Doctoral Thesis

Tumor-associated macrophages secrete Platelet factor 4 to promote Th1-Treg differentiation and suppress antitumor immunity

(腫瘍関連マクロファージは Platelet factor 4 を分泌して Th1-Treg分化を促進し、抗腫瘍免疫を抑制する)

March 2025

Osaka University

Ayumi Kuratani

Abstract

The tumor microenvironment contains various immunosuppressive cells, including regulatory T cells (Tregs) and tumor-associated macrophages (TAMs). It has previously shown that one subset of Tregs, Th1-type Tregs (Th1-Tregs), significantly accumulates in tumors and potently suppresses antitumor immunity. However, the mechanism of Th1-Treg accumulation in tumors remained unknown. Recent studies have revealed a high correlation between TAMs and tumor-infiltrating Tregs, suggesting that TAMs may be involved in the recruitment of Tregs into tumors and in immunosuppressive functions.

In this study, I generated a novel mouse model in which TAMs can be labeled and removed to elucidate the function of TAMs. Depletion of TAMs resulted in a reduced percentage of Th1-Tregs in the tumor and suppressed tumor growth. I then examined whether TAMs are involved in the induction of differentiation of Tregs into Th1-Tregs by a TAM-Treg co-culture system. The results revealed that TAM induces Treg differentiation into Th1-Treg. Furthermore, we investigated the mechanism of TAM induction of Th1-Treg, and found that the chemokine platelet factor 4 (PF4), which is highly expressed in TAMs, is involved in Th1-Treg differentiation.

To elucidate the *in vivo* function of PF4, systemic PF4-deficient and macrophage-specific PF4-deficient mice were generated. The results showed that both systemic PF4-deficient and macrophage-specific PF4-deficient mice had a reduced percentage of Th1-Tregs in tumors and slower tumor growth compared to wild-type mice.

Finally, to investigate whether systemic neutralization of PF4 with PF4-specific antibodies has immunotherapeutic effects against tumors, neutralizing antibodies that inhibit PF4 function were generated, and administered it to tumor-bearing mice. The results showed that the administration of PF4 neutralizing antibody reduced the percentage of Th1-Tregs in the tumor, activated anti-tumor immunity, and suppressed tumor growth. Furthermore, administration of PF4-neutralizing antibody did not induce autoimmunity which occurs by removal of all Tregs.

These findings indicate that PF4 produced by TAMs promotes tumor growth by inducing Treg differentiation into Th1-Tregs and strongly suppressing anti-tumor immunity. PF4 may thus be a novel therapeutic target for safe and effective cancer immunotherapy.

Table of Contents

Abbreviations

APC: allophycocyanin

Arg1: Arginase1

cDC1: Conventional type 1 DC

CSF1R: colony stimulating factor 1 receptor

CyTOF: Cytometry by time of flight

Cx3cr1: CX3C chemokine receptor 1

cy5.5: Cyanine5.5

cy7: Cyanine7

DC: Dendritic cell

DMEM: Dulbecco's Modified Eagle Medium

DT: diphtheria toxin

DTR: diphtheria toxin receptor

FBS: Fetal Bovine Serum

Foxp3: forkhead box P3

HBSS: Hanks' Balanced Salt Solution

IFN-γ: Interferon gamma

IL: Interleukin

iNOS: Inducible nitic oxide synthase

LN: lymph node

NK cell: natural killer cells

PBS: Phosphate Buffered Saline

PE: phycoerythrin

Percp: peridinin chlorophyll protein

Pf4: Platelet factor 4

RFP: Red fluorescent protein

rpm: round per minutes

RPMI: Roswell Park Memorial Institute

RT-PCR: Reverse Transcription Polymerase Chain Reaction

scRNA-seq: single-cell RNA sequencing

SPM: Spleen macrophage

TAM: Tumor associated macrophage

T-bet: T-box 21

Tcov: conventional T cell

Th1-Treg: T helper 1 (Th1)-type Treg

TIM: tumor-infiltrating myeloid

TME: Tumor microenvironment

TNF-α: Tumor necrosis factor alfa

t-SNE: t-Distributed Stochastic Neighbor Embedding

Treg: regulatory T cell

TuDC: tumor-infiltrating DCs

WT: Wild Type

YFP: Yellow fluorescent protein

Introduction

The tumor microenvironment (TME) is a complex environment that consists of tumor cells as well as surrounding non-neoplastic cells and molecules, and plays an important role in tumor growth, progression, and immune evasion. TME includes innate and adaptive immune cells, fibroblasts, vascular endothelial cells, and the extracellular matrix [1-11], which interact to regulate tumor behavior [12, 13].

Among adaptive immune cells in TME, regulatory T cells (Tregs) are known to suppress anti-tumor immunity and promote tumor growth [14-16]. Tregs are a specialized subset of $CD4^+$ T cells that play a crucial role in maintaining immune homeostasis [17, 18], and express CD25 on the cell surface and the Treg-specific transcription factor Forkhead box P3 (Foxp3) in the nucleus [19, 20]. Systemic Treg removal has been reported to cause activation of anti-tumor immunity and induce suppression of tumor growth, while triggering autoimmunity [21].

Tumor-infiltrating Tregs can be further polarized to a T helper 1 (Th1)-type subset that expresses not only Foxp3 but also the Th1 lineage determinant transcription factor T-bet (encoded by the *Tbx21* gene) [8, 22], hence called Th1-type Tregs (Th1-Tregs) [23]. Th1-Tregs abundantly accumulate in tumors compared to other non-tumor tissues [6]. The selective depletion of Th1-Tregs reactivates anti-tumor immunity and inhibits tumor growth [6], demonstrating a pro-tumor role of Th1-Tregs.

Macrophages are innate immune cells found in the TME [3, 5]. Macrophages play an important role in tissue homeostasis and repair as well as defense against pathogen infection [24, 25]. An essential feature of macrophages is phenotypic and functional plasticity [26]. Macrophages reversibly change function and morphology in response to environmental changes, contributing to tissue homeostasis and inflammatory and immune responses. Macrophages classically activated by Th1 cytokines such as lipopolysaccharide (LPS) and interferon γ polarize to type M1. TNF-alpha, IL-1, IL-6, and inducible nitric oxide synthase (iNOS), which have potent bactericidal and tumor-killing activities. On the other hand, macrophages activated by Th2 cytokines such as IL-4 and IL-13 polarize to M2 type and are involved in parasite invasion, suppression of inflammation, and tissue repair [27, 28]. Macrophages within tumors are one of the major components of TME and are referred to as tumor associated macrophages (TAMs), which influence tumor development, growth, anti-tumor immunity, metastasis, and angiogenesis [29, 30]. TAMs are therefore increasingly attracting attention as new targets for tumor therapy [31-34]. In many malignancies, the majority of TAMs exhibit M2-like properties and have been found to act in a tumor-promoting manner, inducing suppression of anti-

tumor immunity and promotion of angiogenesis.15 However, in a complex and diverse cellular environment such as TME, TAMs may not simply be polarized into only two phenotypes, such as M1 and M2 types, but may be a heterogeneous population of macrophage subpopulations with a variety of polarization patterns.

TAMs have also been reported to be involved in the accumulation of immune cells in TME. A high correlation between TAMs and Tregs infiltrating into tumor tissues suggests that TAMs may recruit Tregs to the TME and suppress anti-tumor T cell functions by secreting various cytokines and chemokines [35-37]. Moreover, anti-colony stimulating factor 1 receptor (CSF1R) monoclonal antibody (mAb)-mediated TAM depletion was shown to decrease Tregs in a mouse lung cancer model, suggesting a link between TAMs and Tregs [38]. Here I have investigated how cells, including TAMs, and factors in the TME contribute to abundant tumor infiltration of Th1-Tregs and whether an intervention of such cellular interactions could augment anti-tumor immunity.

RESULTS

1. Generation of a TAM-specific depletion system using VeDTR

In order to test whether TAMs are involved in the high Th1-Treg ratio in the TME, I set out to develop a genetic system to deplete TAMs. TAMs are well known to express arginase I (Arg1) [35, 39, 40], which was shown to be exclusively present in tumors but not in other non-tumor tissues [39]. To confirm that Arg1 gene expression is specific for TAMs, I generated knock-in mice expressing red fluorescent protein (RFP) under the control of the endogenous Arg1 gene (**Fig. 1A)**. RFP expression was compared in various tissue macrophages such as microglia (brain macrophages), alveolar macrophages (lung macrophages), Kupffer cells (liver macrophages) and spleen macrophages (SPMs) in addition to tumor-infiltrating $CD11b^+$ $Ly6G^-$ cells including TAMs (**Fig. 1B**). I found exclusively high RFP expression in the tumor-infiltrating $CD11b^+$ $Ly6G^-$ cells compared to other tissue macrophages (**Fig. 1B**). The tumor-infiltrating $CD11b^+$ $Ly6G^-$ cell populations potentially contained not only TAMs but also monocytes, dendritic cells (DCs), natural killer cells (NK cells) and other immune cell types. Therefore, based upon the gating strategy for tumor-infiltrating myeloid cells (TIMs) (**Fig. 1C)** [41], I further compared RFP expression among these cell types. I detected preferential RFP expression in TAMs but barely in the others among TIMs and NK cells (**Fig. S1D)**, indicating that Arg1 is exclusively expressed in TAMs. Although Arg1 was preferentially expressed in TAMs, Arg1 alone could not be used to specifically mark TAMs due to the macrophage-independent high expression in the liver (**Fig. 1E**).

Therefore, I decided to use the VeDTR mouse system enabling intersectional genetic expression of yellow fluorescent protein (YFP) and diphtheria toxin receptor (DTR) [6]. $Arg1^+$ TAMs had to be specifically characterized by two different genes in the VeDTR system. I selected the Cx3cr1 gene as the second marker, since Cx3cr1 is a well-known macrophage/monocyte marker and the Cre driver mice are widely used [42]. I engineered Cx3cr1-Cre knock in mice by genome editing (**Fig. 2A**), and generated Cx3cr1-Cre/VeDTR(ΔFRT) mice (**Fig. 2B**), where I found that all $Cx3cr1^+$ cells express YFP in most $CD11b^+$ cells in spleens and tumors (**Fig. 2C**). When single-cell RNA-seq (scRNA-seq) analysis was performed using YFP^+ $CD45^+$ cells in tumors or spleens (**Fig. 2D**), TAMs and SPMs were found to be distinctly clustered in the t-SNE plot (**Fig. 2D and 2E**). As previously reported [43], some non-$CD11b^+$ populations such as B cells, T cells, NK cells and DCs were also detected in YFP^+ cells from Cx3cr1-Cre/VeDTR(ΔFRT) mice (**Fig. 2E**). Expectedly, the Arg1 gene was exclusively expressed in a subset of TAMs but barely detected in SPMs or other non-macrophage cells populations (**Fig. 2F**). To use

the Arg1 gene in the VeDTR system (**Fig. 1A**), I generated knock-in mice expressing Flp recombinase under the control of the endogenous Arg1 gene (**Fig. 2G**), and crossed them with Cx3cr1-Cre and VeDTR(LF) mice that require both Cre and Flp recombinases to express YFP and DTR under the control of endogenous Cx3cr1 and Arg1 genes (**Fig. 4A**). The resultant Cx3cr1-Cre/Arg1-Flp/VeDTR(LF) mice were tested for YFP expression in various tissue macrophages (**Fig. 4B**). In Cx3cr1-Cre/Arg1-Flp/VeDTR(LF) mice, YFP was exclusively detected in tumor-infiltrating $CD11b^+$ $Ly6G^-$ cells compared to other tissue macrophages (**Fig. 4B**). Moreover, robust DTR expression was detected in TAMs but barely in SPMs or non-macrophage liver tissues (**Fig. 4C**), suggesting that TAMs are specifically marked in tumor-bearing Cx3cr1-Cre/Arg1-Flp/VeDTR(LF) mice. When localization of $Arg1^+$ TAMs (DTR^+ cells) were assessed by immunohistochemistry, they were preferentially found at hypoxic zones in tumors (**Fig. 3A**), as described previously [44]. Upon DT injection, YFP^+ $CD11b^+$ cells were depleted in tumors (**Fig. 4D**). Furthermore, growth of tumors (MC38 colon adenocarcinoma and B16F10 melanoma) in YFP^+ TAM-depleted Cx3cr1-Cre/Arg1-Flp/VeDTR(LF) mice was significantly inhibited compared to that in the non-depleted control mice (**Fig. 4E** and **4F**), demonstrating that $Arg1^+$ TAM depletion reduces tumor growth.

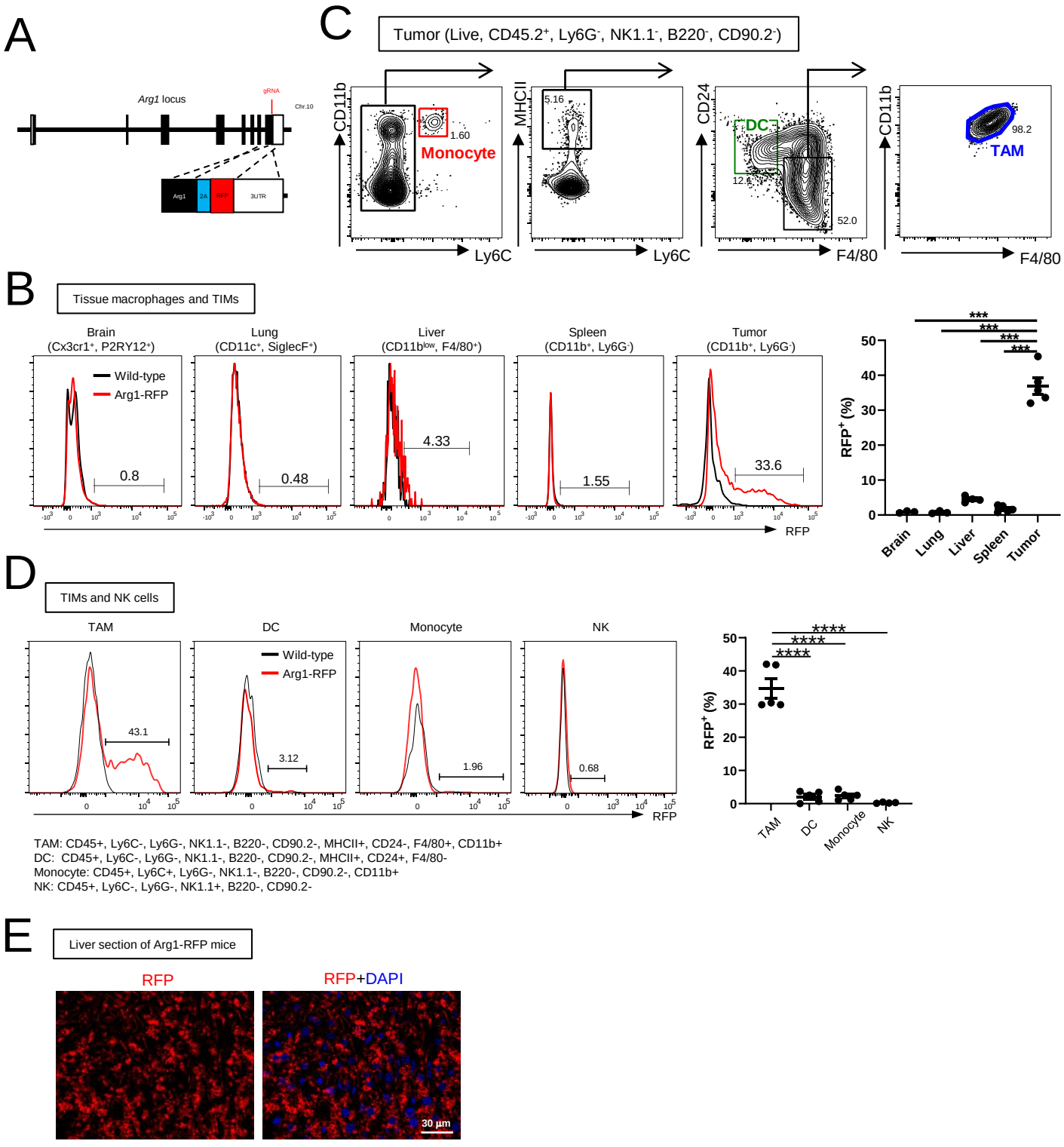

Fig. 1. Generation of Arg1-RFP mice.

(**A**) Targeting strategy for the *Arg1* locus to insert P2A-mCherry.

(**B**) Flow cytometry analysis of tissue macrophages of derived from Arg1-RFP mice (n = 5) that were inoculated s.c. with MC38 cells. Representative histogram overlays and measurements of percentages of RFP^+ cells in indicated tissue macrophage population with indicated surface markers are shown.

(**C**) Flow cytometry gating schematic for sorting and analysis of specified MC38 tumor $CD45.2^-$ $CD90.2^-$ $B220^-$ $Ly6G^-$ $NK1.1^-$ myeloid populations in accordance with Mujal AM, *et al* [41].

(**D**) Flow cytometry analysis of MC38 tumor $CD45.2^-$ $CD90.2^-$ $B220^-$ $Ly6G^-$ $NK1.1^-$ myeloid populations and NK cells derived from Arg1-RFP mice (n = 5) that were inoculated s.c. with MC38 cells. Representative histogram overlays and measurements of percentages of RFP^+ cells in indicated myeloid populations in addition to NK cells with indicated surface markers are shown.

(**E**) Immunohistochemistry analysis of tissue sections derived from Arg1-RFP mice that were inoculated s.c. with MC38 cells. Representative images of indicated tissue sections stained with anti-RFP antibody and DAPI.

Data are mean ± SEM, and pooled from two to three independent experiments. Statistical analysis was performed using one way ANOVA followed Dunnett's multiple comparisons test (B, D). ****, $P < 0.0001$; ns, nonsignificant.

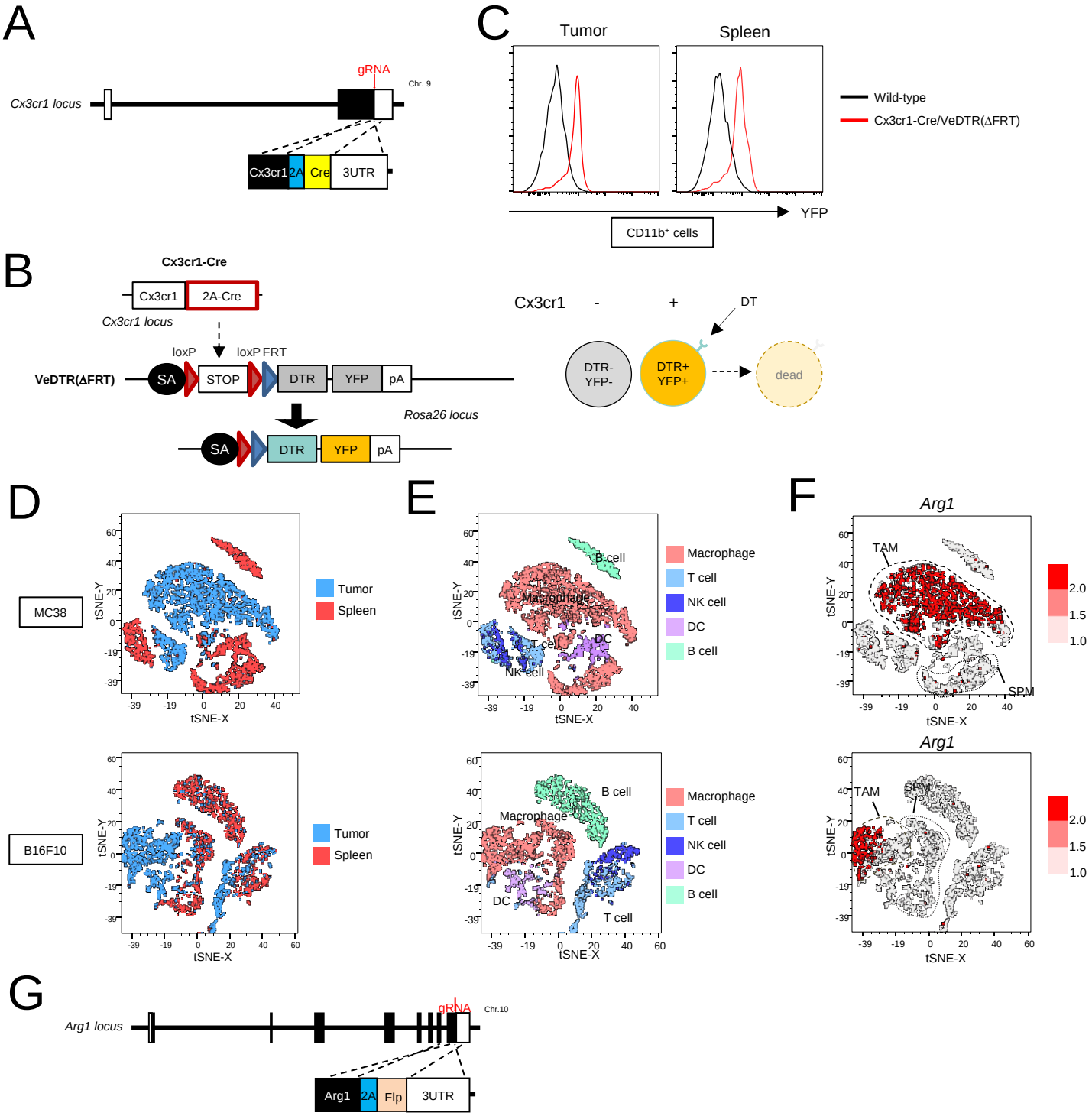

Fig. 2. Generation of Cx3cr1-Cre mice and Arg1-Flp mice.

(**A**) Targeting strategy for the *Cx3cr1* locus to insert the P2A-Cre cassette.

(**B**) Strategy to generate Cx3cr1-Cre/VeDTR(ΔFRT) mice that allow Cx3cr1-dependent expression of YFP and DTR.

(**C**) Flow cytometry analysis of CD45$^+$ CD11b$^+$ Ly6G$^-$ cells from indicated tissues of MC38-bearing Cx3cr1-Cre/VeDTR(ΔFRT) mice. Representative histogram overlays are shown. Data are representative of three independent experiments.

(**D-F**) scRNA-seq analysis of CD45$^+$ YFP$^+$ cells derived from spleens and tumors of Cx3cr1-Cre/VeDTR(ΔFRT) mice (n = 3), into which tumor cells (MC38 cells or B16F10 cells) were subcutaneously (s.c.) transplanted. *t*-distributed stochastic neighbor embedding (t-SNE) plot showing all cells sequenced with each color representing tissues of origin (D), the immune cell types (E), and expression of Arg1 (F).

(**G**) Targeting strategy for the *Arg1* locus to insert the P2A-Flp cassette.

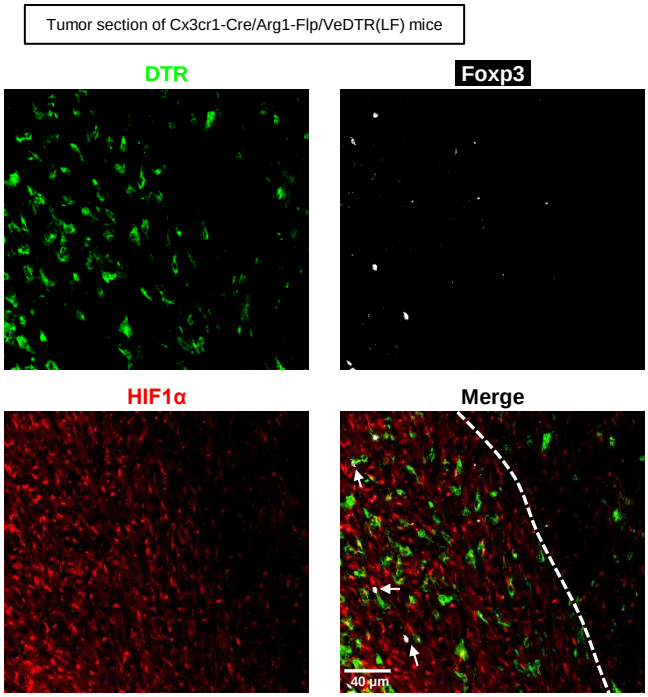

Fig.3. Arg1^{+} TAMs were preferentially found at hypoxic zones in tumors.
Immunohistochemistry analysis of tissue sections derived from Cx3cr1-Cre/Arg1-Flp/VeDTR(LF) mice that were inoculated s.c. with MC38 cells. Representative images of tumor tissue sections stained with anti-DTR (green), anti-HIF1α (red). Data were representative of three independent experiments

2. Arg1$^+$ TAM depletion decreases Th1-Treg ratios in TME

I investigated the impact of Arg1$^+$ TAM depletion on the status of Th1-Treg in the TME. A marked reduction of Foxp3$^+$ T-bet$^+$ CD4$^+$ T cell ratios was observed in MC38 and B16F10 tumors after Arg1$^+$ TAM depletion by flow cytometry (**Fig. 5A** and **5B**). Next, I analyzed the effect of Arg1$^+$ TAM depletion on the CD11b$^-$ CD45$^+$ lymphocyte population (non-macrophage population) using mass cytometry (CyTOF) (**Fig. 6A**, **6B**, **6C** and **Fig. 7**). The ratios of Foxp3$^+$ T-bet$^+$ cells were reduced, whilst T-bet$^+$ LAG-3$^-$ CD8$^+$ T cells were increased (**Fig. 6A**, **6B**, **6C** and **Fig. 7**). In contrast, the ratios of other populations remained statistically unchanged (**Fig. 7**), suggesting the negative and positive impact of Arg1$^+$ TAM depletion on the ratios of Th1-Tregs and T-bet$^+$ LAG-3$^-$ CD8$^+$ T cells in tumor-infiltrating CD11b$^-$ cells, respectively. Given the role of LAG-3 in CD8$^+$ T cell exhaustion [45], Arg1$^+$ TAM depletion might ameliorate immune suppression in TME. The status of CD11b$^+$ CD45$^+$ cells in the TME after Arg1$^+$ TAM depletion was assessed by CyTOF (**Fig. 8A**, **8B**, and **8C**). I found that Arg1$^+$ TAM depletion significantly increased the ratios of CD80^{high} or iNOS$^+$ CD11b$^+$ cells in addition to Ly6G$^+$ CD11b$^+$ cells. I confirmed the increase of CD80 and iNOS, and reduction of CD206 after Arg1$^+$ TAM depletion by flow cytometry and immunohistochemistry (**Fig. 9A and 9B**). Given decreased ratios of pro-tumor Th1-Tregs and immune-suppressive macrophage marker CD206, and the increased ratios of anti-tumor macrophage markers (CD80 and iNOS), I asked whether Arg1$^+$ TAM depletion may lead to anti-tumor immunity. I therefore assessed the production of anti-tumor cytokines such as TNF-α and IFN-γ from CD4$^+$ T cells by flow cytometry (**Fig. 10**). Although the numbers of CD4$^+$ T cells and CD8+ T cells in tumors remained unchanged after Arg1$^+$ TAM depletion (**Fig. 11A**), it was noteworthy that the ratios of TNF-α$^+$/IFN-γ$^+$ CD4$^+$ T cells and CD8$^+$ T cells in tumors of Arg1$^+$ TAM-depleted Cx3cr1-Cre/Arg1-Flp/VeDTR(LF) mice were much higher than those in the non-depleted control mice (**Fig. 10**), suggesting qualitative but not quantitative changes in intra-tumoral CD4$^+$ T cells and CD8$^+$ T cells due to Arg1$^+$ TAM depletion. The ratios of Tregs (Foxp3$^+$ CD4$^+$ cells) and conventional CD4$^+$ T cells (Tconvs: Foxp3$^-$ CD4$^+$ cells) in draining lymph nodes (LNs) were unchanged after Arg1+ TAM depletion (**Fig. 11B**), suggesting that Arg1$^+$ TAMs are not involved in regulating the numbers of Tregs and Tconvs in draining LNs. Taken together, these data suggest that Arg1$^+$ TAM depletion reduces ratios of Th1-Tregs and immune-suppressive TAMs and increases those of immune-stimulatory CD11b$^+$ cells and T-bet$^+$ LAG-3$^-$ CD8$^+$ T cells in tumors, leading to anti-tumor immunity.

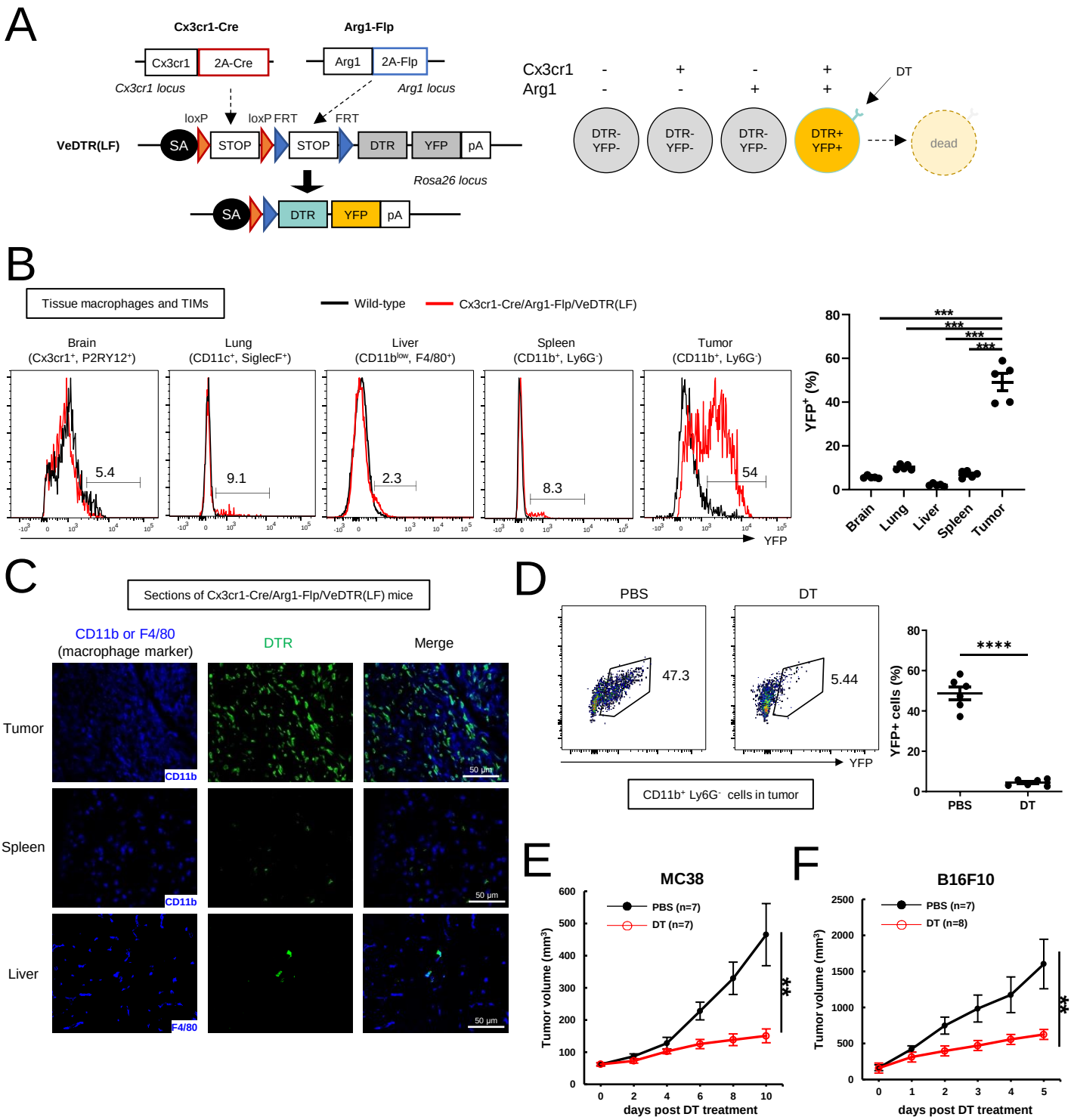

Fig. 4. Generation of Arg1+ TAM-targeted mice by VeDTR.

(**A**) Strategy to generate Cx3cr1-Cre/Arg1-Flp/VeDTR(LF) mice that allow Cx3cr1- and Arg1-dependent intersectional expression of YFP and DTR.

(**B**) Flow cytometry analysis of tissue macrophages derived from Cx3cr1-Cre/Arg1-Flp/VeDTR(LF) mice (n = 5) that were inoculated s.c. with MC38 tumor cells. Representative histogram overlays and measurements of percentages of YFP^+ cells in tissue macrophage populations with the indicated surface markers are shown.

(**C**) Immunohistochemistry analysis of tissue sections derived from Cx3cr1-Cre/Arg1-Flp/VeDTR(LF) mice that were inoculated s.c. with MC38 cells. Representative images of indicated tissue sections stained with anti-CD11b or F4/80 and anti-DTR antibodies.

(**D**) Flow cytometry analysis of intra-tumoral $CD45^+$ $CD11b^+$ $Ly6G^-$ cells (TAMs) derived from PBS-or DT-treated Cx3cr1-Cre/Arg1-Flp/VeDTR(LF) mice (n = 6 per group) that were inoculated s.c. with MC38 cells. Representative FACS plots and the percentages of YFP^+ cells in TAMs are shown.

(**E, F**) Growth of s.c. implanted MC38 (E) or B16F10 (F) tumors in PBS-injected mice and DT-injected Cx3cr1-Cre/Arg1-Flp/VeDTR(LF) mice (indicated numbers of mice per group).
Data indicate mean ± SEM, and are pooled from two to three independent experiments. Statistical analysis was performed using one-way ANOVA followed by Dunnett's multiple comparisons test (B) and two-tailed Student's t-tests (D, E, F). **, $P < 0.01$; ***, $P < 0.001$; ****, $P < 0.0001$; ns, nonsignificant.

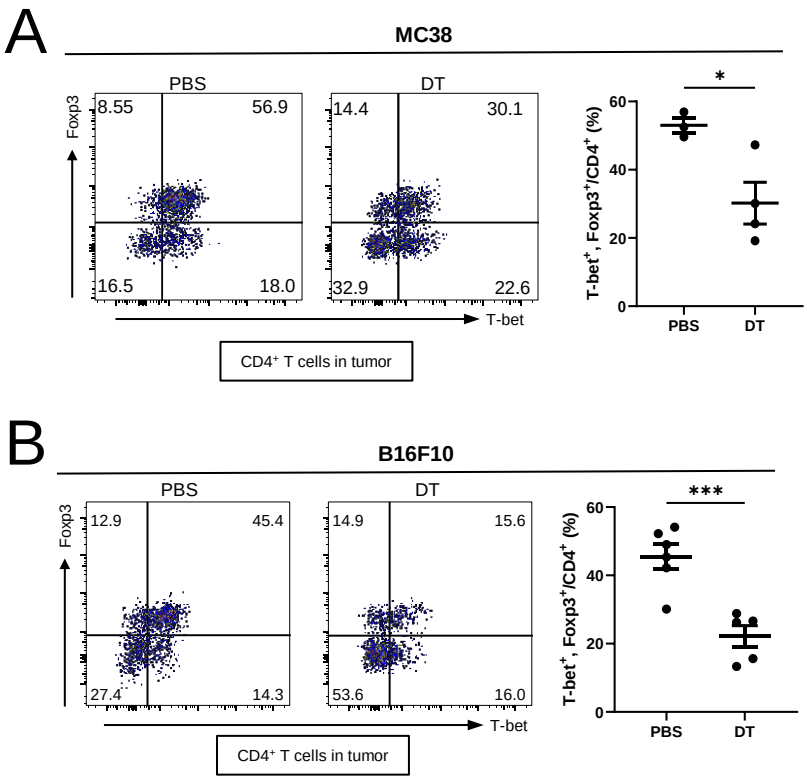

Fig. 5. Depletion of Arg1⁺ TAMs reduces Th1-Treg ratios in tumors.
(**A,B**) Flow cytometry analysis of tumor-infiltrating CD4⁺ T cells derived from Cx3cr1-Cre/Arg1-Flp/VeDTR(LF) mice that were s.c. implanted with MC38 (**A**) or B16F10 (**B**) tumor cells. Representative FACS plots and the percentages of Foxp3 and T-bet double-positive cells in tumor-infiltrating CD4⁺ T cells. n = 3 per group.

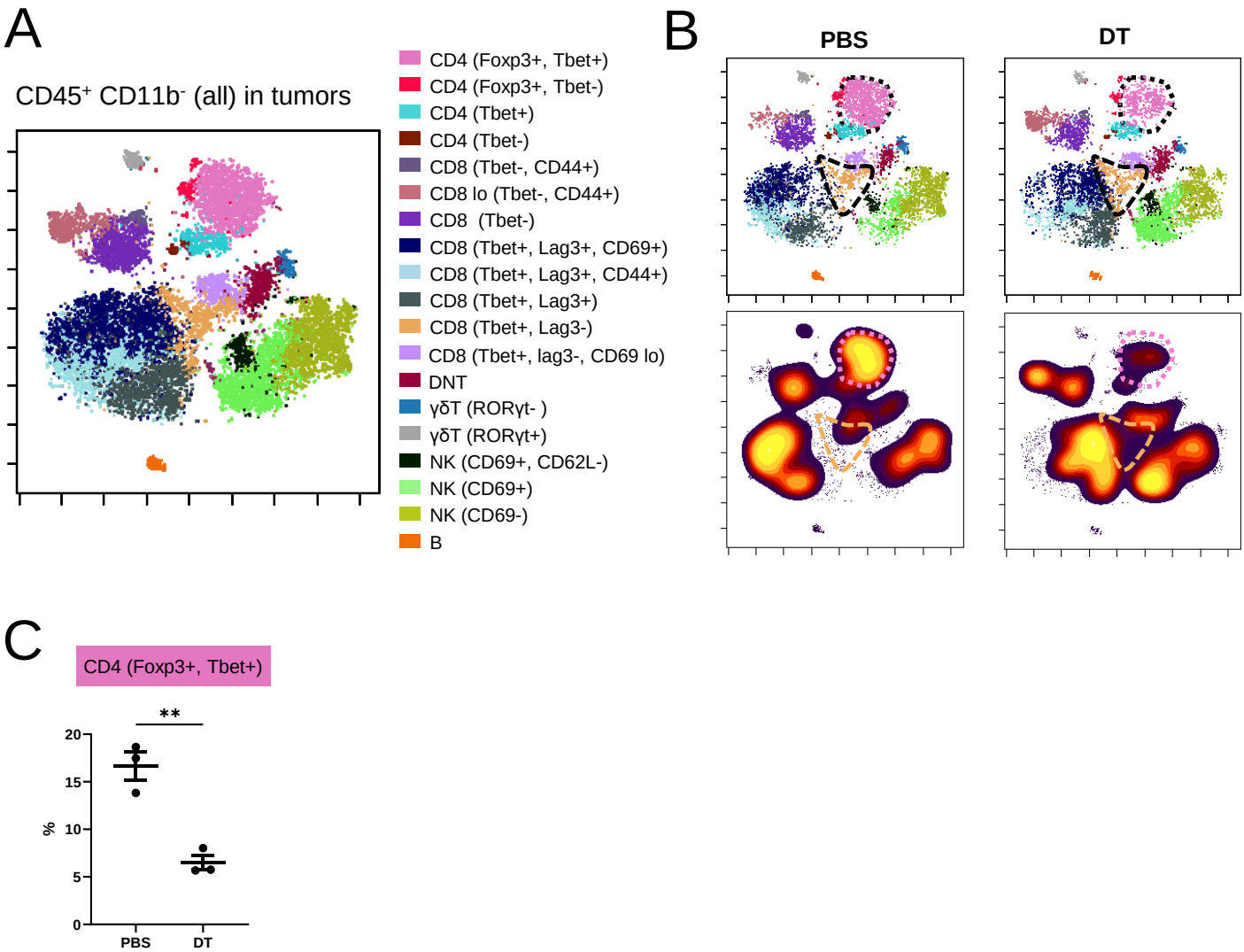

Fig.6. CyTOF analysis showed that depletion of Arg1^{+}TAM reduces Th1-Treg ratio in tumors.
(**A-C**), CyTOF analysis of CD45^{+} CD11b^{-} cells derived from Cx3cr1-Cre/Arg1-Flp/VeDTR(LF) mice were s.c. implanted with MC38 cells at 20 days post tumor inoculation. Data show pooled replicates (n = 3 biologically independent mice of DT condition and n = 3 biologically independent mice of PBS condition). t-SNE plot of 19,356 CD45^{+} CD11b^{-} cells (A), tSNE plot and contour plot (B), and measurements of percentages of CD4^{+} Foxp3^{+} T-bet^{+} cells from mice with PBS condition and DT condition (C). Dashed lines indicate cell population with statistical difference. Related to Fig. 7.
Data indicate mean ± SEM, and are pooled from two to three independent experiments. Statistical analysis was performed using two-tailed Student's t-tests (C). **, $P < 0.01$

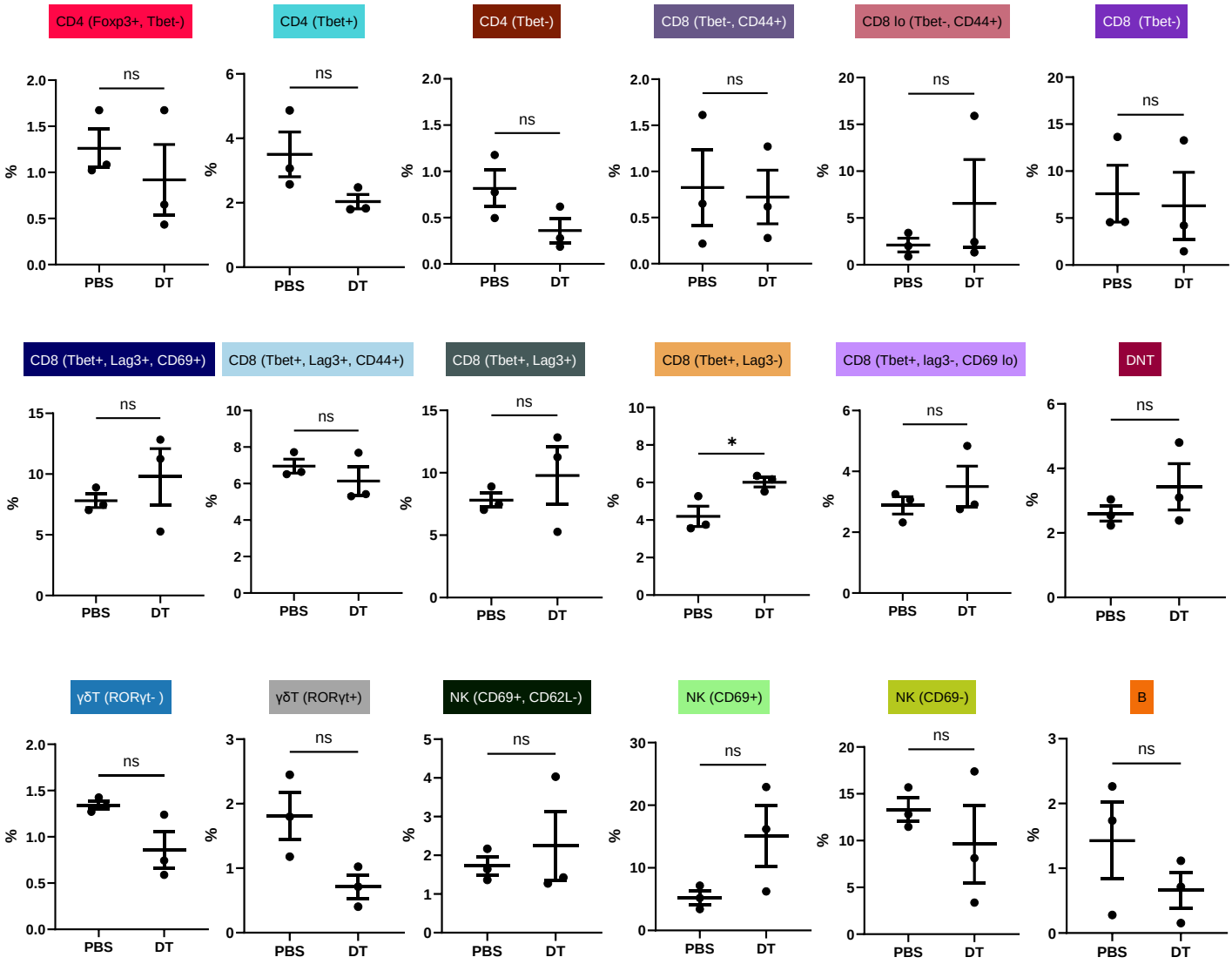

Fig.7. Analysis of tumor infiltrating Lymphocyte during Arg1^{+} TAM Removal by CyTOF.
CyTOF analysis of CD45^{+} CD11b^{-} cells derived from Cx3cr1-Cre/Arg1-Flp/VeDTR(LF) mice were s.c. implanted with MC38 cells at day 20 post tumor inoculation. Data show pooled replicates (n = 3 biologically independent mice of DT condition and n = 3 biologically independent mice of PBS condition). Measurements of percentages of indicated cell population from mice with PBS condition and DT condition.
Data are mean ± SEM, and pooled from two to three independent experiments. Statistical analysis was performed using two-tailed Student's t-tests.

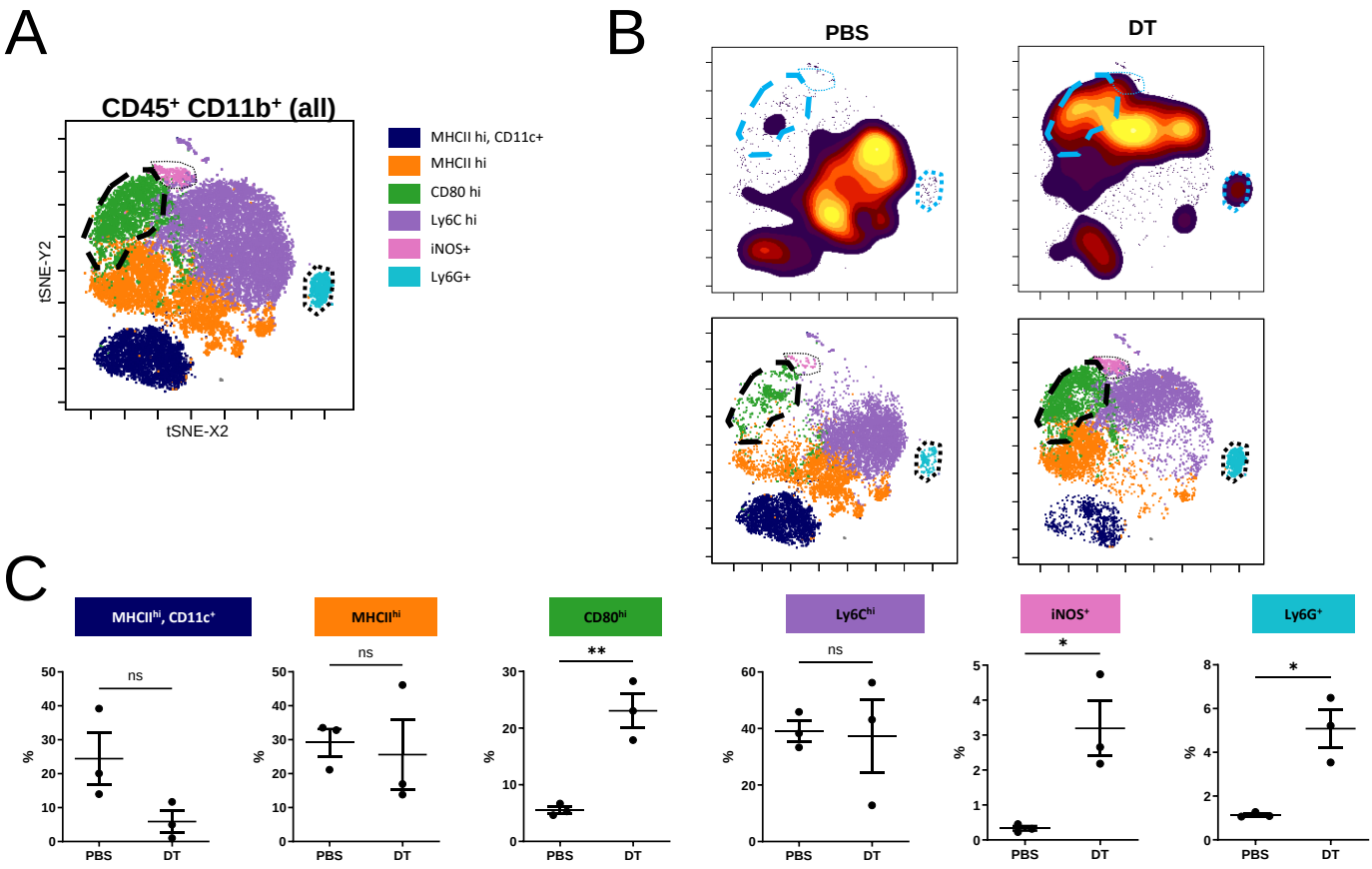

Fig.8. Analysis of tumor infiltrating Myeloids during Arg1$^+$ TAM Removal by CyTOF.
(**A-C**) CyTOF analysis of CD11b$^+$ CD45$^+$ cells derived from Cx3cr1-Cre/Arg1-Flp/VeDTR(LF) mice were s.c. implanted with MC38 cells at day 20 post tumor inoculation. Data show pooled replicates (n = 3 biologically independent mice of DT condition and n = 3 biologically independent mice of PBS condition). t-SNE plot of 26,448 CD45$^+$ CD11b$^+$ cells (A), tSNE plot and contour plot (B), and measurements of percentages of indicated cells from mice with PBS condition and DT condition (C). Dashed lines indicate cell population with statistical difference.
Data are mean ± SEM, and pooled from two independent experiments. Statistical analysis was performed using two-tailed Student's t-tests (C). *, $P < 0.05$; ns, nonsignificant.

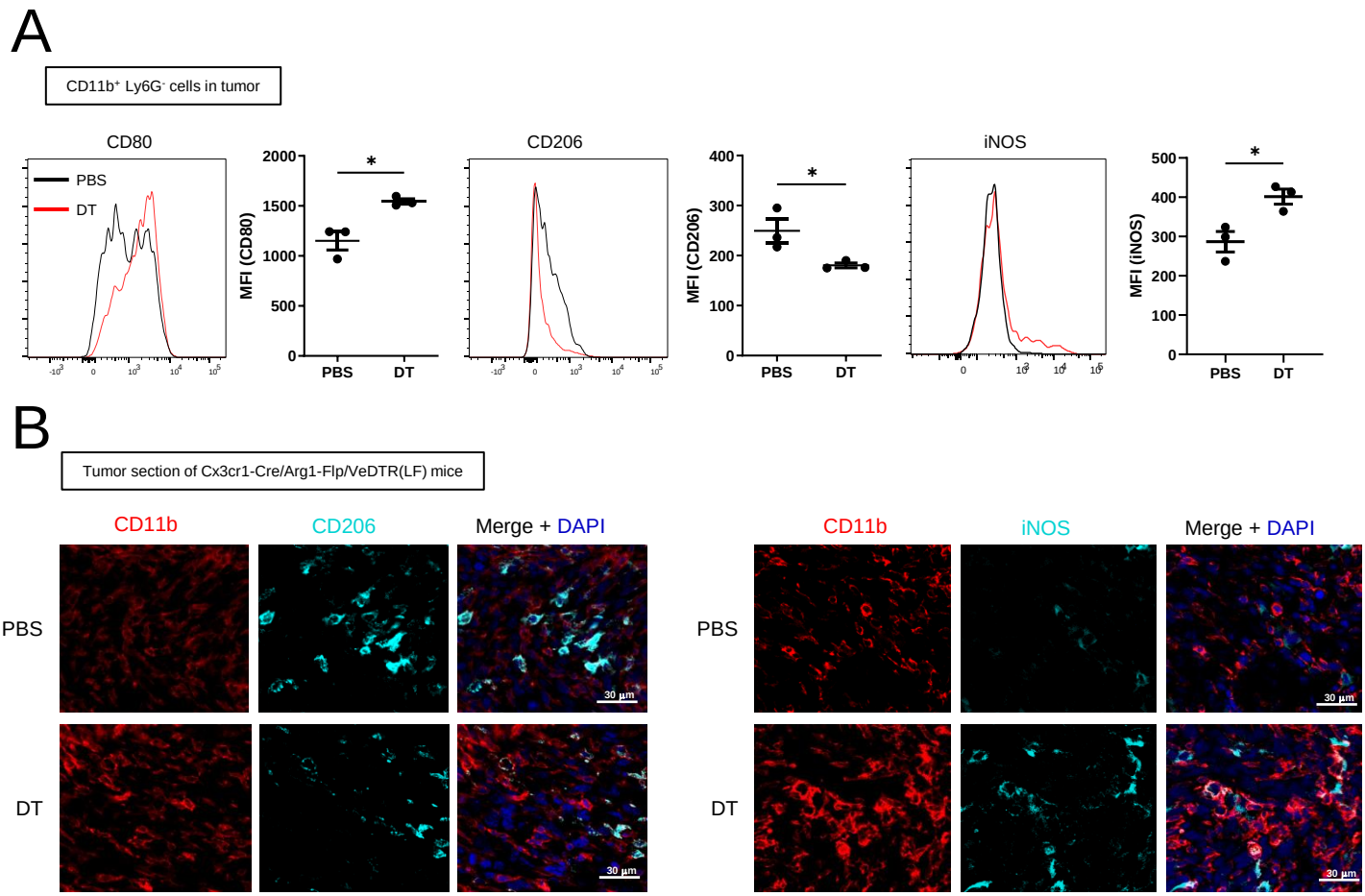

Fig.9. Increase in CD80 and iNOS and decrease in CD206 after Arg1+ TAM depletion by flow cytometry and immunohistochemistry.

(**A**) Flow cytometry analysis of indicated surface markers on intra-tumoral $CD11b^+$ $CD45^+$ cells of derived from PBS-or DT-treated Cx3cr1-Cre/Arg1-Flp/VeDTR(LF) mice (n = 3 per group) that were inoculated s.c. with MC38 cells. Representative histogram overlays and measurements of mean fluorescence intensity (MFI).

(**B**) Immunohistochemistry analysis of tissue sections derived from PBS- or DT-treated Cx3cr1-Cre/Arg1-Flp/VeDTR(LF) mice that were inoculated s.c. with MC38 cells. Representative images of indicated tissue sections stained with anti-CD11b (red), CD206 or iNOS (blue) antibodies.

Data are mean ± SEM, and pooled from two independent experiments. Statistical analysis was performed using two-tailed Student's t-tests (A). *, $P < 0.05$; ns, nonsignificant.

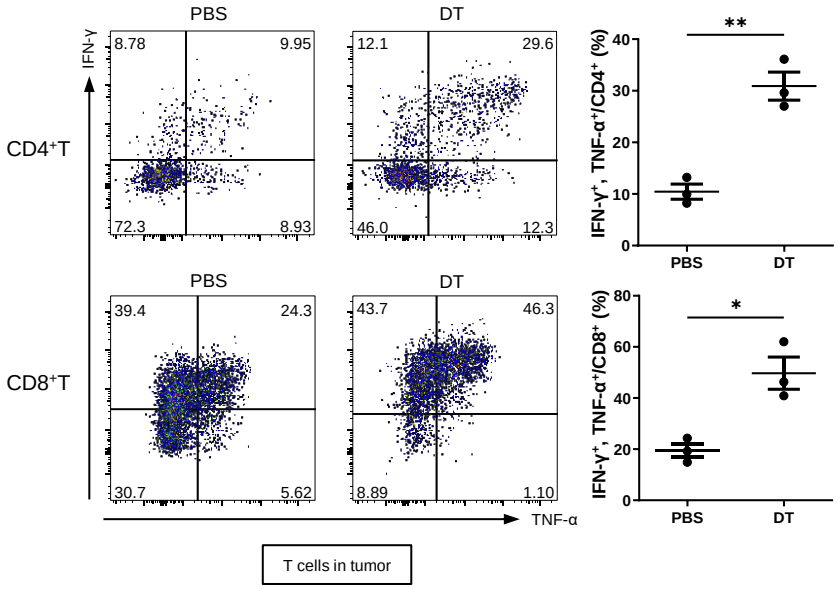

Fig.10. Removal of Arg1TAM increased the percentage of anti-tumor T cells in the tumor.
Flow cytometry analysis of tumor-infiltrating T cells of derived from Cx3cr1-Cre/Arg1-Flp/VeDTR(LF) mice that were s.c. implanted with MC38 cells. Representative FACS plots and the percentages of IFN-γ and TNF-α double-positive cells in intra-tumoral $CD4^+$ (top) and $CD8^+$ (bottom) T cells. n = 3 per group.
Data indicate mean ± SEM, and are pooled from two to three independent experiments. Statistical analysis was performed using two-tailed Student's t-tests (A, D, E). *, $P < 0.05$; **, $P < 0.01$

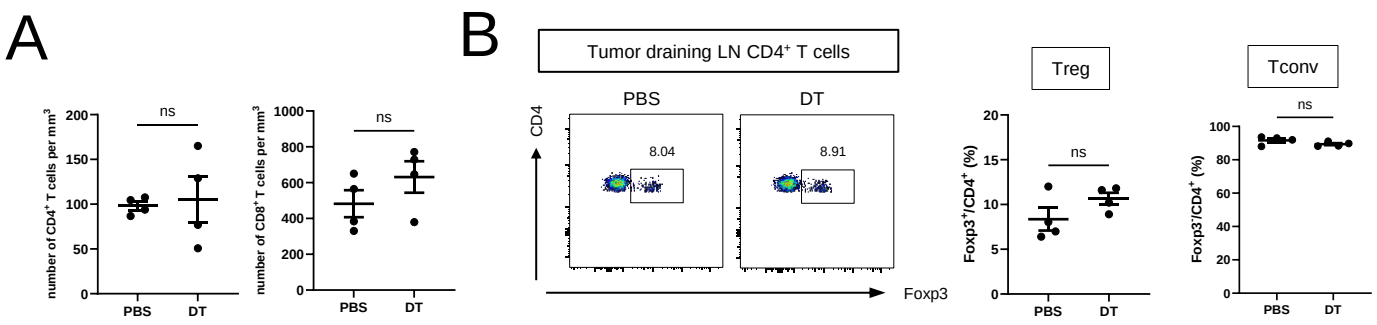

Fig.11. The number of CD4$^+$ T cells and CD8$^+$ T cells in the tumor remained unchanged after depletion of Arg1$^+$ TAM.

(**A**) Numbers of CD4$^+$ T cells and CD8$^+$ T cells per 1 mm^3 of tumor derived from Cx3cr1-Cre/Arg1-Flp/VeDTR(LF) mice that were s.c. implanted with MC38 cells. n = 4 per group.

(**B**) Flow cytometry analysis of CD4$^+$ T cells in inguinal LNs (ILNs) derived from Cx3cr1-Cre/Arg1-Flp/VeDTR(LF) mice that were s.c. implanted with MC38 cells. Representative FACS plots and the percentages of Foxp3-positive cells in ILN CD4$^+$ T cells. n = 4 per group.

Data are mean ± SEM, and pooled from two to three independent experiments. Statistical analysis was performed using two-tailed Student's t-tests (A, B). ns, nonsignificant.

3. TAMs secrete PF4 that polarizes Tregs into Th1-Treg cells

Th1-Tregs accumulate in tumors compared to other non-tumor tissues [6]. $Arg1^+$ macrophages were also present in significant numbers in tumors compared to non-tumor tissues (**Fig. 4B**). $Arg1^+$ TAM depletion led to reduction of Th1-Tregs in tumors (**Fig. 6**). Furthermore, when the localization of $Arg1^+$ TAMs and Tregs in MC38-bearing Cx3cr1-Cre/Arg1-Flp/VeDTR(LF) mice was examined by immunohistochemistry, I found that most of $Foxp3^+$ $CD4^+$ cells associated with DTR^+ cells in the tumors (**Fig. 12A**). I observed the distance between $Foxp3^+$ $CD4^+$ cells and DTR^+ cells was significantly closer in tumors as opposed to spleens (**Fig. 12B**), suggesting a more intimate interaction between Tregs and $Arg1^+$ macrophages within the TME compared to the spleen. High Th1-Treg accumulation in the TME requires that Tregs be polarized into Th1-Tregs, and I hypothesized that $Arg1^+$ TAMs play a role for Treg polarization. To test this possibility, I isolated $Arg1^+$ TAMs (**Fig. 13**) [7], and tested whether Tregs become Th1-Tregs when co-cultured with $Arg1^+$ TAMs (**Fig. 14**). Non-Th1-Tregs (YFP^- $CD4^+$ $CD25^+$ T cells in spleens of tumor-bearing Foxp3-Cre/Tbx21-Flp/VeDTR(LF) mice, hereafter called YFP^- Tregs) were co-cultured with $Arg1^+$ TAMs (RFP^+ TAMs), Arg1- TAMs (RFP^- TAMs) or SPMs, and tested for YFP expression of Tregs to monitor the Th1-Treg polarization (**Fig. 14A**). It was notable that the co-culture of YFP^- Tregs with RFP^+ TAMs resulted in YFP expression in Tregs, whereas that with RFP^- TAM and SPMs did not (**Fig. 14A**), suggesting that $Arg1^+$ TAMs potentiate Th1-Treg polarization. I further analyzed the molecular mechanism by which $Arg1^+$ TAMs polarize Tregs to Th1-Tregs. Initially, I tested whether the *in vitro* Th1-Treg polarization by $Arg1^+$ TAMs requires direct contact between $Arg1^+$ TAMs and non-Th1-Tregs (**Fig. 14B**). When these macrophages and YFP^- Tregs were physically separated by filters, YFP^- Tregs expressed YFP after the co-culture with RFP^+ TAMs but not with RFP^- TAMs and SPMs (**Fig. 14B**), suggesting the presence of humoral factor(s) derived from $Arg1^+$ TAMs in Th1-Treg generation. Moreover, even though $Arg1^+$ TAMs were derived from either MC38 colorectal tumor- or B16F10 melanoma-bearing mice, the YFP expression in non-Th1-Tregs was detected (**Fig. 14B**), suggesting that the Th1-Treg polarization by TAMs may be dependent on the factor(s) common to $Arg1^+$ TAMs in both tumor models but independent on tumor antigens. To explore common humoral factor(s), I compared the gene expression profiles between $Arg1^+$ TAMs and $Arg1^-$ TAMs from B16F10 and MC38 tumor-bearing mice using scRNA-seq and bulk RNA-seq (**Fig. 15A** and 1**5B**). I identified 16 and 85 genes that showed higher expression levels in $Arg1^+$ TAMs than in $Arg1^-$ TAMs by bulk RNA-seq and scRNA-seq, respectively. Among them, 5 genes (*Arg1, Mmp12, Egln3, Spp1 and Pf4*) were shared by both RNA-seq analysis (**Fig. 15C**), and I compared gene expression in

TAMs and SPMs using scRNA-seq (**Fig. 15D**). Expression of *Arg1, Egln3, Spp1* and *Pf4* mRNA was exclusively detected in TAMs but not in SPMs. In contrast, *Mmp12* mRNA was detected in a subset of SPMs from B16F10-bearing mice (**Fig. 15D**), precluding Mmp12 from the candidates. Among the rest, since proteins encoded by *Spp1* and *Pf4* are shown to be secreted [46, 47], the gene products such as secreted phosphoprotein 1 (SPP1, also known as Osteopontin) and Platelet factor 4 (PF4, also known as CXCL4) are humoral factors. In addition, I regarded Arg1 as a humoral factor since it depletes the extracellular arginine pool [48]. In contrast, *Egln3* encodes a prolyl hydroxylase that acts only intracellularly [49, 50]. I therefore precluded *Egln3*, and further investigated the involvement of SPP1, PF4 and Arg1 in Th1-Treg polarization (**Fig. 16A** and **16B**). When non-Th1-Tregs were stimulated with recombinant SPP1, or PF4 protein without $Arg1^+$ TAMs, it was surprising that stimulation with the recombinant PF4 protein caused YFP expression in non-Th1-Tregs, whereas recombinant SPP1 did not (**Fig. 16A**). When I assessed the role of Arg1 in Th1-Treg polarization using the Arg1 inhibitor, I found that treatment with nor-NOHA (an Arg1 inhibitor) in the co-culture of $Arg1^+$ TAMs and non-Th1-Tregs did not affect Th1-Treg conversion (**Fig. 16B**). These results suggest that PF4 is the humoral factor that may be uniquely involved in $Arg1^+$ TAM-induced Th1-Treg polarization among the candidate gene products. When I compared the expression of *Pf4* mRNA in macrophages from various tissues, $Arg1^+$ TAMs exhibited the highest *Pf4* mRNA levels (**Fig. 16C**), further suggesting a specific role of PF4 in $Arg1^+$ TAMs. Next, I assessed whether the PF4-induced Th1-Tregs functionally inhibit the proliferation of conventional $CD4^+$ T cells (**Fig. 16D**). I found stronger suppression of effector $CD4^+$ T cell proliferation by recombinant PF4 protein-stimulated Th1-Tregs than unstimulated non-Th1-Tregs (**Fig. 16D**), indicating that the PF4-induced Th1-Tregs possess a suppressive function. I further analyzed the expression of CD25, GITR, and CTLA-4, molecules that play an important role in regulating Treg function [51, 52]. The surface expression of GITR was not significantly different, whereas CD25 and CTLA-4 expression were increased in recombinant PF4 protein-stimulated Tregs compared to unstimulated Tregs (**Fig. 16E**), suggesting that PF4 enhances suppressive ability. Subsequently, I analyzed the molecular mechanism of how PF4 stimulates the polarization of non-Th1-Tregs into Th1-Tregs. CXCR3 is a receptor for PF4 in humans [53]. I found that the CXCR3 inhibitor (AMG487) profoundly inhibited recombinant PF4 protein-induced conversion of non-Th1-Tregs into Th1-Tregs (**Fig. 16F**), suggesting that PF4 stimulates the Th1-Treg polarization via CXCR3. In addition to PF4, CXCL9, CXCL10 and CXCL11 are also CXCR3 ligands [54]. Among them, CXCL9 is well known as an anti-tumor immune marker [55], so I tested if CXCL9 can induce Th1-Treg

polarization. CXCL9 as well as PF4 was found to stimulate the polarization of non-Th1-Tregs into Th1-Tregs (**Fig. 17A**). I next investigated the source of these chemokines in the tumor models. Conventional type 1 DC (cDC1) is the major source of CXCL9 in the TME because mice devoid of Batf3, the master transcription factor to generate cDC1s [56], are completely devoid of CXCL9 production [7]. I compared the ratios of cDC1s and TAMs. I isolated tumor-infiltrating DCs (TuDCs) and cDC1 based upon the gating strategy shown in Fig. 13 [7]. The ratios of RFP^+ TAMs in $CD45^+$ immune cell populations were much higher than those of cDC1s ($Xcr1^+$ DCs) (**Fig. 17B**), suggesting that there are far more PF4-producing $Arg1^+$ TAMs than CXCL9-producing cDC1s in the TME. I next assessed whether TuDCs also express PF4 and induce Th1-Treg polarization. *Pf4* mRNA levels in TuDCs were lower than in RFP^+ TAMs (**Fig. 17C**) and co-culture of TuDCs with non-Th1-Tregs did not induce Th1-Treg polarization (**Fig. 17D**). Collectively, these data suggest that $Arg1^+$ TAMs, but not TuDCs, produce PF4 to polarize Tregs into Th1-Tregs in a CXCR3-dependent manner.

Next, I explored the mechanisms underlying the expression of CXCR3 on Tregs prior to PF4 stimulation. Given that IFN-γ has been shown to drive the differentiation of Tregs into Th1-Tregs in the tumor-draining LNs [57], I investigated whether IFN-γ is involved in the expression of CXCR3 on Tregs and in the PF4-induced Th1-Treg polarization. I found that IFN-γ stimulated the expression of surface CXCR3 on non-Th1-Tregs in a dose-dependent manner (**Fig. 18A**). Although a low concentration of IFN-γ stimulation was insufficient on its own for Th1-Treg polarization, IFN-γ-dependent Th1-Treg polarization was observed when co-stimulated with PF4 (**Fig. 18B**). Moreover, the basal levels of CXCR3 on non-Th1-Tregs from $Ifngr1^{-/-}$ mice were significantly lower than those from wild-type mice (**Fig. 18C**). I next sorted non-Th1-Tregs from both wild-type and $Ifngr1^{-/-}$ Foxp3-Cre/Tbx21-Flp/VeDTR(LF) mice and tested them for PF4-induced Th1-Treg polarization (**Fig. 18D**). PF4-induced Th1-Treg polarization of non-Th1-Tregs from $Ifngr1^{-/-}$ mice was profoundly impaired compared to that from wild-type mice (**Fig. 18D**). In terms of signal transduction and gene regulation, PF4 stimulation on non-Th1-Tregs led to Stat1 phosphorylation and expression of mRNAs encoding IFN-γ-inducible proteins such as Gbp1, Gbp5, Irgm1, Stat1 and Socs1 (**Fig. 18E** and **18F**). Prior to PF4 stimulation, most of these mRNA levels in wild-type cells were higher than those from $Ifngr1^{-/-}$ mice, and PF4-induced upregulation of the IFN-γ-inducible genes was not observed in $Ifngr1^{-/-}$ cells (**Fig. 18E** and **18F**). These data suggest that the initial fate decision may be determined by IFN-γ signaling. To directly assess the role of IFN-γ stimulation in Tregs, I utilized Foxp3-Cre/$Ifngr1^{fl/fl}$ mice and inoculated them with MC38 tumors. The ratios of Th1-Tregs in the tumors of Foxp3-Cre/Ifngr1fl/fl mice were

significantly lower than those in control mice, while the ratios of Th1-Tregs in spleens were similar between the two groups (**Fig. 18G**). Furthermore, tumor growth in Foxp3-Cre/Ifngr1$^{fl/fl}$ mice was reduced compared to that in control mice (**Fig. 18H**). Taken together, these results suggest that IFN-γ signaling-induced CXCR3 expression is a prerequisite for Th1-Treg polarization which is further reinforced by PF4, thereby promoting tumor growth.

I further explored the mechanisms by which Arg1^{+} TAMs express PF4 (**Fig. 19**). It was notable that co-culture of SPMs with B16F10 melanoma cells could increase Pf4 mRNA expression (**Fig. 19A**). Due to the Warburg effect, tumor tissues are known to have high concentrations of lactic acid [58]. Indeed, both B16F10 melanoma and MC38 colorectal tumor tissues exhibited markedly high lactic acid concentrations compared to spleens from the same tumor-bearing mice (**Fig. 19B**). Since lactic acid stimulates *Arg1* expression in macrophages [40], I assessed whether it also induces *Pf4* expression using quantitative RT-PCR. Lactic acid stimulation alone potentiated *Pf4* mRNA expression in SPMs (**Fig. 19C**). In contrast, low pH conditions alone did not induce *Pf4* mRNA expression (**Fig. 19D**), suggesting that lactic acid-induced Pf4 expression in macrophages is independent of the acid-induced low pH. Th2 cytokines such as IL-4 and IL-13 are involved in immune-suppressive macrophage polarization in the TME [59]. However, I did not find an increase the expression level of *Pf4* mRNA in SPMs stimulated with IL-4/IL-13 (**Fig. 19E**). In contrast, the IL-4/IL-13, lactic acid and low pH conditions strongly stimulated *Arg1* mRNA expression in SPMs (**Fig. 19C**, **19D** and **19E**) [25, 37, 40], indicating a differential determinant for *Pf4* and *Arg1* mRNA expression in macrophages. Taken together, PF4 induction in TAMs might rely on a tumor-specific condition such as the high lactic acid concentration.

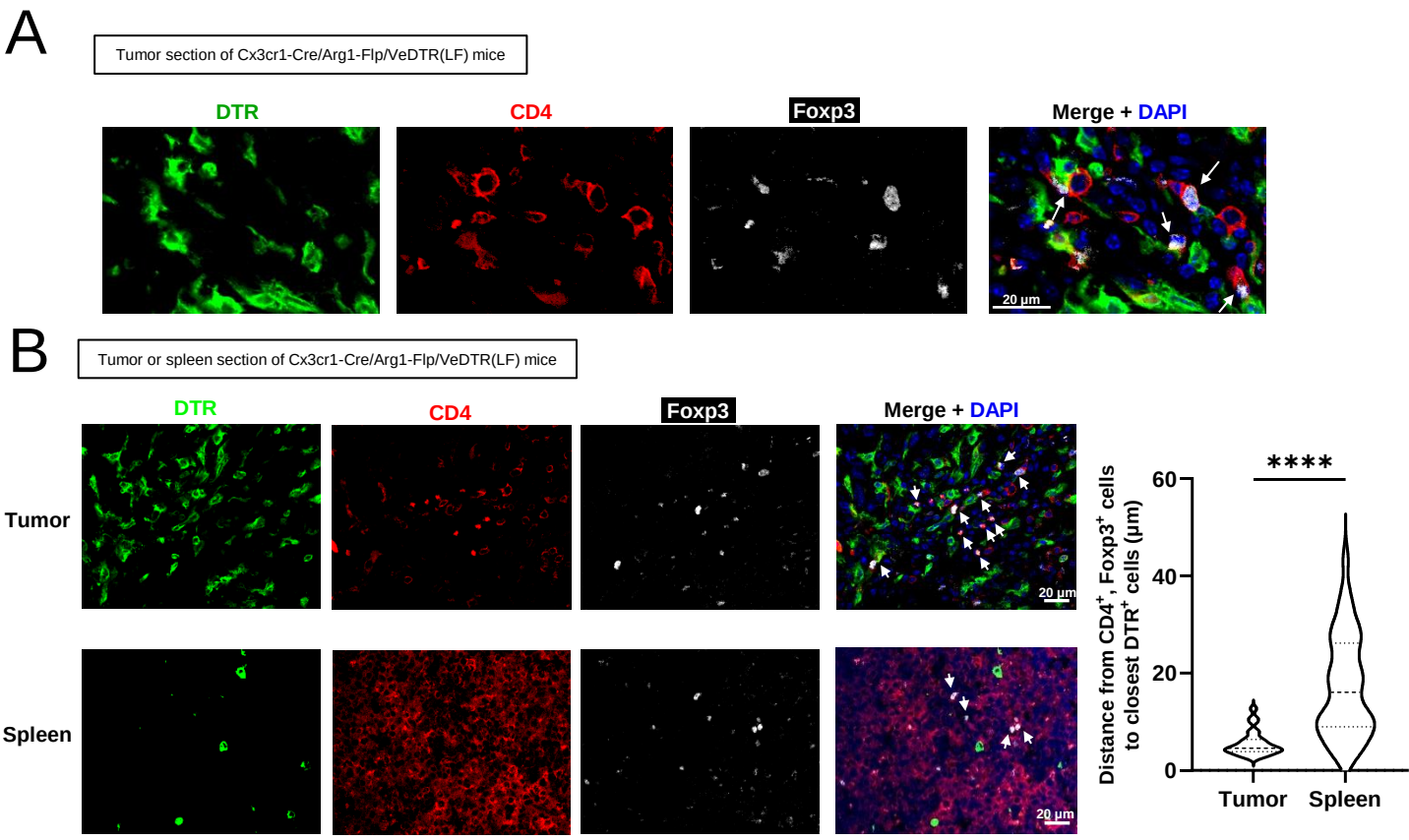

Fig.12. Arg1$^+$TAMs and Tregs were in close contact within the tumor.
(**A**) Immunohistochemistry analysis of tissue sections derived from Cx3cr1-Cre/Arg1-Flp/VeDTR mice that were inoculated s.c. with MC38 cells. Representative images of tumor tissue sections stained with DAPI, anti-DTR (green), anti-CD4 (red), and anti-Foxp3 (white) antibodies. Arrows indicate cell-cell interaction between DTR$^+$ cells (Arg1$^+$ TAMs) and CD4$^+$ Foxp3$^+$ cells (Tregs).
(**B**) Immunohistochemistry analysis of indicated tissue sections derived from Cx3cr1-Cre/Arg1-Flp/VeDTR mice (n =3) that were inoculated s.c. with MC38 cells. Representative images of tumor tissue sections stained with DAPI, anti-DTR (green), anti-CD4 (red), and anti-Foxp3 (white) antibodies. Arrows indicate CD4$^+$ Foxp3$^+$ cells (Tregs). Distance from Tregs in tumors (27 cells) or in spleens (37 cells) to closest Arg1$^+$ TAMs was measured.
Data are mean ± SEM, and pooled from two or three independent experiments. Statistical analysis was performed using two-tailed Student's t-tests (B). ****, $P < 0.0001$.

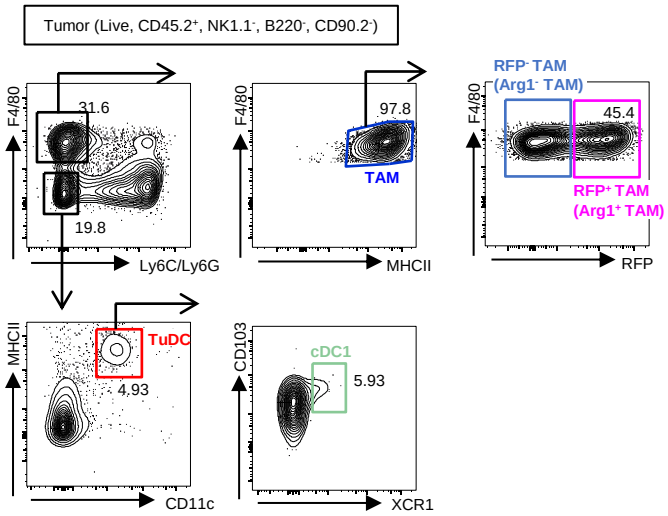

Fig.13. Representative gating strategy for the identification of TAMs and DCs in tumors.
Flow cytometry gating schematic for RFP$^+$ TAM, RFP$^-$ TAM, tumor-infiltrating DC (TuDC) and cDC1 in accordance with Ayala M, et al [7] TuDCs were identified by CD45$^+$, Ly6C$^-$, Ly6G$^-$, NK1.1$^-$, B220$^-$, CD90.2$^-$, MHCII$^+$, F4/80$^-$ and CD11c$^+$. TAMs were identified by RFP$^+$ or RFP$^-$ CD45$^+$, Ly6C$^-$, Ly6G$^-$, NK1.1$^-$, B220$^-$, CD90.2$^-$, MHCII$^+$, , F4/80$^+$, CD11b$^+$.

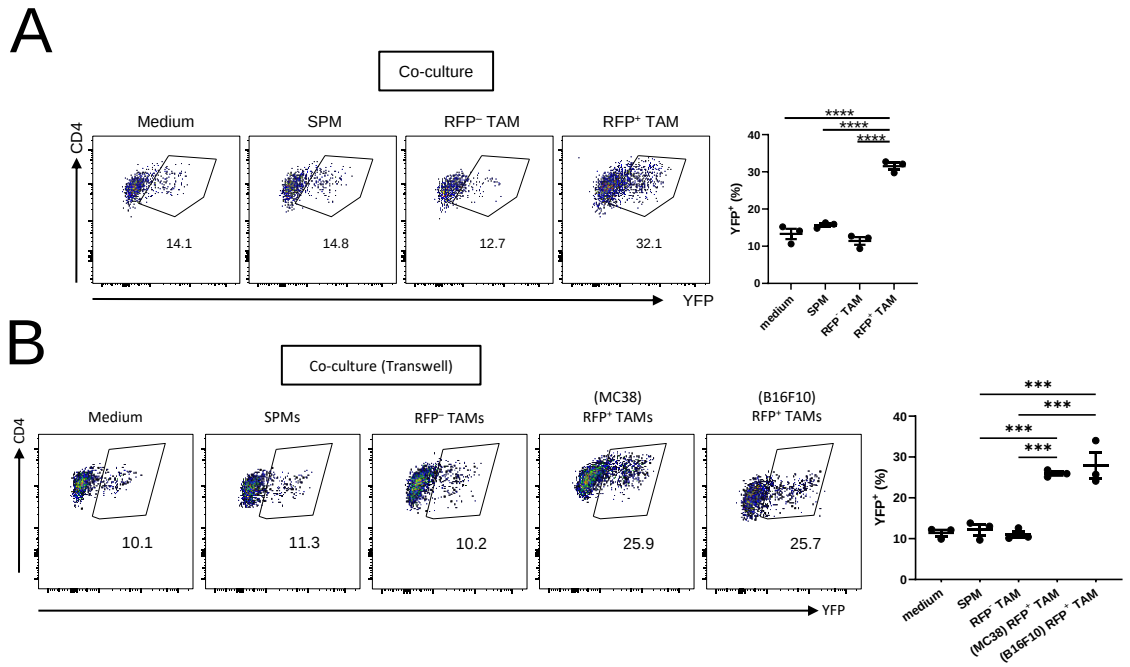

Fig.14. Arg1+TAM induces Th1-Treg differentiation in Tregs.

(**A**) Flow cytometry analysis of YFP$^-$ CD4$^+$ CD25$^+$ cells that were derived from spleens of MC38-bearing Foxp3-Cre/Tbx21-Flp/VeDTR(LF) mice and directly co-cultured with RFP$^+$ or RFP$^-$ TAMs (RFP$^+$ or RFP$^-$ CD45$^+$, Ly6C$^-$, Ly6G$^-$, NK1.1$^-$, B220$^-$, CD90.2$^-$, MHCII$^+$, F4/80$^+$, CD11b$^+$) and SPMs (CD45$^+$, Ly6C$^-$, Ly6G$^-$, NK1.1$^-$, B220$^-$, CD90.2$^-$, MHCII$^+$, F4/80$^+$, CD11b$^+$) from MC38-bearing Arg1-RFP mice. Gates show YFP$^+$ cells. Representative FACS plots and the percentages of YFP$^+$ cells pooled from three independent experiments.

(**B**) Flow cytometry analysis of YFP$^-$ CD4$^+$ CD25$^+$ cells that were derived from spleens of B16F10-bearing Foxp3-Cre/Tbx21-Flp/VeDTR(LF) mice and indirectly co-cultured with RFP$^+$ or RFP$^-$ TAMs and SPMs from MC38- or B16F10-bearing Arg1-RFP mice using transwell plates. Gates show YFP$^+$ cells. Representative FACS plots and the percentages of YFP$^+$ cells pooled from three independent experiments. Data indicate mean ± SEM. Statistical analysis was performed using one way ANOVA followed Dunnett's multiple comparisons test (A, B). ***, P < 0.001; ****, P < 0.0001

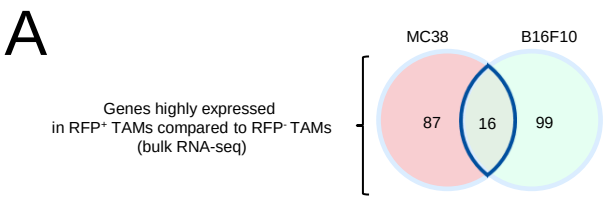

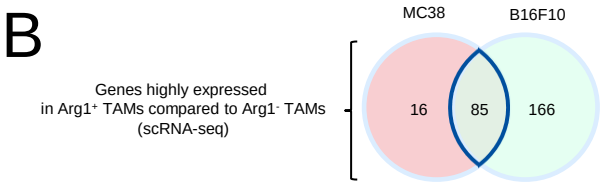

Expressed in MC38 TAM alone	Rapgef3, A430105I19Rik, Ppp1r13l, Hnmt, Snora33, P4ha2, Pelo, Lhx2, Cercam, Etv1, Hilpda, Cldn1, Ccl8, Rasip1, Slc6a8, Gm826, Marco, Optn, Gdpd1, Nkain1, Clec2f, Tctex1d4, Shf, Epb4.1l3, Tspan6, Prss50, Zfp708, Lyzl4, Fam20c, Tmeff1, Kdm5b, Trim45, Cobll1, Vat1, Slc39a4, Il7, Micall2, Pdgfrl, Peli3, Tspan8, Nr2f2, Eno2, Ctsk, Plxdc1, Sdc1, Nhsl2, Mapre3, Acot1, Spry4, Fabp5, Acad12, Ddit4, Hexim2, Spsb4, Cuedc1, 1700029I15Rik, Fam221a, Atp2b4, Fabp7, Gstm1, Gm5544, Ocln, Acer2, Hyal1, Ube2cbp, Gm3604, Dnajc22, Npff, Fbxo32, Rgs11, Cdh2, Hist1h2bp, Azin2, Pcyt1b, Cd59b, Ms4a4d, Igf1, Hhipl1, Zdhhc14, Cgnl1, Fbln2, Unc13a, P2ry2, Zfp93, Atxn1, Mill2, Pbld2
Expressed in both MC38 and B16F10 TAM	Egln3, Nos2, Folr2, Npy, Atp6v0d2, Mmp12, Rnf128, 3110021A11Rik, Prss46, Pf4, Mmp10, Htr2b, Spp1, Adm, A530064D06Rik, Arg1
Expressed in B16F10 TAM alone	D930016D06Rik, Rptoros, Cnksr2, Igf2bp2, Lyve1, Plk2, Sirt1, Ccl6, Gm1976, Gfra4, Fam20a, Fabp4, Gm4532, Map3k15, Tnfrsf26, Xk, 1190002N15Rik, Pdpn, Esam, Flrt2, Mfhas1, Nim1k, Tanc2, Lipn, Fcrlb, Ccl9, Dusp9, Tmc4, Nrg1, A230009B12Rik, Glis3, Cd163, Gm11423, Mir6376, Lhfpl1, 3010001F23Rik, Chp2, Sfn, Tslp, Dhdh, Tert, Mmp19, Art1, Emp1, Map10, Cd36, Pde9a, Gal, Gm6904, Pde8a, BC021785, Clec4d, Ptgis, Hspb9, Cftr, Sgk1, Mmp13, Fn1, Cd59a, Srgn, Ctsl, 9230116N13Rik, Zfp652os, C130071C03Rik, Hmox1, Fam78b, Ccdc15, Basp1, Pcp4l1, Oit3, Klf8, Raet1e, Slc22a4, Oas3, Kifc2, Cacna1d, Ednrb, Il7r, Ecm1, Ppbp, Cxcl3, Jag1, Trim12a, C130026I21Rik, S1pr1, Dpf3, Rab39, Thbs1, Fam227b, Ankrd6, Slc7a2, 1700001O22Rik, Gm20604, Rtkn2, AA474331, Adam33, Tnfaip6, Ccl24, Scml4

Expressed in MC38 TAM alone	Fcgr3,Rcbtb2,Apoc2,S100a6,Rnase4,Sgk1,Aldoc,Pla2g7,Selenom,Gatm,Ms4a4a, Plau,Fbxo32,Apoe,Thbs1
Expressed in both MC38 and B16F10 TAM	Arrdc4,Fth1,Pkm,Bcl2a1b,Vegfa,Sdc3,Egln1,Anpep,Aprt,Ndrg1,Mxi1,Lrp1,Capg, Zfp36l1,Ier3,Emp1,Vdac1,Ldha,Clec4d,Bsg,Sdc4,Fn1,Pgam1,Ctsl,Stab1,Mif, AA467197,C5ar1,Hmox1,Cstb,Spp1,Basp1,Arg1,Anxa2,Bnip3,Slc2a1,Slc7a2, Fcgr2b,Slc16a3,Ctsd,Gsn,Egln3,Abca1,Dab2,Gapdh,Eif4ebp1,Gpi1,Hilpda,Pdpn, Mmp12,Cd9,Plin2,P4hb,Cd14,Cxcl2,F10,Fam162a,Cd68,Rgcc,Pf4,Pid1,Adam8, Lgals3,Fabp5,Ddit4,Msr1,Srgn,Mt1,Plp2,Itgam,Anxa3,Ecm1,Tmem189,Il7r,Prelid1, C3ar1,Lgals1,Pgk1,Eno1,Grina,Tmem37,Aldoa,Trem2,Tpi1,Ero1l
Expressed in B16F10 TAM alone	Ap2s1,Selenbp1,Igf2bp2,Cdk4,Ccl6,Ugdh,Bnip3l,S100a10,Cox4i2,Tmem120a,Npepps, Pdia4,Dctn3,Lrp12,Ndufab1,Osbpl8,Slc7a8,Elob,Gys1,Rnf126,Ftl1-ps1,Mmp14, Fcrlb,Ccl9,Slc15a3,Anxa4,Mgarp,Odc1,St8sia4,Snx5,Bst1,Pld3,Uap1l1,Bcar3,Maf, Atp6v1c1,Clec4n,Baiap2,Prelid2,Hmga1,Sdc1,Pafah1b3,App,Lpl,Pgm1,Atp6v1a, Spg21,Vps29,Anxa1,Mmp13,Slamf7,Rhoc,Ccl7,Pdcd5,Glrx,Syngr1,P4ha1,Ccl12, Flrt3,Rgs1,Rbpj,Acod1,Adss1l1,Arl3,Snx6,Pfkl,Hsbp1,Cxcl3,Tec,Nt5dc2,Ppp1r14b, Galk1,Ccl24,Bax,Ankrd37,Prdx6,Timp1,Txn1,Eea1,Mtss1,Snx3,Anxa5,Por,Bcl2l1, Igf2r,Nos2,Il1rn,Myo1e,4930430E12Rik,Eno1b,Inhba,Eid1,Tbcb,Rgl1,Raph1,Cfp, Lhfpl2,Grhpr,Gla,Kcnn4,Tnfsf9,Calm3,Tmem171,Cd63,Gabarap,Tubb5,Psmb6,F7, Gna13,Slc37a2,Itsn1,Ccl2,Fam20c,Lilr4b,Upp1,Cd300lf,Impdh1,Vim,Vat1,Creb5,Hk1, Pebp1,Fcgr1,Arhgap10,Spryd7,Cd36,Fnip2,Gpnmb,Ptgs2,Gm14636,Tspan3,Plgrkt, Il1a,Rab11a,Higd1a,Ndufv3,Psma6,Rsbn1,Rbx1,Impa2,Lmna,Id2,Acp1,Lgmn,Ftl1, Bri3,Ms4a7,Gde1,Ap3s1,F13a1,Card19,Mrc1,Yif1b,Psmd8,Fkbp1a,Galnt6,Errfi1, Slc27a1,Pmp22,Ctsb,Akr1a1,Cxcl1,Yipf4,Dhrs3,Appl2,Cd84

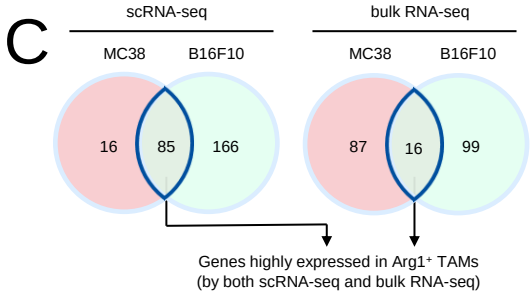

Genes highly expressed in Arg1+ TAMs
(by both scRNA-seq and bulk RNA-seq)

Gene name	Humoral factor	Not expressed In SPM
Arg1	✓	✓
Mmp12	✓	
Egln3		✓
Spp1	✓	✓
Pf4	✓	✓

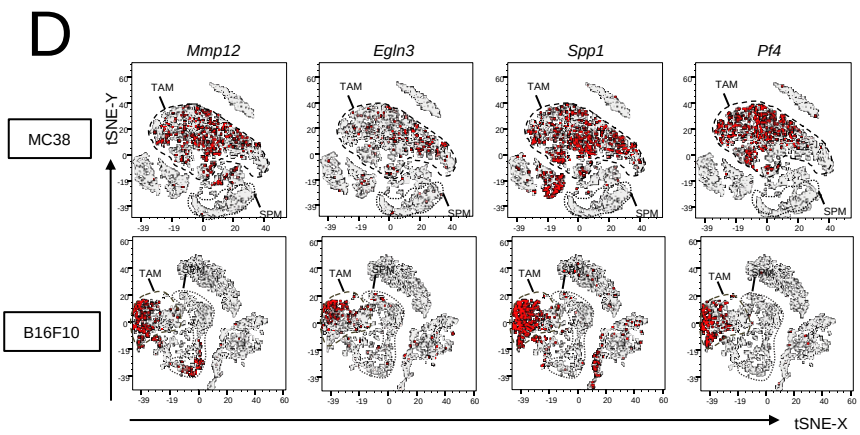

Fig.15. Comparison of gene expression between Arg1$^+$ TAM and Arg1$^-$TAM.

(**A**) Common genes that are differentially expressed between RFP$^+$ or RFP$^-$ TAMs from MC38- or B16F10-bearing Arg1-RFP mice (n = 3 per group) in the bulk RNA-seq. The indicated 16 genes are overlapped between 103 upregulated genes (|Fold change| > 2 and p-value < 0.05) in RFP$^+$ TAMs from MC38 tumors and 115 upregulated genes (|Fold change| > 2 and p-value < 0.05) in RFP$^+$ TAMs from B16F10 tumors. Table shows list of genes expressed in RFP$^+$ TAMs from both tumors or from either tumor.

(B) Common genes that are differentially expressed between Arg1$^+$ or Arg1$^-$ TAMs from MC38- or B16F10-bearing Cx3cr1-Cre/VeDTR(ΔFRT) mice (n = 3 per group), which were resulted from the analysis of the scRNA-seq data (Fig. S2D, S2E and S2F). The indicated 85 genes are overlapped between 101 upregulated genes (|Fold change| > 1.2 and p-value < 0.05) in Arg1$^+$ TAMs from MC38 tumors and 251 upregulated genes (|Fold change| > 1.2 and p-value < 0.05) in Arg1$^+$ TAMs from B16F10 tumors. Table shows list of genes expressed in Arg1$^+$ TAMs from both tumors or from either tumor.

(**C**) Common genes that are differentially expressed between RFP$^+$ or RFP$^-$ TAMs from MC38- or B16F10-bearing Arg1-RFP mice (n = 3 per group) in the bulk RNA-seq (left). Common genes that are differentially expressed between Arg1$^+$ or Arg1$^-$ TAMs from MC38- or B16F10-bearing Cx3cr1-Cre/DTR(ΔFRT) mice (n = 3 per group) in the scRNA-seq (right). Table shows the overlapped 5 genes.

(**D**) t-SNE plot showing of mRNA expression of indicated genes in TAMs and SPMs from MC38- or B16F10-bearing mice.

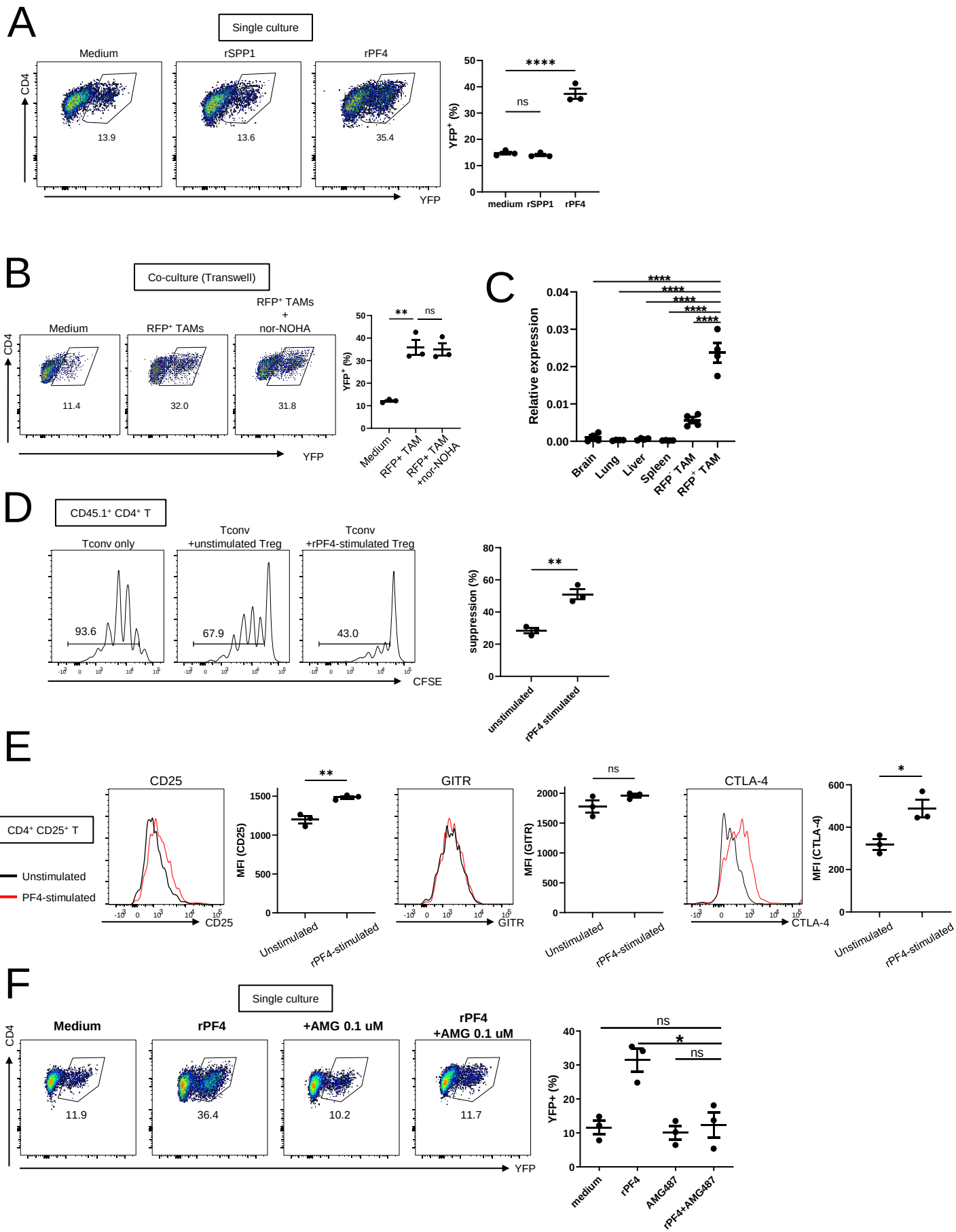
A
Single culture
Medium
rSPP1
rPF4
CD4
13.9
13.6
35.4
YFP
YFP+ (%)
****
ns
medium
rSPP1
rPF4
B
Co-culture (Transwell)
RFP+ TAMs + nor-NOHA
Medium
RFP+ TAMs
11.4
32.0
31.8
**
ns
Medium
RFP+ TAM
RFP+ TAM +nor-NOHA
C
Relative expression
Brain
Lung
Liver
Spleen
RFP- TAM
RFP+ TAM
D
CD45.1+ CD4+ T
Tconv only
Tconv +unstimulated Treg
Tconv +rPF4-stimulated Treg
93.6
67.9
43.0
CFSE
suppression (%)
unstimulated
rPF4 stimulated
E
CD4+ CD25+ T
Unstimulated
PF4-stimulated
CD25
GITR
CTLA-4
MFI (CD25)
MFI (GITR)
MFI (CTLA-4)
Unstimulated
rPF4-stimulated
F
Single culture
Medium
rPF4
+AMG 0.1 uM
rPF4 +AMG 0.1 uM
11.9
36.4
10.2
11.7
YFP+ (%)
medium
rPF4
AMG487
rPF4+AMG487

Fig. 16. Arg1$^+$ TAMs secrete PF4 that polarizes Tregs into Th1-Tregs.

(**A**) Flow cytometry of YFP$^-$ CD4$^+$ CD25$^+$ cells that were derived from spleens of B16F10-bearing Foxp3-Cre/Tbx21-Flp/VeDTR(LF) mice and subsequently stimulated with recombinant PF4 protein (rPF4) or recombinant SPP1 protein (rSPP1). Gates show YFP$^+$ cells. Representative FACS plots and the percentages of YFP$^+$ cells pooled from three independent experiments.

(**B**) Flow cytometry analysis of YFP$^-$ CD4$^+$ CD25$^+$ cells that were derived from spleens of MC38-bearing Foxp3-Cre/Tbx21-Flp/VeDTR(LF) mice and directly co-cultured with RFP$^+$ TAMs in tumors (Arg1$^+$ TAMs) from MC38-bearing Arg1-RFP mice w/o nor-NOAH. Gates show YFP$^+$ cells. Representative FACS plots and the percentages of YFP$^+$ cells pooled from three independent experiments.

(**C**) Quantitative RT-PCR (q-PCR) analysis to detect Pf4 mRNA levels of tissue macrophages from MC38-bearing wild-type mice. Tissue msacrophages were identified by expression of the cell surface marker (Brain (microglia): Cx3cr1$^+$, P2RY12$^+$, Lung (alveolar macrophage): CD11c$^+$, SiglecF$^+$, Liver (Kupffer cell): CD11b^{low}, F4/80$^+$, SPMs, RFP$^+$ or RFP$^-$ TAMs).

(**D**) Flow cytometry analysis of carboxyfluorescein succinimidyl ester (CFSE)-labeled naive CD4$^+$ T cells (Tconv) co-cultured with YFP- CD4$^+$ CD25$^+$ cells that were derived from spleens of B16F10-bearing Foxp3-Cre/Tbx21-Flp/VeDTR(LF) mice and stimulated with rPF4. Representative histograms and the percentages of YFP$^+$ cells pooled from three independent experiments.

(**E**) Flow cytometry analysis of indicated surface markers on YFP$^-$ CD4$^+$ CD25$^+$ cells that were derived from spleens of B16F10-bearing Foxp3-Cre/Tbx21-Flp/VeDTR(LF) mice and stimulated with rPF4. Representative histogram overlays and measurements of mean fluorescence intensity (MFI).

(**F**) Flow cytometry analysis of YFP$^-$ CD4$^+$ CD25$^+$ cells that were derived from spleens of B16F10-bearing Foxp3-Cre/Tbx21-Flp/VeDTR(LF) mice and subsequently stimulated with rPF4 w/o AMG487. Gates show YFP$^+$ cells. Representative FACS plots and the percentages of YFP$^+$ cells pooled from three independent experiments.

Data indicate mean ± SEM. Statistical analysis was performed using one way ANOVA followed Dunnett's multiple comparisons test (A, B, C, F) and two-tailed Student’s t-tests (D, E). *, $P < 0.05$; **, $P < 0.01$; ns, nonsignificant.

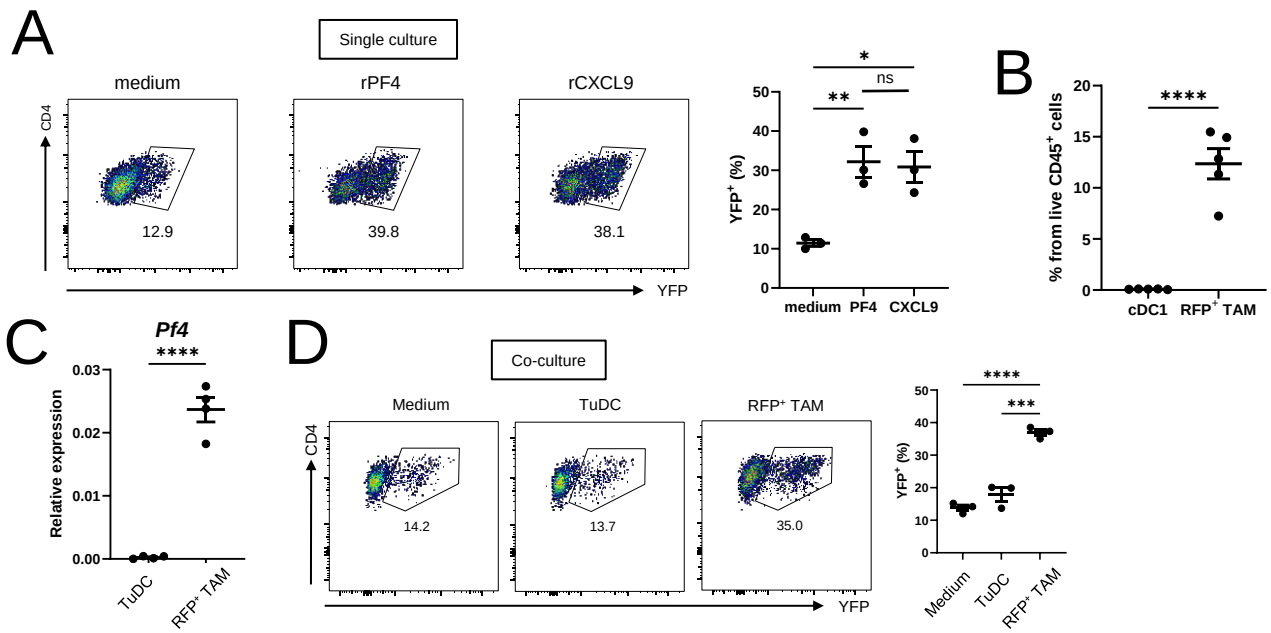

Fig.17. TuDCs did not induce Th1-Treg polarization.

(**A**) Flow cytometry of YFP$^-$ CD4$^+$ CD25$^+$ cells that were derived from spleens of B16F10-bearing Foxp3-Cre/Tbx21-Flp/VeDTR(LF) mice and subsequently stimulated with recombinant PF4 protein or recombinant CXCL9 protein. Gates show YFP$^+$ cells.

(**B**) Percentages of RFP$^+$ TAMs and cDC1s in tumor derived from Arg1-RFP mice that were s.c. implanted with MC38 cells. n = 5 per group.

(**C**) q-PCR analysis to detect *Pf4* mRNA levels of TuDCs and RFP$^+$ TAMs from MC38-bearing Arg1-RFP mice.

(**D**) Flow cytometry analysis of YFP$^-$ CD4$^+$ CD25$^+$ cells that were derived from spleens of MC38-bearing Foxp3-Cre/Tbx21-Flp/VeDTR(LF) mice and indirectly co-cultured with TuDCs or RFP$^+$ TAMs from MC38-bearing Arg1-RFP mice using transwell plates. Gates show YFP$^+$ cells. Representative FACS plots and the percentages of YFP$^+$ cells pooled from three independent experiments.

Data are mean ± SEM, and pooled from two or three independent experiments. Statistical analysis was performed using two-tailed Student's t-tests (B, C), one way ANOVA followed Dunnett's multiple comparisons test (A, D). *, $P < 0.05$; **, $P < 0.01$; ***, $P < 0.001$; ****, $P < 0.0001$; ns, nonsignificant.

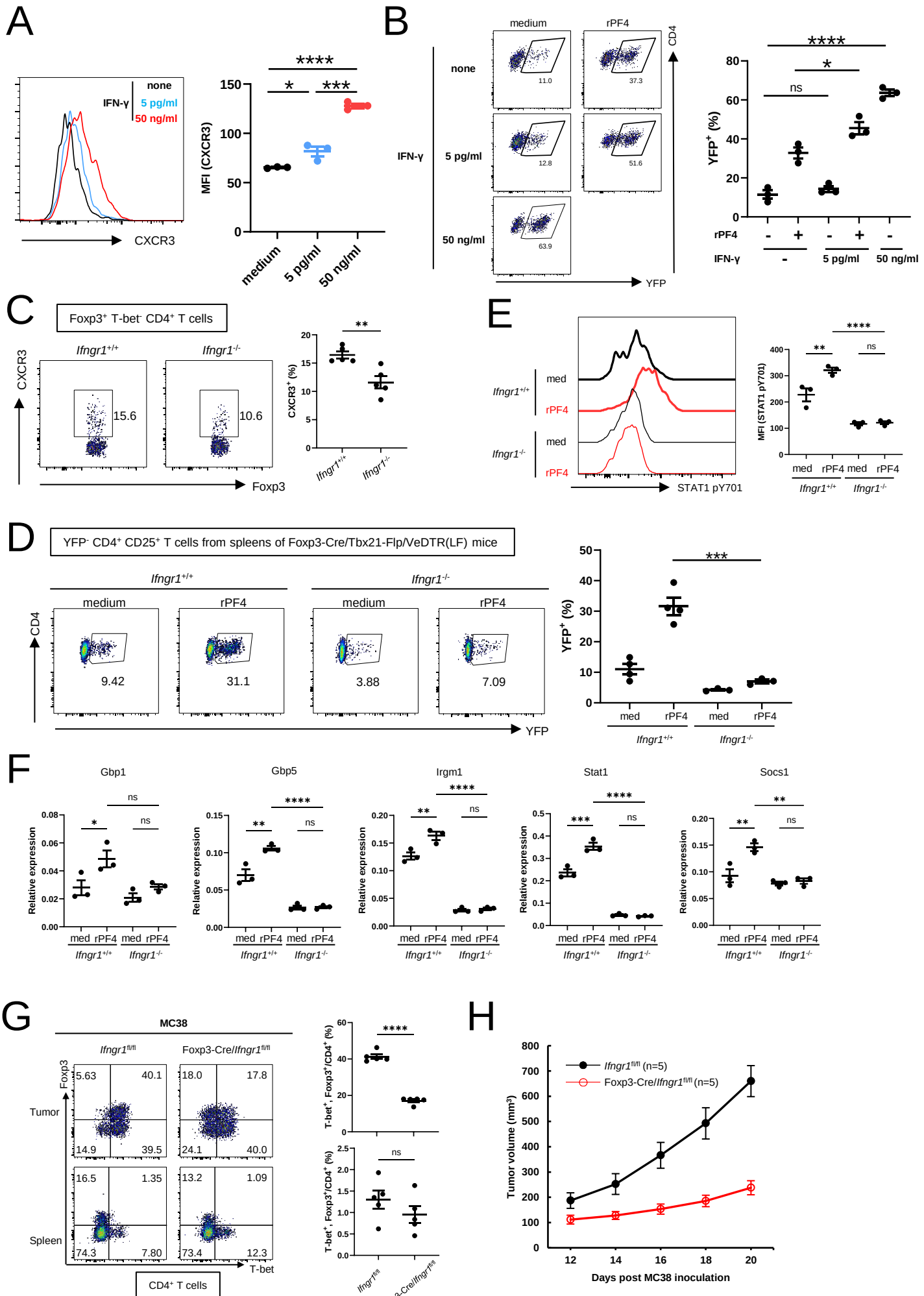
A
IFN-γ
none
5 pg/ml
50 ng/ml
CXCR3
MFI (CXCR3)
****
*
***
medium
5 pg/ml
50 ng/ml
B
medium
rPF4
none
IFN-γ
5 pg/ml
50 ng/ml
11.0
37.3
12.8
51.6
63.9
CD4
YFP
YFP+ (%)
****
*
ns
rPF4
IFN-γ
C
Foxp3+ T-bet- CD4+ T cells
Ifngr1+/+
Ifngr1-/-
CXCR3
15.6
10.6
Foxp3
CXCR3+ (%)
**
E
med
rPF4
STAT1 pY701
MFI (STAT1 pY701)
****
**
ns
D
YFP- CD4+ CD25+ T cells from spleens of Foxp3-Cre/Tbx21-Flp/VeDTR(LF) mice
medium
rPF4
9.42
31.1
3.88
7.09
CD4
YFP
YFP+ (%)
***
F
Gbp1
Gbp5
Irgm1
Stat1
Socs1
Relative expression
ns
*
**
***
****
med
rPF4
G
MC38
Ifngr1fl/fl
Foxp3-Cre/Ifngr1fl/fl
Foxp3
Tumor
Spleen
5.63
40.1
14.9
39.5
18.0
17.8
24.1
40.0
16.5
1.35
74.3
7.80
13.2
1.09
73.4
12.3
T-bet
CD4+ T cells
T-bet+, Foxp3+/CD4+ (%)
T-bet+, Foxp3-/CD4+ (%)
****
ns
H
Ifngr1fl/fl (n=5)
Foxp3-Cre/Ifngr1fl/fl (n=5)
Tumor volume (mm3)
Days post MC38 inoculation

Fig. 18. Role of IFN-γ in PF4-induced Th1-Treg polarization.

(**A**) Flow cytometry of YFP$^-$ CD4$^+$ CD25$^+$ CXCR3$^-$ cells that were derived from spleens of MC38-bearing Foxp3-Cre/Tbx21-Flp/VeDTR(LF) mice and subsequently stimulated with 5 pg/ml or 50 ng/ml IFN-γ. Representative histogram overlays and measurements of mean fluorescence intensity (MFI).

(**B**) Flow cytometry of YFP$^-$ CD4$^+$ CD25$^+$ CXCR3$^-$ cells that were derived from spleens of MC38-bearing Foxp3-Cre/Tbx21-Flp/VeDTR(LF) mice and subsequently stimulated with recombinant PF4 protein (rPF4) in addition to 5 pg/ml or 50 ng/ml IFN-γ. Gates show YFP$^+$ cells. Representative FACS plots and the percentages of YFP$^+$ cells pooled from three independent experiments.

(**C**) CXCR3 expression in splenic Foxp3$^+$ T-bet$^-$ CD4$^+$ T cells. Representative plot (left) and total results (right) (*Ifngr1*$^{+/+}$: n=5, *Ifngr1*$^{-/-}$: n = 5).

(**D**) Flow cytometry analysis of YFP$^-$ CD4$^+$ CD25$^+$ cells that were derived from spleens of B16F10-bearing *Ifngr1*$^{+/+}$ (n = 4) or *Ifngr1*$^{-/-}$ (n = 4) Foxp3-Cre/Tbx21-Flp/VeDTR(LF) mice and subsequently stimulated with rPF4. Gates show YFP$^+$ cells. Representative FACS plots and the percentages of YFP$^+$ cells pooled from two independent experiments.

(**E**) Flow cytometry to assess phospho-STAT1 levels in *Ifngr1*$^{+/+}$ (n = 3) or *Ifngr1*$^{-/-}$ (n = 3) YFP$^-$ CD4$^+$ CD25$^+$ cells that were derived from spleens of MC38-bearing Foxp3-Cre/Tbx21-Flp/VeDTR(LF) mice and unstimulated or stimulated with rPF4 for 3 hrs.

(**F**) q-PCR analysis to detect mRNA levels of indicated genes in *Ifngr1*$^{+/+}$ (n = 3) or *Ifngr1*$^{-/-}$ (n = 3) YFP$^-$ CD4$^+$ CD25$^+$ cells that were derived from spleens of MC38-bearing Foxp3-Cre/Tbx21-Flp/VeDTR(LF) mice and unstimulated or stimulated with rPF4 for 24 hrs.

(**G**) Flow cytometry analysis of CD4$^+$ T cells of derived from indicated tissues of *Ifngr1*$^{fl/fl}$ mice or Foxp3-Cre/*Ifngr1*$^{fl/fl}$ mice that were s.c. implanted with MC38 tumor. Representative FACS plots and the percentages of Foxp3 and T-bet double-positive cells in CD4$^+$ T cells in tumors or spleens. n = 5 per group.

(**H**) Growth of s.c. implanted MC38 tumors in *Ifngr1*$^{fl/fl}$ mice or Foxp3-Cre/*Ifngr1*$^{fl/fl}$ mice (indicated numbers of mice per group).

Data are mean ± SEM, and pooled from two-three independent experiments. Statistical analysis was performed using two-tailed Student's t-tests (C, D, G) and one way ANOVA followed Dunnett's multiple comparisons test (A, B, E, F). (*, P < 0.05; **, P < 0.01; ***, P < 0.001, **** P < 0.0001; ns, nonsignificant.

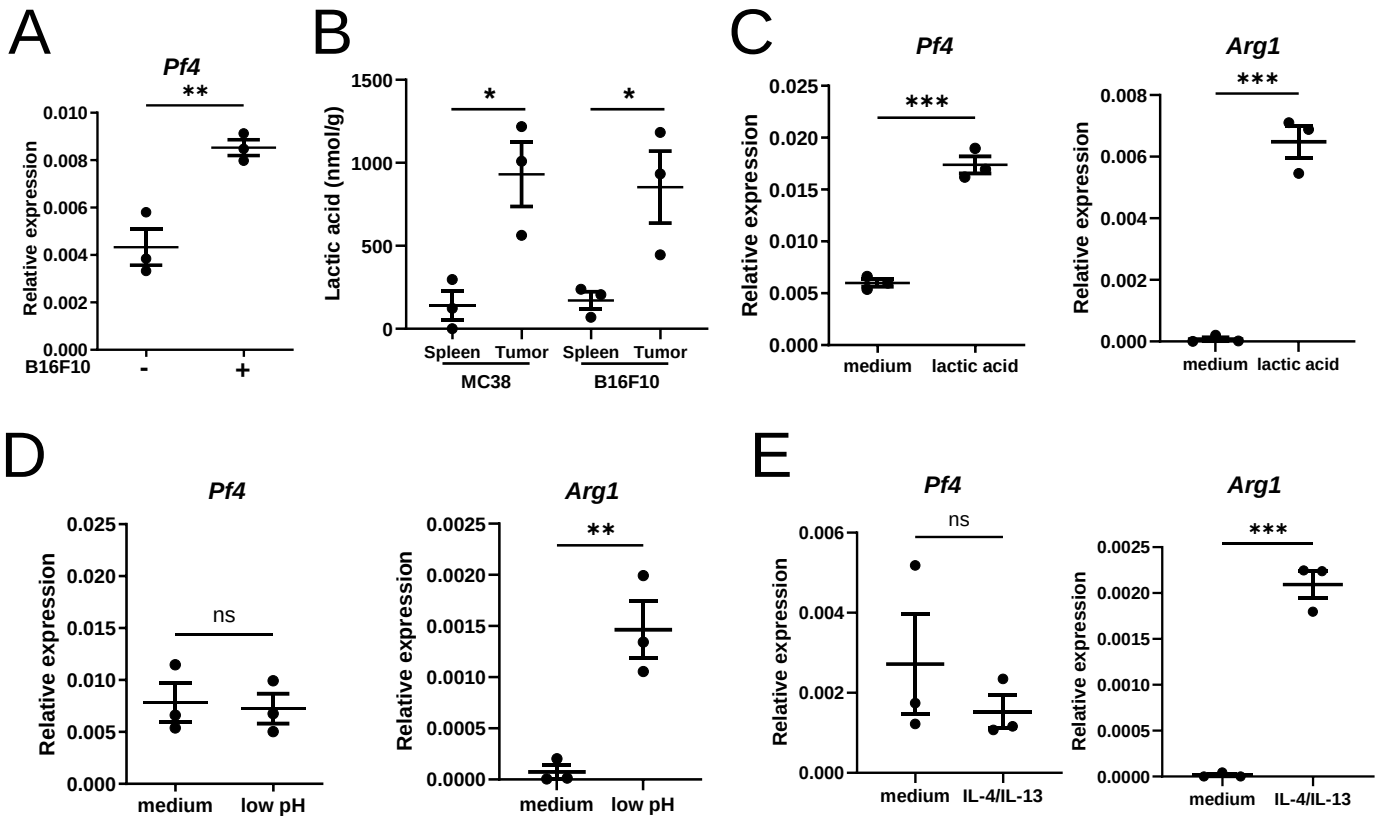

Fig. 19. Differential expression pattern of Pf4 and Arg1 mRNA in macrophages.

(**A**) Quantitative RT-PCR (q-PCR) analysis to detect *Pf4* mRNA levels of $CD11b^+$ $CD45^+$ cells of spleens from wild-type mice (n = 3 per group) that were indirectly co-cultured with B16F10 cells using transwell for 24 hrs.

(**B**) Concentrations of suspensions of indicated tissues from MC38- or B16F10-bearing wild-type mice (n = 4 per group) were measured by the L-Lactate Assay Kit.

(**C-E**) Quantitative RT-PCR (q-PCR) analysis to detect Pf4 or Arg1 mRNA levels of $CD45^+$ $CD11b^+$ $Ly6G^-$ cells of spleens from wild-type mice (n = 3 per group) in the absence or presence of lactic acid (25 mM) (**C**), low pH (pH6.0) medium (**D**) or IL-4 (20 ng/ml) and IL-13 (20 ng/ml) for 12 hrs (**E**).

Data are mean ± SEM, and pooled from three independent experiments. Statistical analysis was performed using two-tailed Student's t-tests (A, B, C, D, E). *, $P < 0.05$; **, $P < 0.01$; ***, $P < 0.001$; ns, nonsignificant.

4. Genetic PF4 inactivation reduces intra-tumoral Th1-Tregs and tumor growth

I examined the *in vivo* contribution of PF4 to the high Th1-Treg ratios in the TME. $Pf4^{-/-}$ mice were generated using CRISPR/Cas9 genome editing (**Fig. 20A**). $Arg1^{+}$ tumor-infiltrating $CD11b^{+}$ $Ly6G^{-}$ cells were isolated from both wild-type and $Pf4^{-/-}$ mice in the Arg1-RFP strain background, and tested for PF4 protein levels using ELISA (**Fig. 21A** and **21B**). While high PF4 protein levels were observed in the sera and $Arg1^{+}$ tumor-infiltrating $CD11b^{+}$ $Ly6G^{-}$ cells of wild-type mice, no PF4 proteins were detected in the $Pf4^{-/-}$ counterparts (**Fig. 21A** and **21B**), suggesting that PF4 production was abolished from $Arg1^{+}$ TAMs and non-macrophage cell types such as platelets in $Pf4^{-/-}$ mice. When comparing tumor growth in wild-type and $Pf4^{-/-}$ mice, I found that $Pf4^{-/-}$ mice showed delayed tumor growth in the two cancer models tested (MC38 and B16F10) (**Fig. 21C** and **21D**). Upon examining the Th1-Treg ratios in the tumors and spleens by flow cytometry, I found that the Th1-Treg ratios in the tumors of $Pf4^{-/-}$ mice were significantly lower than those of wild-type mice (**Fig. 21E** and **21F**). In sharp contrast, the Th1-Treg ratios in the spleens were comparable between tumor-bearing wild-type and $Pf4^{-/-}$ mice (**Fig. 21E** and **21F**), suggesting that PF4 is specifically involved in intra-tumoral Th1-Treg accumulation and promotes tumor growth.

To assess to what degree macrophage-derived PF4 contributes to Th1-Treg accumulation and tumor growth, I engineered mice with floxed alleles of the Pf4 gene ($Pf4^{fl/fl}$) by CRISPR/Cas9 genome editing (**Fig. 20B**), and generated Cx3cr1-Cre/$Pf4^{fl/fl}$ mice on the Arg1-RFP strain background. Although serum PF4 proteins were not detected in the conventional $Pf4^{-/-}$ mice (**Fig. 21A**), serum PF4 was present in the Cx3cr1-Cre/$Pf4^{fl/fl}$ counterparts (**Fig. 21G**). In contrast, PF4 protein production from $Arg1^{+}$ tumor-infiltrating $CD11b^{+}$ $Ly6G^{-}$ cells was abolished in MC38 tumor-bearing Cx3cr1-Cre/$Pf4^{fl/fl}$ mice (**Fig. 21H**), suggesting that PF4 production is defective in Arg1+ TAMs but intact in non-macrophage populations such as platelets. Tumor growth was reduced in the tumor-bearing Cx3cr1-Cre/$Pf4^{fl/fl}$ mice (**Fig. 21I**). Although the ratios of Th1-Treg in spleens of Cx3cr1-Cre/$Pf4^{fl/fl}$ mice were comparable to those in control mice, those in tumors from Cx3cr1-Cre/$Pf4^{fl/fl}$ mice were significantly reduced compared to control mice (**Fig. 21J**). Taken together, these results suggest that macrophage-derived PF4 plays a major role in promoting Th1-Treg accumulation in TME and contributing to the tumor growth.

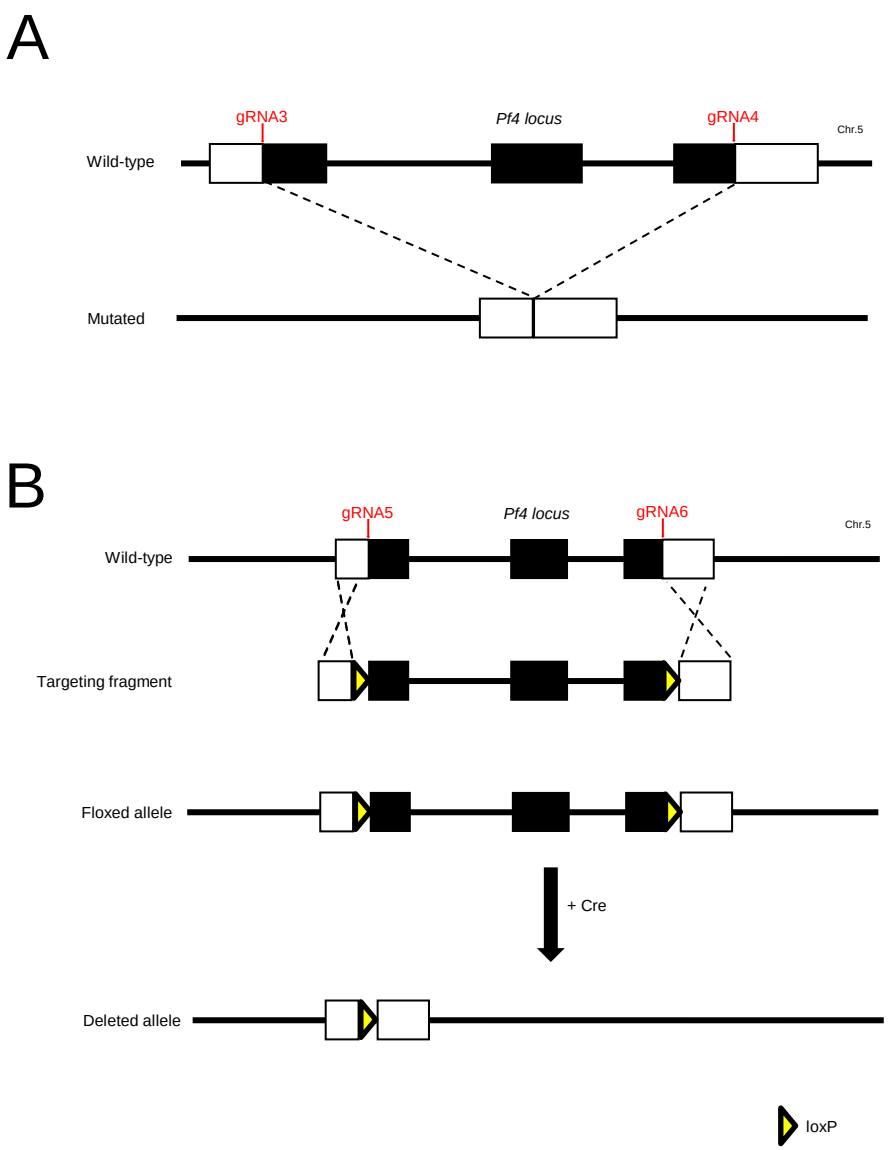

Fig. 20. Generation of *Pf4*$^{-/-}$ or *Pf4*$^{fl/fl}$ mice.
(**A, B**) Targeting strategy for the *Pf4* locus to delete (**A**) or flox (**B**) the entire coding region.

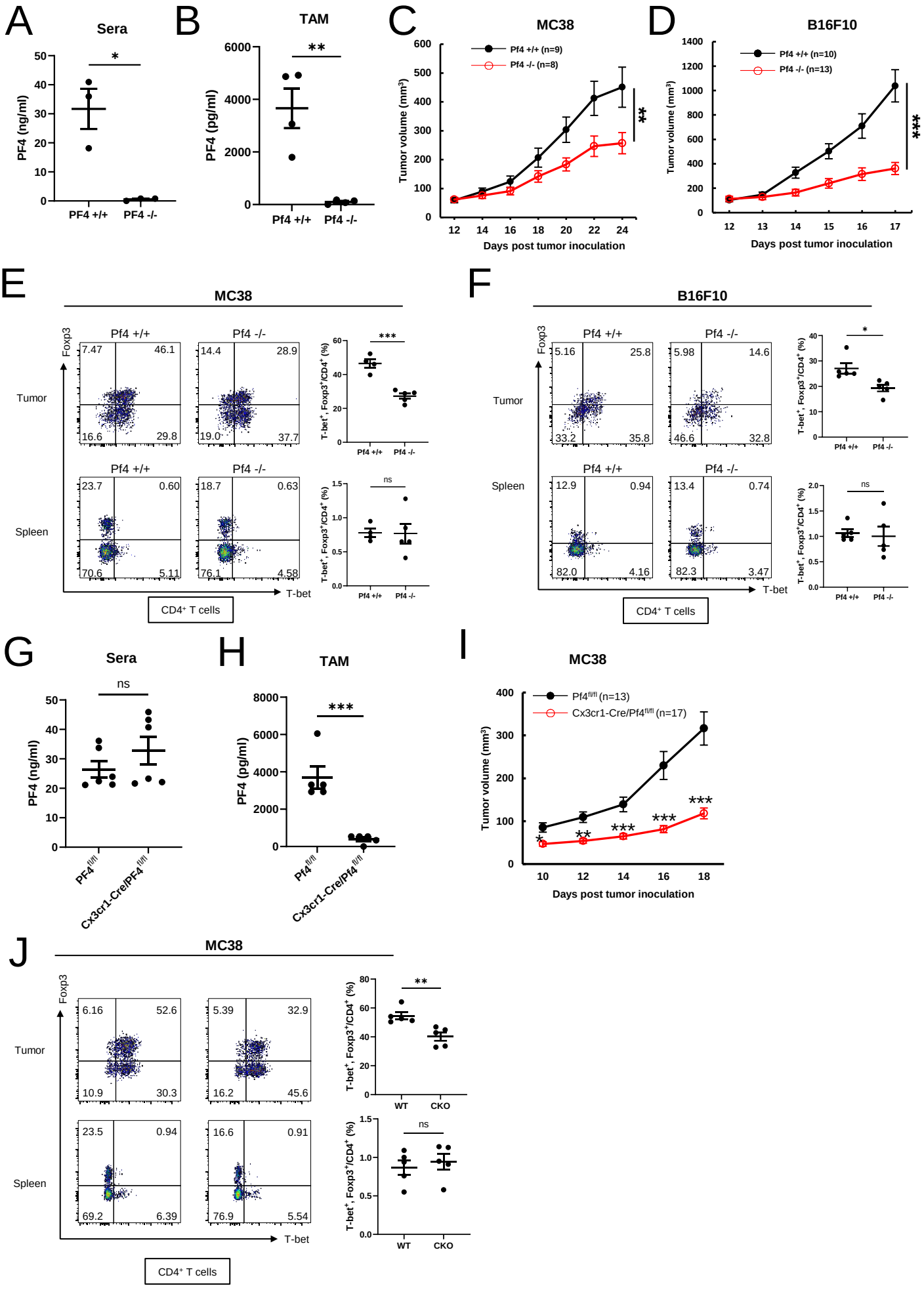
A
Sera
PF4 (ng/ml)
PF4 +/+
PF4 -/-
B
TAM
PF4 (pg/ml)
C
MC38
Pf4 +/+ (n=9)
Pf4 -/- (n=8)
Tumor volume (mm³)
Days post tumor inoculation
D
B16F10
Pf4 +/+ (n=10)
Pf4 -/- (n=13)
E
MC38
Foxp3
T-bet
Tumor
Spleen
CD4⁺ T cells
T-bet⁺, Foxp3⁺/CD4⁺ (%)
F
B16F10
G
Sera
ns
PF4 fl/fl
Cx3cr1-Cre/PF4 fl/fl
H
TAM
I
MC38
Pf4fl/fl (n=13)
Cx3cr1-Cre/Pf4fl/fl (n=17)
J
MC38
WT
CKO

Fig. 21. Genetic inactivation of PF4 inhibits tumor growth and accumulation of Th1-Tregs in tumors.

(**A, B**) Concentrations of PF4 proteins in the sera (A) or the culture supernatants of RFP^+ $CD45^+$ $CD11b^+$ $Ly6G^-$ cells in tumors (B) from MC38 tumor-bearing Arg1-RFP/$Pf4^{+/+}$ mice or Arg1-RFP/$Pf4^{-/-}$ mice (n = 4 per group) were measured by ELISA.

(**C, D**) Growth of s.c. implanted MC38 (C) or B16F10 (D) tumors in $Pf4^{+/+}$ mice or $Pf4^{-/-}$ mice (indicated numbers of mice per group are shown).

(**E, F**) Flow cytometry analysis of $CD4^+$ T cells of derived from indicated tissues of $Pf4^{+/+}$ mice or $Pf4^{-/-}$ mice that were s.c. implanted with MC38 (E) or B16F10 (F). Representative FACS plots and the percentages of Foxp3 and T-bet double-positive cells in $CD4^+$ T cells in tumors or spleens. n = 4-5 per group.

(**G, H**) Concentrations of PF4 proteins in the sera (A) or the culture supernatants of RFP^+ $CD45^+$ $CD11b^+$ $Ly6G^-$ cells in tumors (B) from MC38-bearing Arg1-RFP/$Pf4^{fl/fl}$ mice or Arg1-RFP/Cx3cr1-Cre/$Pf4^{fl/fl}$ mice (n = 5-6 per group) were measured by ELISA.

(**I**) Growth of s.c. implanted MC38 tumors in $Pf4^{fl/fl}$ mice or Cx3cr1-Cre/$Pf4^{fl/fl}$ mice (indicated numbers of mice per group are shown).

(**J**) Flow cytometry analysis of $CD4^+$ T cells of derived from indicated tissues of $Pf4^{fl/fl}$ mice or Cx3cr1-Cre/$Pf4^{fl/fl}$ mice that were s.c. implanted with MC38 tumor. Representative FACS plots and the percentages of Foxp3 and T-bet double-positive cells in $CD4^+$ T cells in tumors or spleens. n = 4-5 per group.

Data indicate mean ± SEM, and pooled from two to three independent experiments. Statistical analysis was performed using two-tailed Student's t-tests (A, B,C, D, E, F, G, H, I, J). *, $P < 0.05$; **, $P < 0.01$; ***, $P < 0.001$; ns, nonsignificant.

5. PF4 neutralization by antibody decreases intra-tumoral Th1-Treg ratios and tumor growth

Genetic inactivation of PF4 decreased the ratios of Th1-Tregs in tumors and reduced tumor growth (**Fig. 21**). Recombinant PF4 protein has been previously reported to stimulate human $CD4^+$ T cells to express Foxp3 and T-bet [60], prompting us to examine whether systemic PF4 neutralization by a PF4-specific antibody may have immunotherapeutic effects on tumors. However, a commercially available anti-PF4 (com-anti-PF4) mAb barely neutralized the recombinant PF4 protein-induced Treg polarization into Th1-Tregs (**Fig. 22A**). I therefore generated an independent anti-PF4 mAb (#6-1-5) that neutralized PF4-induced conversion of Tregs to Th1-Tregs (**Fig. 22A**). My anti-PF4 mAb (#6-1-5) specifically detected PF4 alone, without recognizing CXCL9, CXCL10 and CXCL11 (**Fig. 22B**), all of which are other ligands for CXCR3 [54]. I assessed whether the administration of anti-PF4 mAb (#6-1-5) is immunotherapeutic to B16F10 melanoma and MC38 colorectal tumors. Anti-PF4 mAb (#6-1-5) was administered at 10 days post-tumor inoculation, which is the same timing of DT administration in Cx3cr1-Cre/Arg1-Flp/VeDTR(LF) mice (**Fig. 4E** and **4F**). The growth of B16F10 melanoma in anti-PF4 mAb (#6-1-5)-treated mice was significantly diminished, whereas reduction of MC38 colorectal tumors did not reach significance (**Fig. 23A**). When the anti-PF4 mAb (#6-1-5) was administered at 3 days post-tumor inoculation, I observed growth inhibition of both B16F10 and MC38 tumors (**Fig. 23B**). When comparing the Th1-Treg ratios in the tumors of anti-PF4 mAb-treated or untreated mice, I found that the Th1-Treg ratios in the tumors of anti-PF4 mAb-treated mice were significantly decreased compared to those in isotype control mAb-treated control mice (**Fig. 23C** and **23D**). In contrast, the Th1-Treg ratios in the spleens were comparable between both treatment groups (**Fig. 23C** and **23D**), reminiscent of the phenotypes of PF4-deficient mice **(Fig. 21E**, **21F** and **21J**). Consistently, when MC38 or B16F10 tumor-bearing Foxp3-Cre/Tbx21-Flp/VeDTR(LF) mice were examined for YFP^+ cell ratios in tumors and spleens, the anti-PF4 mAb treatment decreased Th1-Treg ratios in tumors but not in spleens (**Fig. 24A** and **24B**). Upon examining anti-tumor immunity, the ratios of IFN-γ^+/TNF-α^+ $CD4^+$ T cells or $CD8^+$ T cells in anti-PF4 mAb-treated mice were significantly increased compared to those in tumors of control mice (**Fig. 23E** and **23F**). Collectively, these data suggest that neither $Arg1^+$ TAM depletion nor PF4 neutralization affects the migration of Tregs to the TME. I asked whether the anti-angiogenetic but not anti-tumor immunological functions of PF4 might affect tumor growth [61], however, anti-PF4 mAb administration did not change intra-tumor vascular architecture (**Fig. 25A**). Exogenous and overexpressed PF4 can directly stimulate $CD8^+$ T cells via CXCR3 to activate caspase-3, leading to apoptosis

and inhibition of anti-tumor immunity, respectively [62]. However, anti-PF4 mAb administration did not alter activated caspase-3 levels in intra-tumoral $CD8^+$ T cells compared to isotype control administration (**Fig. 25B**). I next tested whether PF4 directly affects $CD8^+$ T cell responses. When $CD8^+$ T cells were stimulated with PF4, cell division stimulated by anti-CD3/anti-CD28 was not affected (**Fig. 25C**). In addition, production of cytokines such as IFN-γ and IL-2 from OT-I $CD8^+$ T cells co-cultured with ovalbumin (OVA) peptide-pulsed antigen presenting cells was unchanged in the presence or absence of PF4 (**Fig. 25D**). When OT-I $CD8^+$ T cells were adoptively transferred, the OVA-induced cell division *in vivo* were comparable in the presence or absence of anti-PF4 mAb (#6-1-5) (**Fig. 25E**). These data suggest that PF4 blocking may not have a direct effect on $CD8^+$ T cells in my model used. To further assess whether the anti-PF4 mAb-induced anti-tumor effect depends on immunity, I evaluated the effect of anti-PF4 mAb administration in RAG2-deficient mice that lack T and B lymphocytes (**Fig. 26**). I found that anti-PF4 mAb-induced inhibition of tumor growth was completely abolished in RAG2-deficient mice (**Fig. 26**), suggesting that tumor growth reduction is dependent on T and B cells (hence, immunity) but not other non-immune effects.

Regarding safety, the administration of anti-PF4 mAb (#6-1-5) did not cause weight loss and abnormal immune cell activation such as increased ratios of $CD44^{high}$ $CD62L^{low}$ $CD4^+$ or $CD8^+$ T cells (**Fig. 27A** and **27B**), which are strongly and immediately induced following total Treg depletion (**Fig. 27C** and **27D**), but not after selective Th1-Treg reduction [6]. In addition, although total Treg depletion markedly increased aspartate aminotransferase (AST) and alanine aminotransferase (ALT) in the serum and led to severe tissue pathology manifested by massive immune cell infiltrates in liver sinusoids and lungs [6], administration of anti-PF4 mAb (#6-1-5) did not (**Fig. 27E** and **27F**). Thus, PF4 neutralization-dependent Th1-Treg depletion may be safer than total Treg depletion concerning autoimmunity.

I next compared the anti-tumor efficacy of anti-PF4 and anti-CTLA4 (clone 9D9) antibodies. Administration of either anti-CTLA4 or anti-PF4 mAb 3 days after MC38 tumor inoculation did not result in significant differences in tumor growth inhibition (at 17 days post-inoculation) (**Fig. 28A**), suggesting that the anti-tumor efficacy of anti-PF4 mAb (#6-1-5) against the MC38 colorectal tumor may be comparable to that of anti-CTLA4 mAb in this protocol. Analysis of the percentages of Th1-Tregs and total Tregs in the tumors revealed that both were substantially lower in anti-CTLA4 mAb-treated mice compared to tumors from anti-PF4 mAb-treated mice (**Fig. 28B**). This raises the question of whether the modest reduction in Th1-Tregs by anti-PF4 mAb (#6-1-5) treatment is sufficient to induce tumor growth inhibition. To investigate this, I used MC38

tumor-bearing Foxp3-Cre/Tbx21-Flp/VeDTR(LF) mice (**Fig. 28C**, **28D** and **28E**). My previous study showed that peritoneal injection of 100 ng of DT reduced Th1-Tregs by approximately 90% in these mouse tumors [6]. Thus, I reduced both DT dose and frequency to 10 ng, which was injected every two days, to assess its effect on Th1-Treg proportions, achieving a modest reduction of approximately 20-30% in tumors of Foxp3-Cre/Tbx21-Flp/VeDTR(LF) mice (**Fig. 28C**). Tumor growth in mice with this modest Th1-Treg reduction slowed similarly to that observed in Arg1+ TAM-ablated or anti-PF4-treated mice (**Fig. 28D**). Moreover, IFN-γ^+/TNF-α^+ $CD4^+$ T cells or $CD8^+$ T cells in tumors from mice with modest Th1-Treg reduction significantly increased compared to those of tumors from control mice (**Fig. 28E**). TAMs and PF4 can play many roles in regulating tumor growth independently of Tregs [3, 5, 62, 63]. However, given the direct and specific impact of DT treatment on Th1-Tregs in Foxp3-Cre/Tbx21-Flp/VeDTR(LF) mice, the modest reduction of Th1-Tregs induced by anti-PF4 mAb (#6-1-5) treatment might account for the reduced tumor growth rate. The reduced tumor growth in mice with modest Th1-Treg reduction was comparable to that in mice with the profound Th1-Treg reduction (**Fig. 28D**). In addition, the remaining Th1-Tregs in tumors of the partial Th1-Treg depletion could suppress Tconv proliferation similarly to Th1-Tregs from the non-depleted control mice (**Fig. 28F**), suggesting that the remaining Th1-Tregs were functional. Although it remains unclear why the partial and profound Th1-Treg depletion resulted in similar tumor growth reduction, my data suggest that even partial Th1-Treg depletion might be able to effectively enhance anti-tumor immunity if the duration of the partial depletion is extended.

To explore the potential relevance to human cancer and immunology, I analyzed the correlations between PF4 expression levels and the prognosis of various cancer patients using the Cancer Genome Atlas (TCGA) database. I found that the survival probability of patients with $PF4^{high}$ pan-tumors was significantly lower than that of patients with $PF4^{low}$ tumors (**Fig. 29A**). Furthermore, within the $PF4^{high}$ group, the survival probability of individuals with $CD11b^{high}$ tumors was lower than that of patients with $CD11b^{low}$ tumors (**Fig. 29B**), suggesting that greater numbers of $PF4^+$ TAMs might be associated with a poorer prognosis in humans.

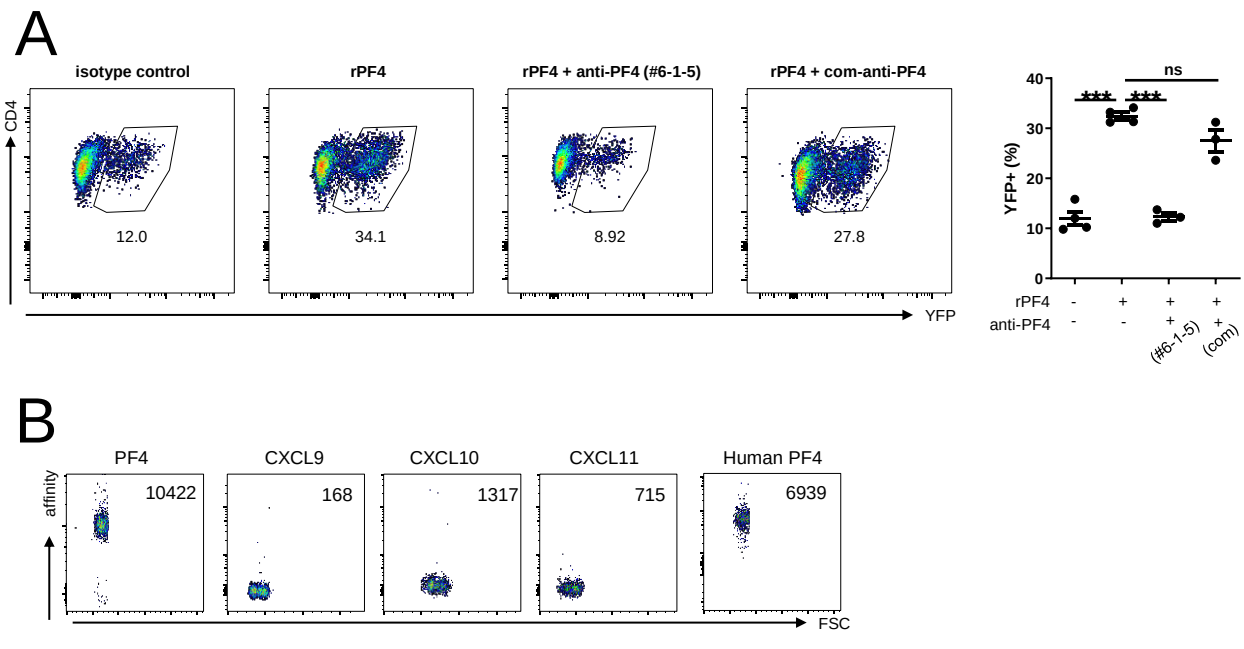

Fig.22. Generation of anti-PF4 monoclonal antibody.

(**A**) Flow cytometry analysis of YFP^- $CD4^+$ $CD25^+$ cells that were derived from spleens of B16F10-bearing Foxp3-Cre/Tbx21-Flp/VeDTR(LF) mice and subsequently stimulated with recombinant PF4 protein (rPF4) w/o indicated anti-PF4 mAb. Gates show YFP^+ cells. Representative FACS plots and the percentages of YFP^+ cells pooled from three independent experiments.

(**B**) Flow cytometry to test affinity of the anti-PF4 mAb (#6-1-5) to mouse PF4, mouse CXCL9, mouse CXCL10, CXCL11 and human PF4. Data are representative of three independent experiments.

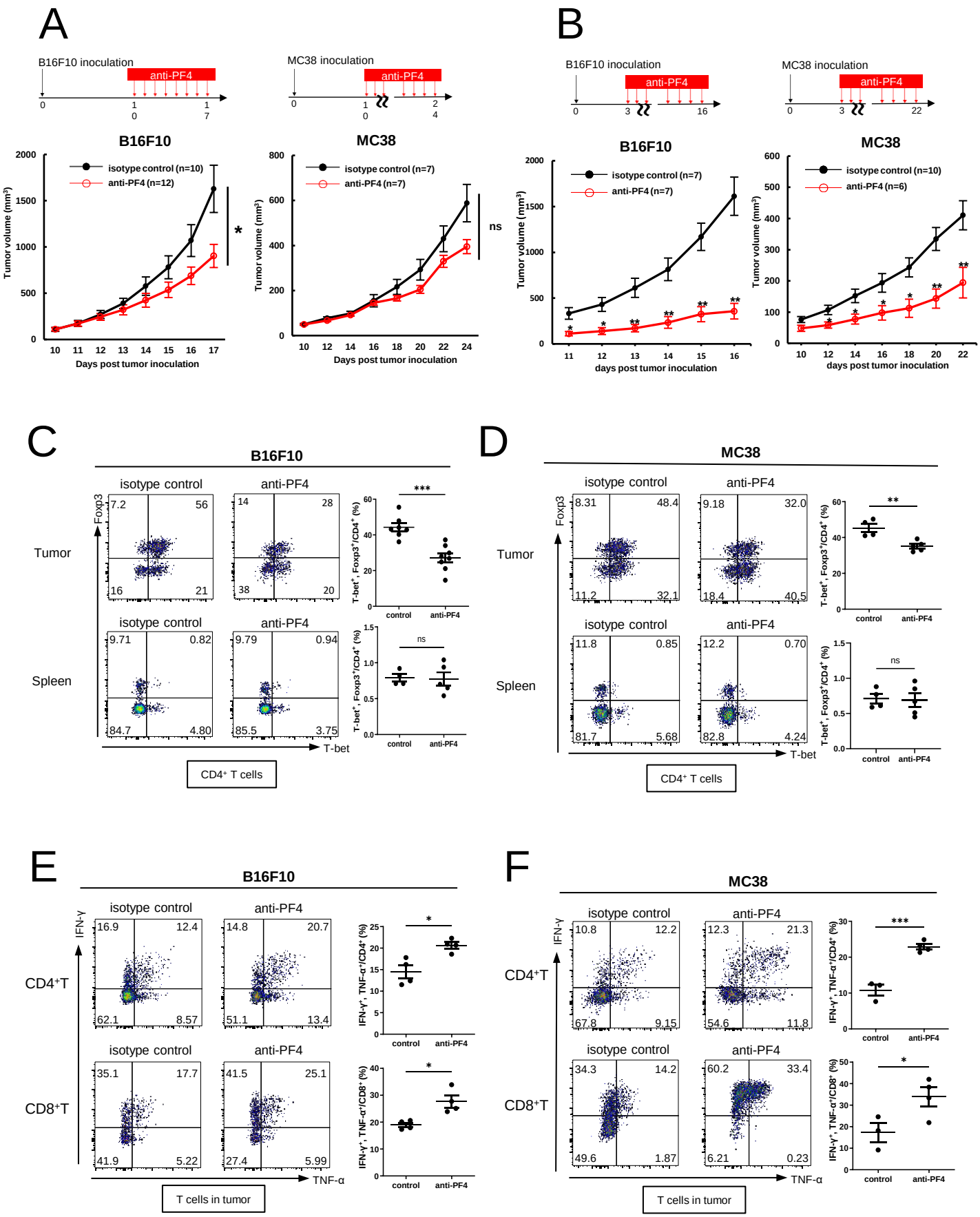
A
B16F10 inoculation
anti-PF4
MC38 inoculation
anti-PF4
B16F10
isotype control (n=10)
anti-PF4 (n=12)
Tumor volume (mm³)
Days post tumor inoculation
MC38
isotype control (n=7)
anti-PF4 (n=7)
ns
B
B16F10 inoculation
anti-PF4
MC38 inoculation
anti-PF4
B16F10
isotype control (n=7)
anti-PF4 (n=7)
days post tumor inoculation
MC38
isotype control (n=10)
anti-PF4 (n=6)
C
B16F10
isotype control
anti-PF4
Tumor
Spleen
Foxp3
T-bet
CD4⁺ T cells
T-bet⁺, Foxp3⁺/CD4⁺ (%)
control
anti-PF4
ns
D
MC38
isotype control
anti-PF4
Tumor
Spleen
CD4⁺ T cells
E
B16F10
isotype control
anti-PF4
CD4⁺T
CD8⁺T
IFN-γ
TNF-α
T cells in tumor
IFN-γ⁺, TNF-α⁺/CD4⁺ (%)
IFN-γ⁺, TNF-α⁺/CD8⁺ (%)
F
MC38
isotype control
anti-PF4
CD4⁺T
CD8⁺T
T cells in tumor

Fig.23. PF4 neutralization by antibodies inhibits tumor growth and Th1-Tregs in tumors.
(**A**) Growth of s.c. implanted B16F10 or MC38 tumors in anti-PF4- or isotype control mAb-injected wild-type mice (indicated numbers of mice per group). mAb injection started at day 10 after tumor inoculation.
(**B**) Growth of s.c. implanted B16F10 or MC38 tumors in anti-PF4- or isotype control mAb-injected wild-type (indicated numbers of mice per group). mAb injection started at day 3 after tumor inoculation.
(**C-F**) Flow cytometry analysis of $CD45^+$ $CD4^+$ cells in tumors (**C, D, E, F**) or spleens (**C, D**) derived from anti-PF4- or isotype control mAb-injected wild-type mice that were s.c. implanted with B16F10 (C, E) or MC38 (**D, F**). Representative FACS plots and the percentages of Foxp3 and T-bet double-positive cells in $CD4^+$ T cells in tumors or spleens. n = 3 per group (**C, D**). Representative FACS plots and the percentages of IFN-γ and TNF-α double-positive cells in intra-tumoral $CD4^+$ (top) and $CD8^+$ (bottom) T cells. n = 3-5 per group (**E, F**). mAb treatment was started at day 3 after tumor inoculation.
Data indicate mean ± SEM, and are pooled from two to three independent experiments. Statistical analysis was performed using two-way ANOVA followed by Tukey's multiple comparisons test (**A**) and two-tailed Student's t-tests (**B, C, D, E, F, G**). *, $P < 0.05$; **, $P < 0.01$; ***, $P < 0.001$; ns, nonsignificant.

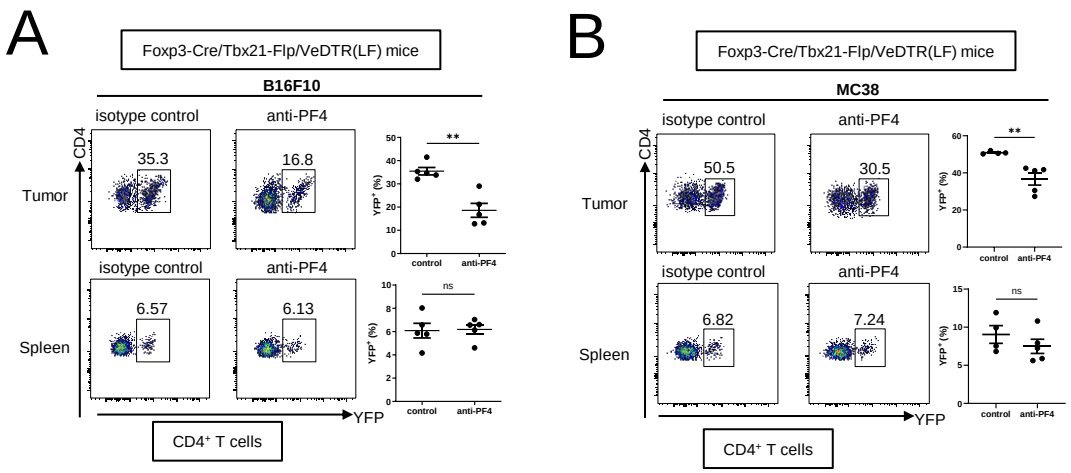

Fig.24. In Foxp3-Cre/Tbx21-Flp/VeDTR(LF) mice mice, administration of anti-PF4 mAb caused inhibition of tumor growth and a decrease in the percentage of Th1-Tregs.

(**A, B**) Flow cytometry analysis of $CD4^+$ $CD45^+$ cells derived from Foxp3-Cre/Tbx21-Flp/VeDTR(LF) mice that were s.c. implanted with B16F10 (**A**) or MC38 (**B**) cells. Representative FACS plots and the percentages of YFP^+ cells in $CD4^+$ T cells in tumors or spleens. n = 4-5 per group.

Data are mean ± SEM, and pooled from two or three independent experiments. Statistical analysis was performed using two-tailed Student's t-tests (A, B). **, $P < 0.01$; ns, nonsignificant.

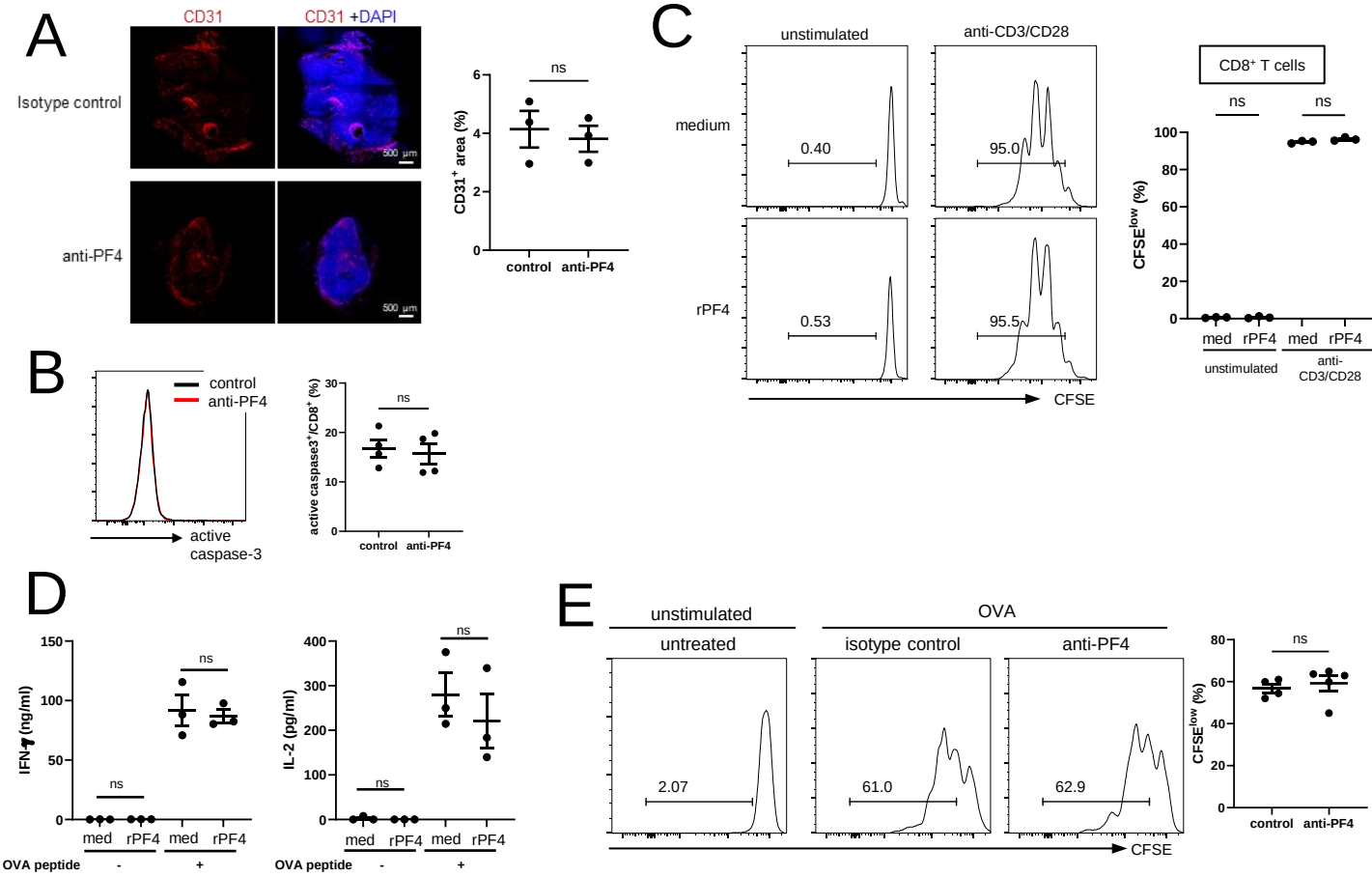

Fig.25. Anti-PF4 mAb administration did not alter intra-tumor vascular architecture.

(**A**) Immunohistochemistry analysis of tissue sections derived from anti-PF4 mAb or isotype control mAb-treated mice that were inoculated s.c. with MC38 cells. Representative images of tumor tissue sections stained with DAPI (blue) and anti-CD31 (red), and the percentages of $CD31^+$ area/tumor area (right) are shown.

(**B**) Expression of activated caspase-3 in tumor-infiltrating $CD8^+$ T cells derived from anti-PF4 mAb or isotype control mAb-treated mice that were s.c. implanted with MC38 cells. n = 4 per group. Representative plot (left) and total results (right) are shown.

(**C**) Flow cytometry analysis of CFSE-labeled naive $CD8^+$ T cells unstimulated or stimulated with rPF4. Representative histograms and the percentages of divided cells pooled from three independent experiments.

(**D**) Concentrations of indicated proteins in the culture supernatants of OT-I $CD8^+$ T cells co-cultured with OVA (257-264) peptide stimulated BMDCsin the absence or presence of rPF4 (5 μg/ml) were measured by ELISA.

(**E**) CFSE-labeled OT-I $CD8^+$ T cells were adoptively transferred into anti-PF4 mAb- or control mAb-treated mice, which were then injected intravenously with OVA (100 μg) and intraperitoneally with poly I:C (10 μg). After 2 d, the fluorescence intensity of CFSE-labeled OT-I $CD8^+$ T cells in the spleens was analyzed by flow cytometry.

Data are mean ± SEM, and pooled from two or three independent experiments. Statistical analysis was performed using two-tailed Student's t-tests (A, B, C, D, E). **, $P < 0.01$; ns, nonsignificant.

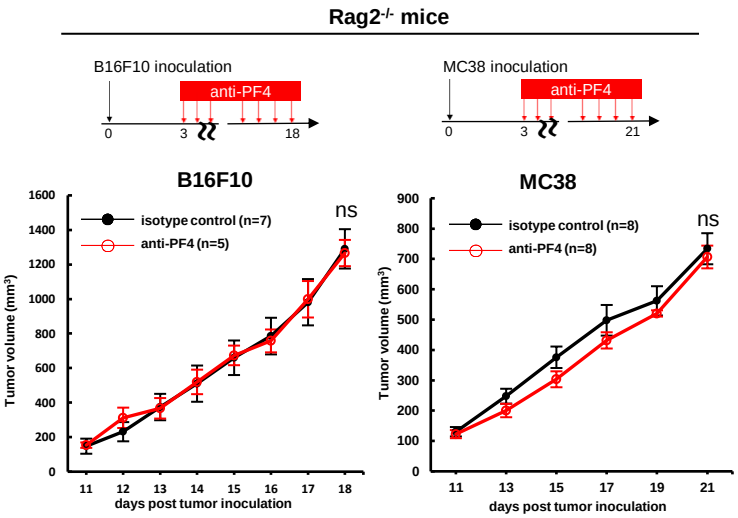

Fig. 26. The inhibitory effect of anti-PF4 mAb on tumor growth was completely abolished in RAG2-deficient mice.

Growth of s.c. implanted B16F10 or MC38 tumors in anti-PF4- or isotype control mAb-injected Rag2$^{-/-}$ mice (indicated numbers of mice per group). mAb injection started at day 3 after tumor inoculation.

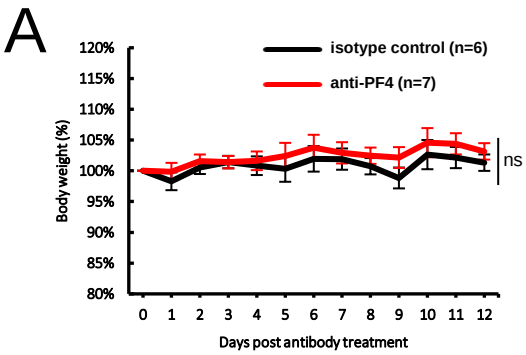
A
isotype control (n=6)
anti-PF4 (n=7)
Body weight (%)
Days post antibody treatment
ns

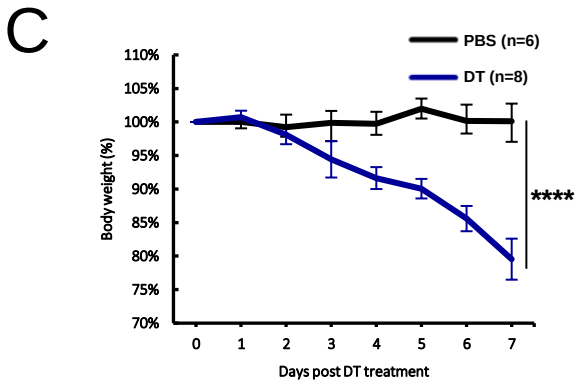
C
PBS (n=6)
DT (n=8)
Body weight (%)
Days post DT treatment
****

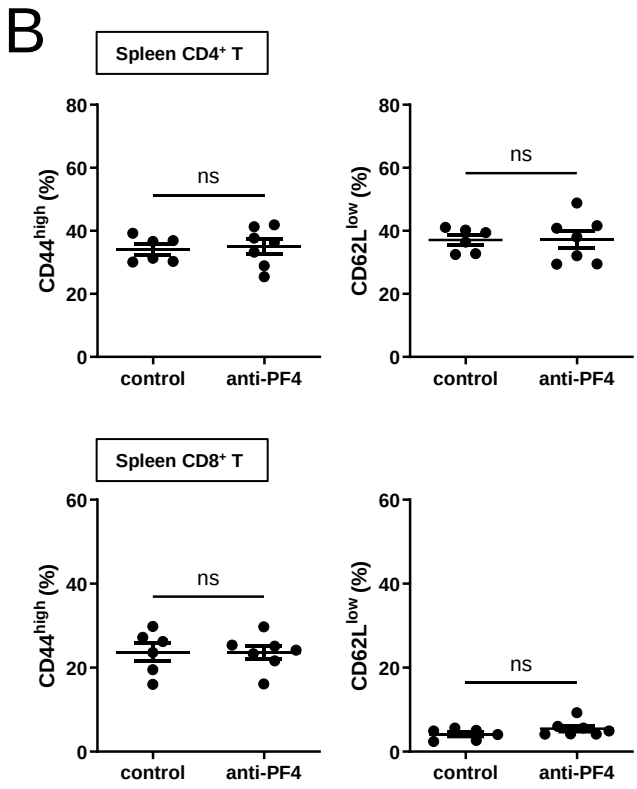
B
Spleen CD4+ T
Spleen CD8+ T
CD44high (%)
CD62Llow (%)
control
anti-PF4
ns

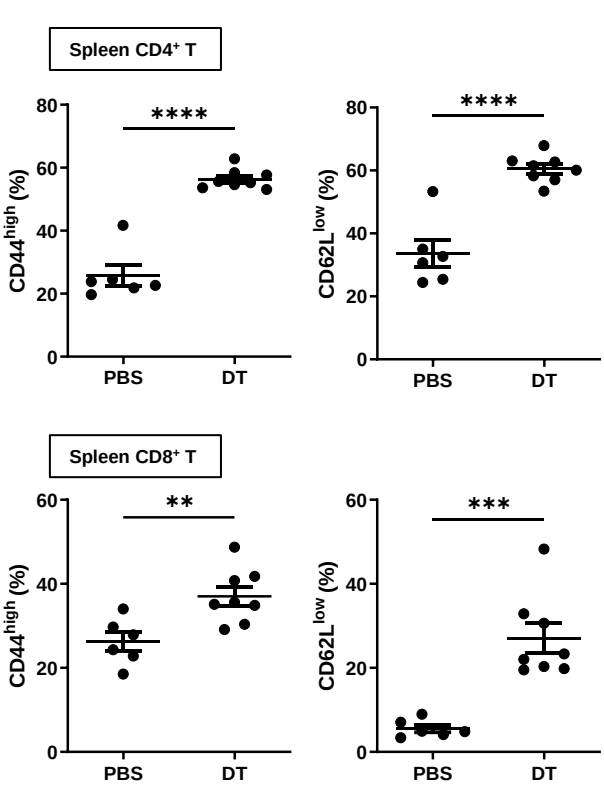
D
Spleen CD4+ T
Spleen CD8+ T
CD44high (%)
CD62Llow (%)
PBS
DT
****
**
***

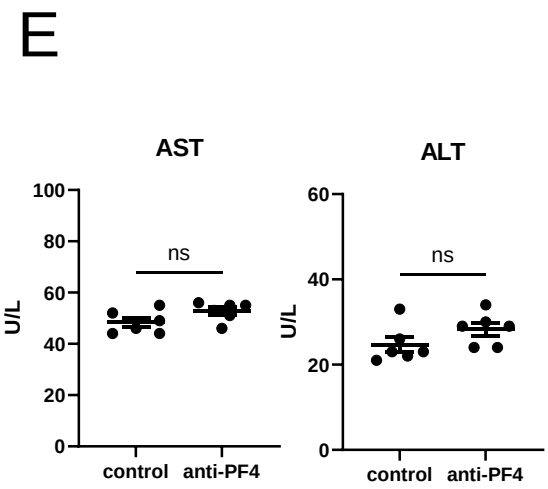
E
AST
ALT
U/L
control
anti-PF4
ns

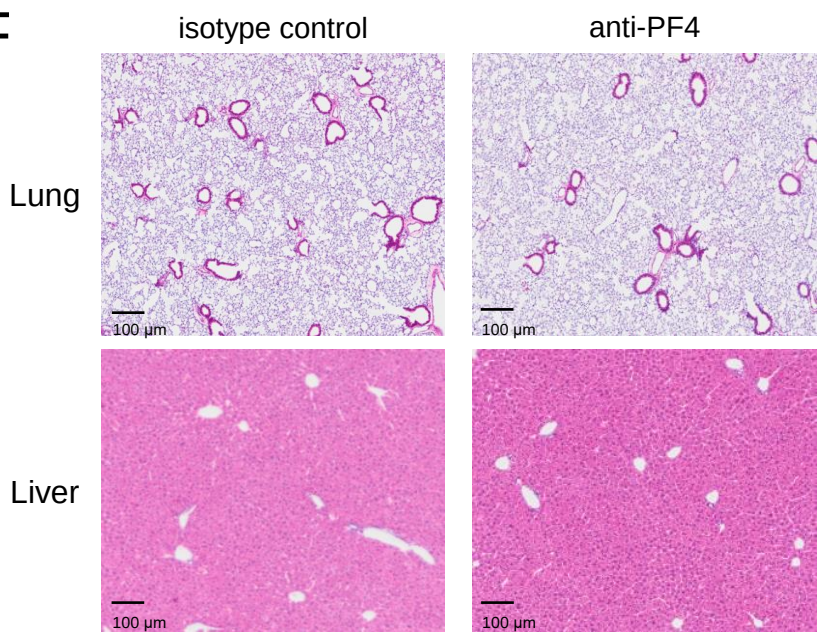
F
isotype control
anti-PF4
Lung
Liver
100 µm

Fig. 27. Anti-PF4 mAb (#6-1-5) did not cause autoimmunity.

(**A**) Body weight change of anti-PF4- or isotype control mAb-injected wild-type mice (indicated numbers per group).

(**B**) Flowcytometric quantification of the percentage of $CD44^{high}$ or $CD62^{low}$ cells in splenic $CD4^+$ T cells or $CD8^+$ T cells of anti-PF4- or isotype control mAb-injected wild-type mice (n = 6-8/group) at day 12 post the first mAb injection. Arrows indicate mAb injection.

(**C**) Body weight change of PBS- or DT-injected Foxp3-Cre/VeDTR(ΔFRT) mice (indicated numbers per group).

(**D**) Flowcytometric quantification of the percentage of $CD44^{high}$ or $CD62^{low}$ cells in splenic $CD4^+$ T cells or $CD8^+$ T cells of PBS- or DT-injected Foxp3-Cre/VeDTR(ΔFRT) mice (n = 6-8/group) at day 7 post the first DT injection. Arrows indicate DT injection.

(**E**) 12 days after the initial injection of anti-PF4 mAb or isotype control mAb (n =6 each), concentration of AST and ALT in the serum were measured. Vertical bars indicate means with SD.

(**F**) The liver and lung were sectioned and stained with H&E.

Data are mean ± SEM, and pooled from two or three independent experiments. Statistical analysis was performed using two-tailed Student's t-tests (A, B, C, D, E). **, $P < 0.01$; ***, $P < 0.001$; ****, $P < 0.0001$; ns, nonsignificant.

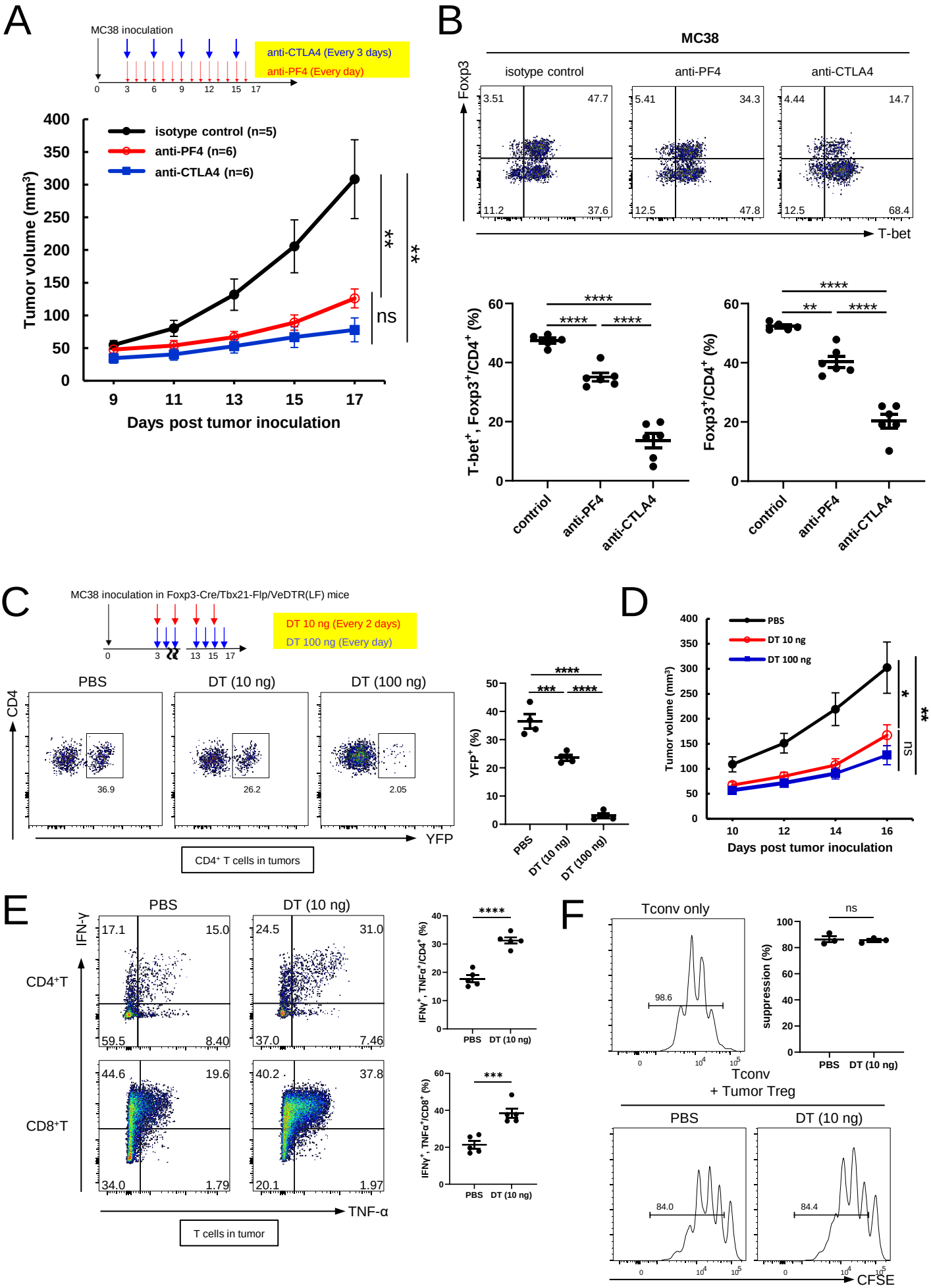
A
MC38 inoculation
anti-CTLA4 (Every 3 days)
anti-PF4 (Every day)
isotype control (n=5)
anti-PF4 (n=6)
anti-CTLA4 (n=6)
Tumor volume (mm³)
Days post tumor inoculation
ns
B
MC38
isotype control
anti-PF4
anti-CTLA4
Foxp3
T-bet
T-bet⁺, Foxp3⁺/CD4⁺ (%)
Foxp3⁺/CD4⁺ (%)
contriol
anti-PF4
anti-CTLA4
C
MC38 inoculation in Foxp3-Cre/Tbx21-Flp/VeDTR(LF) mice
DT 10 ng (Every 2 days)
DT 100 ng (Every day)
PBS
DT (10 ng)
DT (100 ng)
CD4
YFP
CD4⁺ T cells in tumors
YFP⁺ (%)
D
PBS
DT 10 ng
DT 100 ng
Tumor volume (mm³)
Days post tumor inoculation
ns
E
PBS
DT (10 ng)
IFN-γ
CD4⁺T
CD8⁺T
TNF-α
T cells in tumor
IFNγ⁺, TNFα⁺/CD4⁺ (%)
IFNγ⁺, TNFα⁺/CD8⁺ (%)
F
Tconv only
suppression (%)
Tconv
+ Tumor Treg
CFSE

Fig. 28. Comparison of anti-tumor efficacy by anti-PF4 and anti-CLTA4 mAb.

(**A**) Growth of s.c. implanted MC38 tumors in anti-CTLA4 mAb-, anti-PF4 mAb- or isotype control mAb-injected wild-type mice (indicated numbers of mice per group). mAb injection started at day 3 after tumor inoculation. Anti-CTLA4 mAb or anti-PF4-/isotype control mAb are injected every 3 days or every day, respectively.

(**B**) Flow cytometry analysis of indicated $CD45^+$ $CD4^+$ cells in tumors derived from anti-CTLA4 mAb-, anti-PF4 mAb- or isotype control mAb-injected wild-type mice that were s.c. implanted with MC38. Representative FACS plots and the percentages of Foxp3 and T-bet double-positive cells or total Foxp3-positive in $CD4^+$ T cells in tumors. n = 5-6 per group. mAb injection started at day 3 after tumor inoculation. Anti-CTLA4 mAb or anti-PF4/isotype control mAbs are injected every 3 days or every day, respectively.

(**C**) Flow cytometry analysis of $CD4^+$ $CD45^+$ cells derived from Foxp3-Cre/Tbx21-Flp/VeDTR(LF) mice that were s.c. implanted with MC38 cells. Representative FACS plots and the percentages of YFP^+ cells in $CD4^+$ T cells in tumors or spleens. n = 5 per group. DT (10 ng) or PBS injection started at day 3 after tumor inoculation. Both DT (10 ng) and PBS are injected every 2 days. DT (100ng) were started at day 3 and injected every day.

(**D**) Growth of s.c. implanted MC38 tumors in Foxp3-Cre/Tbx21-Flp/VeDTR(LF) mice treated with DT (10 ng) or PBS every 2 days, or with DT (100 ng) every day from day 3 after tumor injection. n = 5 per group.

(**E**) Representative FACS plots and the percentages of IFN-γ and TNF-α double-positive cells in intra-tumoral $CD4^+$ (top) and $CD8^+$ (bottom) T cells from MC38 tumor-bearing Foxp3-Cre/Tbx21-Flp/VeDTR(LF) mice treated with DT (10 ng) or PBS every 2 days from day 3 after tumor injection. n = 5 per group.

(**F**) YFP^+ Treg cells from tumors of PBS-treated or DT (10 ng)-treated Foxp3-Cre/Tbx21-Flp/VeDTR(LF) mice (n = 3 each) were co-cultured with CFSE-labeled naïve $CD4^+$ T cells (Tconv) for 3 days, and the suppression activity was determined. Lines indicate means with SD. Representative result (lower) and total results (n = 3) (upper).

Data are mean ± SEM, and pooled from two independent experiments. Statistical analysis was performed using two-tailed Student's t-tests (A, E, F) and one way ANOVA followed Dunnett's multiple comparisons test (B, C, D). **, $P < 0.01$; ***, $P < 0.001$, **** $P < 0.0001$; ns, nonsignificant.

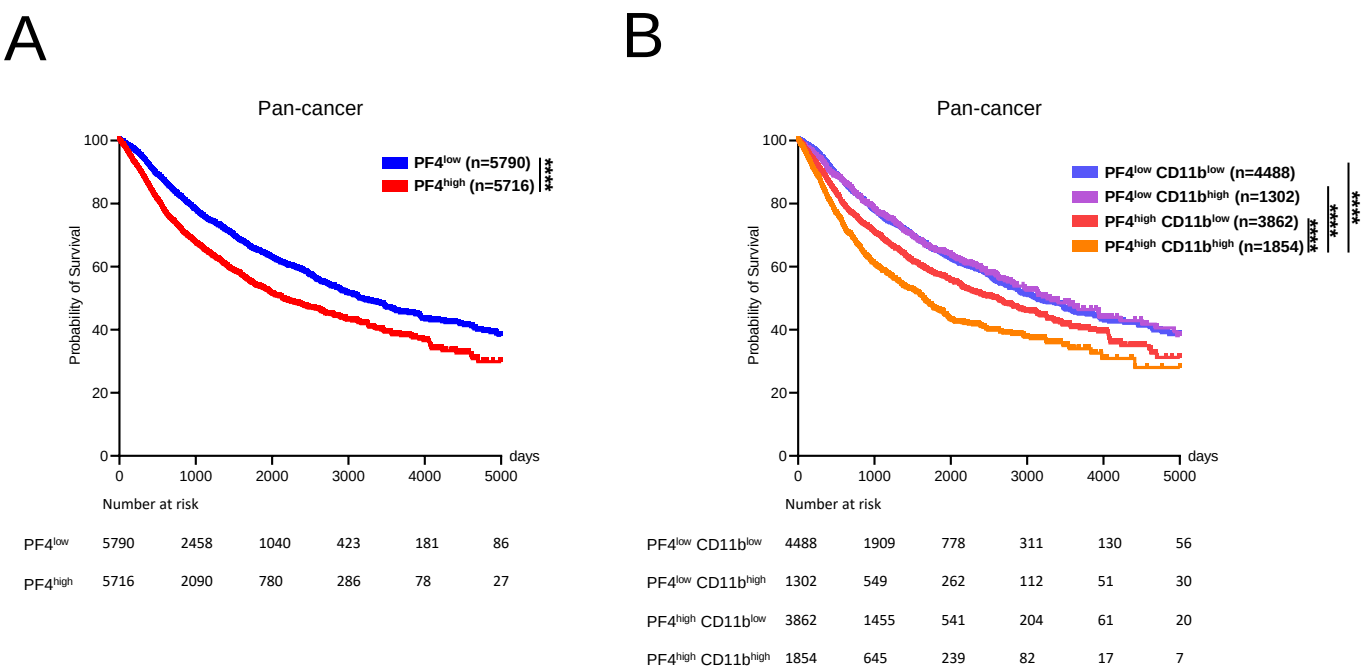

Fig. 29. High PF4 and CD11b expression in human tumors exhibit poor prognosis.

(**A, B**) Kaplan-Meier curves from TCGA (The Cancer Genome Atlas) pan-cancer data analysis show the effect of PF4 high and low expression alone (A) or together with CD11b (ITGAM) high and low expression on time for patient survival (B). Statistical analysis was performed using with log-rank test. ****, $P < 0.0001$

DISCUSSION

In this study, I have developed a genetic method to deplete $Arg1^+$ TAMs, and demonstrated that $Arg1^+$ TAMs are directly involved in Th1-Treg polarization. Previous studies demonstrated that anti-CSF1R mAb-mediated TAM depletion reduced Tregs and inhibited tumor growth [26, 64]. Together with my current findings, an anti-CSF1R mAb-dependent anti-tumor mechanism may involve Th1-Treg reduction in the TME. Tregs in the TME are shown to restrict $CD8^+$ T cell-dependent anti-tumor immunity [7]. $Arg1^+$ TAM depletion increased the ratios of LAG-3^- $CD8^+$ T cells, and enhanced anti-tumor IFN-γ^+/TNF-α^+ $CD8^+$ T cells, suggesting that the $Arg1^+$ TAM depletion-induced change of $CD8^+$ T cells might be indirectly caused by Th1-Treg reduction in the TME. Arg1 is known to have pro-tumor functions such as promoting tumor cell growth by generating polyamines [65] and suppressing anti-tumor immune responses by depleting L-arginine, which is required for T cell growth [66]. Given that tumor growth is suppressed by Arg1 inhibitors and myeloid cell-specific inhibition of Arg1 [40], the suppression of tumor growth by the removal of $Arg1^+$ TAMs may be partly due to Arg1 deficiency in the TME. However, since the Th1-Treg polarization occurred even when Arg1 was inhibited in the co-culture of $Arg1^+$ TAMs and Tregs in vitro, Arg1 and its metabolites are not involved in the Th1-Treg polarization. Given the differential expression pattern of Pf4 and Arg1 mRNAs in macrophages, high lactate within the TME may contribute to the expression of PF4 in TAMs, thereby increasing tumor growth via Th1-Treg polarization.

A previous study has shown that CXCR3 is important for Treg accumulation and immunosuppression in tumors [7], where the significance of CXCR3 in the interaction between Tregs and CXCL9-expressing cDC1 in tumors was suggested [7]. In contrast, my present study showed that the significance of CXCR3 on Tregs is important for Th1-Treg polarization itself. Considering that PF4-producing $Arg1^+$ macrophages are particularly prominent in tumors, it is conceivable that Tregs in close contact with PF4-producing $Arg1^+$ TAMs may differentiate into Th1-Tregs in the TME in a manner dependent on CXCR3. Although both CXCL9 and PF4 are CXCR3 ligands, CXCL9 is important for anti-tumor immunity and well co-related with favorable prognosis in human cancer patients [55, 67-70]. I found that both PF4 and CXCL9 can similarly stimulate Th1-Treg polarization, however, the number of PF4-producing $Arg1^+$ TAMs was much higher than that of CXCL9-producing cDC1s. Previous studies have shown that cDC1s play various immune-stimulatory roles in polarizing $CD4^+$ T cells to anti-tumor Th1 by producing IL-12 and in cross presentation to stimulate anti-tumor $CD8^+$ T cells in the TME [56]. In contrast, TAMs are shown to be immune-suppressive to express IL-10 and

TGF-β to induce $CD4^+$ T cell polarization into Th2 and Tregs, respectively [71]. Here I found a pro-tumor role of $Arg1^+$ TAMs in polarizing Tregs to Th1-Tregs by producing PF4. Collectively, my data and the previous findings suggest that, although PF4 and CXCL9 may stimulate T cells similarly, the predominance of PF4-producing Arg1+ TAMs (immune-suppressive TIMs) over CXCL9-producing cDC1s (immune-stimulatory TIMs) might lead to immune-suppressive outcomes in the TME, making these chemokines appear to act differently. Alternatively, CXCL9 has been shown to bind with two distinct CXCR3 isoforms, CXCR3-A and CXCR3-B, whereas PF4 binds with CXCR3-B alone [53]. Moreover, CXCR3-A signaling by CXCL10 and CXCR3-B signaling by PF4 exert opposite effects on Th1 and Th2 cytokine production in human T cells [72]. In addition, CXCL10/CXCR3 binding drives effector Th1 polarization, while CXCL11/CXCR3 binding induces an immune-suppressive state that is characterized by $IL\text{-}10^+$ Tr1 cells and $IL\text{-}4^+$ Th2 cells via distinct signaling pathways [73], suggesting that each of CXCR3 ligands can act differentially on T cells. Thus, although both PF4 and CXCL9 similarly stimulate Th1-Treg polarization *in vitro*, it remains unclear whether PF4 and CXCL9 act similarly or differently in the *in vivo* tumor models, requiring more studies in the future. Previous studies have shown that IFN-γ is shown to polarize Tregs into Th1-Tregs outside TME such as regional draining LNs [38, 74]. My present study indicates that IFN-γ signaling plays a critical role not only in the initial preparation of CXCR3 on non-Th1-Tregs but also in subsequent PF4-mediated Th1-Treg polarization *in vitro*, where PF4 reinforces IFN-γ signaling in Tregs at the levels of signal transduction and gene regulation. Furthermore, I demonstrate that a very low concentration of IFN-γ, with the help of PF4, synergistically promotes Th1-Treg polarization. Considering the significance of CXCR3 signaling in PF4-reinforced Th1-Treg polarization, IFN-γ signaling-induced CXCR3 may be a prerequisite in non-Th1-Tregs for PF4-reinforced Th1-Treg polarization. Moreover, given that Th1-Tregs express more Ifng mRNA than non-Th1-Tregs, as the levels of IFN-γ from polarized Th1-Tregs increase, the significance of PF4 might gradually diminish due to the positive feedback in which IFN-γ, rather than PF4, becomes the main driver of Th1-Treg polarization *in vitro*. However, the significance of IFN-γ production from Tregs in PF4-reinforced Th1-Treg polarization *in vitro* and in the TME should be tested in more detail in the future. Collectively, my data indicate that the main role of PF4 is likely to reinforce IFN-γ-induced Th1-Treg polarization.

Since injection of recombinant PF4 protein caused inflammation and inhibited angiogenesis [61, 63, 75-79], PF4 has been considered to act as an anti-tumor factor. It has also been reported that PF4 is produced by $Ly6G^+$ $CD11b^+$ myeloid cells in premetastatic lungs and inhibits tumor metastasis [80]. On the other hand, it was

previously reported that anti-PF4 mAb administration was effective in suppressing tumor repopulation after chemotherapy and that its function involves immune system [81]. Whether the anti-tumor effect is due to inhibition of Th1-Tregs induction was not tested. Furthermore, some clinical evidence suggests that plasma PF4 is elevated in a number of cancers including breast [82, 83], prostate [83], colorectal [84], and osteosarcoma [85]. Thus, high PF4 levels correlate with stage of progression and poor prognosis [86]. I also found that TCGA Pan-cancer patients with $PF4^{high}$ tumors had shorter survival periods than those with $PF4^{low}$ tumors, and those with $CD11b^{high}$ and $PF4^{high}$ tumors had even shorter survival periods than those with both $CD11b^{low}$ $PF4^{low}$ tumors, suggesting that PF4high tumors that are highly infiltrated with $CD11b^{+}$ cells may be correlated with poor prognosis. However, whether PF4 is a pro-tumor or an anti-tumor, and whether there are differences in the timing and type of tumors, need to be further examined in the future.

Materials and Methods

Cell lines

MC38 mouse colon carcinoma cells and B16F10 mouse melanoma cells were as described previously [1]. MC38 cells were cultured in RPMI1640 (Nacalai Tesque) with 10% heat-inactivated FBS (Gibco), 100 U/ml penicillin, and 0.1 mg/ml streptomycin (Nacalai Tesque). B16F10 cells were cultured in DMEM (Nacalai Tesque) with 10% heat-inactivated FBS (Gibco), 100 U/ml penicillin, and 0.1 mg/ml streptomycin (Nacalai Tesque). Cells were maintained in culture at 37 °C and 5% CO2.

Mice

C57BL/6NCrSlc (C57BL/6N; CD45.2) mice were purchased from Japan SLC, Inc. Foxp3-Cre mice, RAG2-deficient mice, VeDTR(LF) mice, Foxp3-Cre/VeDTR(ΔFRT) mice, Foxp3-Cre/Tbx21-Flp/VeDTR(LF) mice and congenic CD45.1 mice were described as previously [6]. Ifngr1$^{-/-}$ mice were described previously [87]. OT-I mice were described previously [88]. Ifngr1$^{fl/fl}$ mice were described previously [89]. All animal experiments were conducted with the approval of the Animal Research Committee of Research Institute for Microbial Diseases in Osaka University.

Reagents

PE/Cyanine7 anti-mouse/human CD11b Antibody (Cat#101216), Alexa Fluor® 594 anti-mouse/human CD11b Antibody (Cat#101254), PerCP/Cyanine5.5 anti-mouse CD45.2 Antibody (Cat#109828), Alexa Fluor® 647 anti-mouse CD45.2 Antibody (Cat#109817), PE/Cyanine7 anti-mouse CD4 Antibody (Cat#100422), Alexa Fluor® 594 anti-mouse CD4 Antibody (Cat#100446), Brilliant Violet 421™ anti-mouse CD8a Antibody (Cat#100738), Brilliant Violet 421™ anti-mouse/human CD45R/B220 Antibody (Cat#103240), Brilliant Violet 421™ anti-mouse CD11c Antibody (Cat#117330), PerCP/Cyanine5.5 anti-mouse CD11c Antibody (Cat#117328), APC/Cyanine7 anti-mouse Ly-6G Antibody (Cat#127624), APC anti-mouse CD170 (Siglec-F) Antibody (Cat#155507), PerCP/Cyanine5.5 anti-mouse CX3CR1 Antibody (Cat#149009), APC anti-P2RY12 Antibody (Cat#848005), PerCP/Cyanine5.5 anti-mouse CD25 Antibody (Cat#102030), PE anti-mouse CD25 Antibody (Cat#102007), Alexa Fluor® 647 anti-mouse FOXP3 Antibody (Cat#126408), PE anti-mouse IFN-γ Antibody (Cat#505808), Alexa Fluor® 647 anti-mouse TNF-α Antibody (Cat#506314), APC anti-mouse CD62L Antibody (Cat#104411), PE anti-mouse/human CD44 Antibody (Cat#103008), APC anti-mouse CD80 Antibody (Cat#104713), APC anti-mouse CD206 (MMR) Antibody

(Cat#141707), APC anti-Nos2 (iNOS) Antibody (Cat#696807), APC anti-mouse CD152 Antibody (Cat#106309), PE anti-mouse CD357 (GITR) Antibody (Cat#126309), Brilliant Violet 421™ anti-mouse F4/80 Antibody (Cat#123131), Brilliant Violet 421™ anti-mouse/human CD11b Antibody (Cat#101236), Alexa Fluor® 594 anti-mouse CD31 Antibody (Cat#102520), PE anti-mouse NK-1.1 Antibody (Cat#108708), APC/Cyanine7 anti-mouse/human CD11b Antibody (Cat#101226), Brilliant Violet 421™ anti-mouse NK-1.1 Antibody (Cat#108741), Brilliant Violet 421™ anti-mouse CD90.2 (Thy-1.2) Antibody (Cat# 140327), Brilliant Violet 421™ anti-mouse Ly-6C Antibody (Cat#128031), Brilliant Violet 421™ anti-mouse Ly-6G Antibody (Cat#127628), Brilliant Violet 605™ anti-mouse I-A/I-E Antibody (Cat#107639), Brilliant Violet 711™ anti-mouse Ly-6G Antibody (Cat#127643), Brilliant Violet 711™ anti-mouse Ly-6C Antibody (Cat#128037), Brilliant Violet 605™ anti-mouse CD45 Antibody (Cat#103139), PE/Cyanine7 anti-mouse CD11c Antibody (Cat#117318), APC/Cyanine7 anti-mouse/rat XCR1 Antibody (Cat#148223), PE anti-mouse CD24 Antibody (Cat#101807), PE/Cyanine7 anti-mouse I-A/I-E Antibody (Cat#107630), PE anti-mouse CD11c Antibody (Cat#117308), PE/Cyanine7 anti-mouse CD8a Antibody (Cat#100722), APC anti-mouse CD4 Antibody (Cat#100412), Purified anti-mouse CD16/32 Antibody (Cat#101302), Purified anti-mouse CD3ε Antibody (Cat#100302), Ultra-LEAF™ Purified anti-mouse CD28 Antibody (Cat#102121), recombinant mouse CXCL4/PF4 (Cat#590208), recombinant Mouse SPP1 (Osteopontin) (Cat#763604), recombinant mouse CXCL9 (Cat#578202), recombinant mouse CXCL10 (Cat#573602), recombinant mouse CXCL11 (Cat#578302), and recombinant human CXCL4/PF4 (Cat#550904) were purchased from BioLegend. Anti-mouse/human Arg1 (Cat#17-3697-82), Fixable Viability Dye eFluor™ 450 (Cat#65-0863-14) and anti-F4/80 Monoclonal Antibody (BM8) (Cat#17-4801-82) were purchased from Invitrogen. PE Mouse anti-T-Bet (Cat#561265), APC-Cy™7 Mouse Anti-Mouse CD45.1 (Cat#560579), PE Rabbit Anti-Active Caspase-3 (Cat#570184), PE Rat Anti-Mouse CD103 (Cat#561043) and PE Mouse Anti-Stat1 (pY701) (Cat#612564) were purchased from BD Pharmingen. InVivoMAb anti-mouse CTLA-4 (CD152) (Cat#BE0164) was purchased from Bio X cell. CF488A Donkey Anti-Goat IgG (H + L) and CF594 Donkey Anti-Goat IgG (H + L) were purchased from Biotium. DAPI (Cat#11034-56) was purchased from Nacalai Tesque. Antibodies for CyTOF analysis were as described previously [1]. Recombinant mouse IFN-γ (Cat#315-05), human TGF-β1 (Cat#100-21C), and mouse IL-2 proteins (Cat#212-12) were obtained from Pepro Tech. AMG487 (Cat#S8682) was purchased from Selleck Chemicals. Diphtheria Toxin (Cat#322326) was purchased from Millipore. Collagenase D (Cat#11088882001), Dispase II (Cat#4942078001), DNase I (Cat#11284932001) were

purchased from Roche. HIF-1 alpha Polyclonal antibody (Cat#20960-1-AP) was purchased from Proteintech. Rabbit polyclonal anti-mCherry (Cat#ab167453), and nor-NOHA (Cat#ab285408) were purchased from Abcam. Goat polyclonal anti-Human HB-EGF (Cat#AF-259-NA) to stain DTR and anti-CXCL4/PF4 antibody (Cat#MAB595) were purchased from R&D Systems.

Generation of Cx3cr1-Cre mice, Arg1-RFP/Flp mice, Pf4$^{-/-}$ mice, Pf4$^{fl/fl}$ mice and Ifngr1$^{fl/fl}$ mice

The T7-transcribed Cx3cr1_gRNA1, Arg1_gRNA2, Pf4_gRNA3, Pf4_gRNA4, Pf4flox_gRNA5, Pf4flox_gRNA6, Ifngr1flox_gRNA7 and Ifngr1flox_gRNA8 products, which were amplified by using KOD FX NEO (Toyobo) and the primers (Cx3cr1_gRNA1 5'-TTAATACGACTCACTATAGGatgggtctctcctgctctgaGTTTTAGAGCTAGAAATAGCAAGTTAAAAT -3'; Arg1_gRNA2 5'-TTAATACGACTCACTATAGGtggcgcattcacagtcacttGTTTTAGAGCTAGAAATAGCAAGTTAAAAT -3'; Pf4_gRNA3 5'-TTAATACGACTCACTATAGGccttcccctcggaaggcaggGTTTTAGAGCTAGAAATAGCAAGTTAAAAT -3'; Pf4_gRNA4 5'-TTAATACGACTCACTATAGGggttggaagaagggaagagaGTTTTAGAGCTAGAAATAGCAAGTTAAAAT -3'; Pf4flox_gRNA5 5'-TTAATACGACTCACTATAGGgcagcgacgctcatgtcaagGTTTTAGAGCTAGAAATAGCAAGTTAAAAT -3'; Pf4flox_gRNA6 5'-TTAATACGACTCACTATAGGcagctgatacctaactctccGTTTTAGAGCTAGAAATAGCAAGTTAAAAT -3'; Ifngr1flox_gRNA7 5'-TTAATACGACTCACTATAGGcaatcaccgaggcagagtgtGTTTTAGAGCTAGAAATAGCAAGTTAAAAT-3'; Ifngr1flox_gRNA8 5'-TTAATACGACTCACTATAGGactattgaagtgacccaaaaGTTTTAGAGCTAGAAATAGCAAGTTAAAAT-3') were used as the subsequent generation of Cx3cr1_gRNA1, Arg1_gRNA2, Pf4_gRNA3 gRNA, Pf4_gRNA4, Pf4flox_gRNA5, Pf4flox_gRNA6, Ifngr1flox_gRNA7 and Ifngr1flox_gRNA8. MEGAshortscript T7 (Life Technologies) was used for the generation of these gRNAs. Cas9 mRNA was generated by in vitro transcription (IVT) using mMESSAGE mMACHINE T7 ULTRA kit (Life technologies) and the template that was amplified by PCR using pEF6-hCas9-Puro and the primers T7Cas9_IVT_F and Cas9_R and gel-purified. The synthesized gRNA and Cas9 mRNA were purified using MEGAclear kit (Life Technologies). To obtain Cx3cr1-Cre mice, Arg1-RFP mice, Arg1-Flp mice, Pf4$^{-/-}$ mice, Pf4$^{fl/fl}$ mice and Ifngr1$^{fl/fl}$ mice, CD45.2

C57BL/6N female mice (6 week-old) were superovulated and mated to CD45.2 C57BL/6N stud males. Fertilized one-cell-stage embryos were collected from oviducts and injected into the pronuclei or the cytoplasm with 100 ng/μl Cas9 mRNA, 50 ng/μl gRNA and 50 ng/ml the targeting vector for Cx3cr1-Cre mice, Arg1-RFP mice or Arg1-Flp mice. The injected live embryos were transferred into oviducts of pseudopregnant ICR females at 0.5 d post coitus. The male pup harboring the mutation was mated to CD45.2 C57BL/6N female mice and tested for the germ line transmission.

To generate Cx3cr1-Cre mice, 1.4 kb fragment containing exon2 and 3' untranslated sequence of the Cx3cr1 gene was amplified by PCR using primers (Cx3cr1_LA_F 5'-gaattcGTGTCACCATTAGTCTGGGCGTCT -3'; Cx3cr1_LA_R 5'-ctcGAGCAGGAGAGACCCATCTCCCTCGCT -3'; Cx3cr1 _RA_F 5'-agatctAGGGGTCTCCCCGACCCTAGCTCC-3'; Cx3cr1_RA_R 5'-gcggccgcTCCATGGTAAGGCGAGTCAGCA -3') and cloned in pBluescript vector. P2A peptide sequence containing mammalian codon optimized Cre recombinase cDNA, which was artificially synthesized and obtained from FASMAC, was inserted just before the stop codon of Cx3cr1 in the exon2. The targeting vector was gel purified and used for injection into embryos with Cx3cr1_gRNA1 and Cas9 mRNA. To generate Arg1-RFP/Flp mice, 1.4 kb fragment containing exon8 and 3' untranslated sequence of the Arg1 gene was amplified by PCR using primers Arg1_LA_F 5'-gaattcCTCCATGACTGAAGTAGACAAGCT -3'; Arg1_LA_R 5'-ctcgagCTTAGGTGGTTTAAGGTAGTCAGT -3'; Arg1 _RA_F 5'-ggatccCTGTGAATGCGCCACATGAAAACC -3'; Arg1_RA_R 5'-gcggccgcCTTGTCTCATTACAGAGCCAAG -3') and cloned in pBluescript vector. P2A peptide sequence containing mCherry or mammalian codon optimized Flp recombinase cDNA, which were artificially synthesized and obtained from FASMAC, was inserted just before the stop codon of Arg1 in the exon8. The targeting vector was gel purified and used for injection into embryos with Arg1_gRNA2 and Cas9 mRNA.

For generation of the targeting fragment for the floxed Pf4 allele, the Pf4 gene was isolated from genomic DNA that was extracted from C57BL/6N embryonic fibroblasts by PCR using KOD FX NEO (Toyobo) and primers (Pf4_flox_LA_F 5'-gaattcAATTTCCAACCCCACATCTCCAACCCCACAGCGGTCAGCCTCACCACA ATCGGC-3'; Pf4_flox_LA_R 5'-ctcgagCAAGAGGGTGCCACTGGACCCAAAGATAAAGTTCTACCTTGAGGAAAT GGGTCT -3'; Pf4_flox_MA_F 5'-ctcgagATAACTTCGTATAGCATACATTATACGAAGTTATgccaccATGAGCGTCGCT GCGGTGTTTCGAGGCCTCCGGC-3'; Pf4_flox_MA_R 5'-

acgcgtCTAgCTCTCCAGGATTTTCTTGATTACTTTCTTATATAGGGGTGCTTGCCG GTC -3'; Ifngr1_flox_RA_F 5'-
acgcgtATAACTTCGTATAGCATACATTATACGAAGTTATGTATCAGCTGCCTAAA TGTCAATTGTGTTACAAGACTCCT-3'; Pf4_flox_RA_R 5'-
gcggccgcGACCCCCCTACAGGCAATAGTATAAGAATAAAAGTTATTTTTAATATT TCAT-3'). The targeting fragment was constructed from a 1.9-kb fragment of Pf4 genomic DNA. The floxed 0.73-kb subfragments containing exons 1, 2 and 3 (all coding sequence) were ligated with other fragments using restriction enzymes in pBluescript. The vectors were amplified and co-injected into the embryos with the Cas9-encoding mRNA, Pf4flox_gRNA5 and Pf4flox_gRNA6 to obtain $Pf4^{fl/+}$ pups. $Pf4^{fl/+}$ mice were further crossed with Cx3cr1-Cre mice to generate Cx3cr1-Cre/$Pf4^{fl/fl}$ mice.

For generation of the targeting fragment for the floxed Ifngr1 allele, the Ifngr1 gene was isolated from genomic DNA that was extracted from C57BL/6N embryonic fibroblasts by PCR using KOD FX NEO (Toyobo) and primers (Ifngr1_flox_LA_F 5'-
gtcgaCCCAGAATATGTCCAGACTACTTGAGTCTGCAGTTCTGGTTTTCAGAGC AAAGAAGTGAACCATT-3'; Ifngr1_flox_LA_R 5'-
gaattctctgcctcggtgattgAACTTCACCTCTGACTTTGTCTTTAGGAAAGTATGATTAG TGATAAAT -3'; Ifngr1_flox_MA_F 5'-
gaattcATAACTTCGTATAGCATACATTATACGAAGTTATgtgtAGGTAAAGAGCTTC TTGTCTGAGATT-3'; Ifngr1_flox_MA_R 5'-
acgcgtgggtcacttcaatagtACTTATGTTGGTTTTTTTCTTATCAGAATCTATGACACAT GAGTCTTA -3'; Ifngr1_flox_RA_F 5'-
acgcgtATAACTTCGTATAGCATACATTATACGAAGTTATaaaaTGGACTTAATTGCC AACACTGGCCAG-3'; Ifngr1_flox_RA_R 5'-
gcggccgcGAAGTAACCTGCCCAGTGTGGAAAGACTACGAAGAGGAGGTGACA ACCCCTGACCCGAAGAA-3'). The targeting fragment was constructed from a 2.2-kb fragment of Ifngr1 genomic DNA. The floxed 0.55-kb subfragments containing exon 4 were ligated with other fragments using restriction enzymes in pBluescript. The vectors were amplified and co-injected into the embryos with the Cas9-encoding mRNA, Ifngflox_gRNA7 and Ifngflox_gRNA8 to obtain $Ifngr1^{fl/+}$ pups. $Ifngr1^{fl/+}$ mice were further crossed with Foxp3-Cre mice to generate Foxp3-Cre/$Ifngr1^{fl/fl}$ mice.

Murine tumor model

Tumor cells were injected subcutaneously into 7-11-week-old sex-matched mice. 1.0×10^6 MC38 cells or 3.0×10^5 B16F10 cells in PBS were injected subcutaneously to back

of mice. For DT treatment, tumor-bearing mice were i.p. injected with 100 ng DT (Millipore) in 200 μL PBS. DT injection started on day 10 after tumor inoculation and continued on a daily basis. Tumor volume was measured using a digital caliper and calculated by the following formula: (short diameter)^2 × long diameter × 0.52. When the calculated tumor volume was larger than 2500 mm^3, mice were euthanized within 24 hours. Without specific indication, tumor-bearing mice were analyzed at 15-21 days after tumor inoculation.

Cell preparation from mice

For the isolation of splenocytes, spleens were mashed in PBS on 70 μm cell strainer using a syringes plunger and collected by centrifugation for 5 min at 2000 rpm, then suspended in ACK buffer and kept for 2 min at RT to lyse red blood cells. After ACK treatment, cells were washed and filtered by a 40 μm cell strainer. For the isolation of brain cells, brains were mashed in HBSS on 70 μm cell strainer using a syringes plunger, collected by centrifugation for 5 min at 2000 rpm, and treated with ACK buffer. Then cells were suspended in 40% Percoll (Sigma-Aldrich) in HBSS and centrifuged for 20 min at 2,380×g to remove floating debris. The precipitates were washed in HBSS. For digestion of lung and liver, tissues were cut into small pieces (approximately 3×3 mm) by laser in HBSS, then Collagenase D (1 mg/mL), Dispase II (80 μg/mL), and DNase I (20 μg/mL) were added and incubated for 60 min at 37°C on a shaker. After digestion, cells were treated with ACK buffer, and then suspended in 40% Percoll (Sigma-Aldrich) in HBSS and centrifuged for 20 min at 2,380×g to remove floating debris. The precipitates were washed in HBSS. Tumors were digested using Tumor Dissociation Kit, mouse (Miltenyi, Cat#130-096-730) and gentleMACS Octo Dissociator with Heaters (Miltenyi). After digestion, cells were treated with ACK buffer, and then the dead cells were depleted using Dead Cell Removal Kit (Miltenyi, Cat#130-090-101). Prepared cells were suspended in the appropriate buffer for each experiment.

Flow cytometry and cell sorting

For surface staining, cells were blocked with anti-CD16/32 (Biolegend) for 15 min on ice. Cells were stained with antibodies for 15 min on ice in the presence of anti-CD16/32. For intranuclear staining, Foxp3/Transcription Factor Staining Buffer Set (eBioscience, Cat#00-5523-00) was used following the manufacturer's instruction. For staining TNF-α and IFN-γ, cells were stimulated for 4 hr with 50 ng/mL PMA (Nacalai Tesque, Cat#27547-14) and 1 μg/ml ionomycin (Nacalai Tesque, Cat#19444-91) in the presence of 1 μL/mL Golgi-Stop reagent (BD Biosciences, Cat# 554724) at 37°C. After stimulation,

surface-marker staining was performed on cells, followed by fixation, permeabilization, and staining with cytokine-specific antibodies using Cytofix/Cytoperm™ Fixation/Permeabilization Kit (BD Biosciences, Cat#554714) according to the manufacturer's instructions. For staining STAT1 pY701, BD Cytofix™ Fixation Buffer (BD Biosciences, Cat#554655) and BD Phosflow™ Perm Buffer III (BD Biosciences, Cat#558050) were used following the manufacturer's instruction. FACS Aria III (BD Biosciences) was used for data acquisition and cell sorting. The acquired data were analyzed using FlowJo (BD Biosciences).

Single-cell RNA library construction and sequencing

Cells were stained with cell hashing antibody, TotalSeq-C0301 to-C0306 (BioLegend, Cat#155861, Cat#155863, Cat#155865, Cat#155867, Cat#155869, Cat#155871). Single-cell suspension were processed through the 10x Genomics Chromium Controller following the protocol outlined in the Chromium Single Cell 5' Reagent Kits v2 User Guide. Chromium Next GEM Single Cell 5' Kit v2 (Cat# PN-1000263), Chromium Next GEM Chip K Single Cell Kit (Cat# PN-1000287), Dual Index Kit TT Set A, 5' Feature Barcode Kit (Cat# PN-1000256) and Dual Index Kit TN Set A (Cat#PN-1000250) were applied during the process. Approximately 16,500 live cells per sample, according to the manufacturer's recommendations, were loaded onto the Chromium controller to generate 10,000 single-cell gel-bead emulsions for library preparation and sequencing. Oil droplets of encapsulated single cells and barcoded beads (GEMs) were subsequently reverse-transcribed in a Veriti Thermal Cycler (Thermo Fisher Scientific), resulting in mRNA-derived cDNA and HTO-derived cDNA tagged with a cell barcode and unique molecular index (UMI). Next, cDNA was then amplified to generate single-cell libraries according to the manufacturer's protocol. Quantification was made with an Agilent Bioanalyzer High Sensitivity DNA assay (Agilent, High-Sensitivity DNA Kit, Cat# 5067-4626). Subsequently amplified cDNA was enzymatically fragmented, end-repaired, and polyA tagged. Cleanup/size selection was performed on amplified cDNA using SPRIselect magnetic beads (Beckman-Coulter, SPRIselect, Cat# B23317). Next, Illumina sequencing adapters were ligated to the size-selected fragments and cleaned up using SPRIselect magnetic beads. Finally, sample indices were selected and amplified, followed by a double-sided size selection using SPRIselect magnetic beads. For cell hashing feature barcode libraries were constructed with HTO-derived cDNA. Final library quality was assessed using an Agilent Bioanalyzer High Sensitivity DNA assay. Samples were then sequenced on NovaSeq 6000 platform in a 28+90 base paired-end mode. The resulting raw reads were processed by cellranger 6.0.0 (10x Genomics). Data analysis

was performed by using SeqGeq (BD Life Sciences). After quality control and normalization, PCA and the unsupervised cell clustering were performed using Seurat plugin.

***In vitro* culture and stimulation of Treg**

Splenic YFP$^-$ Tregs (YFP$^-$ CD4$^+$ CD25$^+$ cells) were sorted from Foxp3-Cre/Tbx21-Flp/VeDTR(LF) mice and stimulated with pre-bound α-CD3 (5 μg/ml) and α-CD28 (2 μg/ml) in RPMI1640 culture medium containing mIL-2 (20 ng/ml) and hTGF-β (5 ng/ml) in the presence or absence of recombinant mouse PF4 protein (5 μg/ml), SPP1 (5 μg/ml), AMG487 (0.1 μM), anti-PF4(#6-1-5; 3 μg/ml), com-anti-PF4 (3 μg/ml), nor-NOHA (10 μM) for 3 days.

Co-culture experiments

YFP- Tregs (YFP$^-$ CD4$^+$ CD25$^+$ cells of spleens from tumor-bearing Foxp3-Cre/Tbx21-Flp/VeDTR(LF) mice, 5.0 × 10^4 cells) and TAMs (RFP$^-$ or RFP$^+$ CD45$^+$, Ly6C$^-$, Ly6G$^-$, NK1.1$^-$, B220$^-$, CD90.2$^-$, MHCII$^+$, F4/80$^+$, CD11b$^+$ cells in tumors of Arg1-RFP mice, 5.0 × 10^4 cells) were directly co-cultured in 96 well culture plate stimulated with pre-bound α-CD3 (5 μg/ml) and α-CD28 (2 μg/ml) in RPMI1640 culture medium containing mIL-2 (20 ng/ml), hTGF-β (5 ng/ml) for 3 days. After 3 days of co-culture, percentages of YFP+ cells were analyzed using flow cytometry. For transwell indirect co-culture system of Tregs and TAMs, Tregs (1.0 × 10^5 cells) were plated into a 24-well culture plate stimulated with pre-bound α-CD3 and α-CD28 in RPMI1640 culture medium containing mIL-2, hTGF-β, and TAMs (1.0 × 10^5 cells) were seeded onto transwell insert (with a 0.4 μm pore size, Corning, Cat#3470) top to the 24-well plate. After 3 days of co-culture, percentages of YFP$^+$ cells were analyzed using flow cytometry. For transwell co-culture system of splenic macrophages (CD45$^+$ CD11b$^+$ Ly6G$^-$ cells in spleens of wild-type mice, 1.0 × 10^5 cells) and B16F10 cells (5.0 × 10^5 cells), splenic macrophages were plated into a 24-well culture plate, and B16F10 cells were seeded onto transwell insert (with a 0.4 μm pore size, Corning, Cat#3470) top to the 24-well plate. After 24 hr of co-culture, splenic macrophages were collected for PCR.

***In vitro* culture and stimulation of splenic macrophages**

Splenic macrophages (CD45$^+$ CD11b$^+$ Ly6G$^-$ cells in spleens, 5.0 × 10^4 cells) from naïve mice were plated in a 96-well round bottom culture plate in RPMI1640 with 25 mM lactic acid (Nacalai Tesque) or low pH RPMI1640. Low pH RPMI1640 was prepared by adding hydrochloric acid (Nacalai Tesque).

RNA-seq

For RNA-seq analysis, total RNA was extracted from cells with a miRNeasy Mini kit (Qiagen, Cat#217004) following the manufacturer's instruction. Full-length cDNA was generated using SMART-Seq HT Kit (Takara Bio, Cat#634455) following the manufacturer's instruction. An Illumina library was prepared using a Nextera DNA Library Preparation Kit (Illumina, Cat#FC-131-1096) following SMARTer kit instructions. Sequencing was performed on an Illumina NovaSeq 6000 sequencer (Illumina) in the 101-base single-end mode. Sequenced reads were mapped to the mouse reference genome sequences (mm10) using TopHat v2.0.13 in combination with Bowtie2 ver. 2.2.3 and SAMtools ver. 0.1.19. The fragments per kilobase of exon per million mapped fragments (FPKMs) was calculated using Cufflinks version 2.2.1. Volcano plot and heatmap were generated using GraphBio (http://www.graphbio1.com/en/).

***In vitro* Treg suppression assay**

YFP^- Tregs were isolated from Foxp3-Cre/Tbx21-Flp/VeDTR(LF) mice and unstimulated or stimulated with recombinant mouse PF4 protein (5 μg/ml). After 3 days, the Tregs were collected, washed by PBS 2 times, and used as PF4-stimulated or unstimulated Treg. Splenic naive $CD4^+$ T cells ($CD4^+$ $CD45^+$ $CD62L^{high}$ $CD44^{low}$ $CD25^-$ cells; Tconv) were sorted from CD45.1 congenic mice, and labeled with CellTrace CFSE Cell Proliferation Kit (Invitrogen, Cat#C34554) following the manufacturer's instruction. CFSE-labeled T cells (5.0×10^4 cells) were cultured with the PF4-stimulated or unstimulated Tregs (5.0×10^4 cells) in the presence of Dynabeads Mouse T-Activator CD3/CD28 (Gibco, Cat#11452D) and mIL-2 (20 ng/ml). After 3 days of culture, CFSE intensity in Tconv cells was determined using flow cytometry and suppression activity (%) was calculated by the following formula: 100 × (1- (frequency of $CFSE^{low}$ in Tconv treated with Tregs)/(frequency of $CFSE^{low}$ in Tconv alone)). CD45.1 congenic mice were used to discriminate Tconv (CD45.1) and Tregs (CD45.2).

Quantitative RT-PCR

For quantitative PCR, total RNA was extracted using RNeasy Mini Kit (Qiagen, Cat#74106), after which RNA was reverse transcribed using Verso cDNA synthesis Kit (Thermo Scientific, Cat#AB1453B) following the manufacturer's instructions. Quantitative PCR was performed using GoTaq qPCR Master Mix (Promega, Cat#A6002) and CFX Connect (Bio-Rad). The expression of mRNA was normalized to that of β-actin mRNA.

Immunohistochemistry

Tumor, spleen, and liver were fixed with 4% PFA for 2 h at 4°C. They were immersed overnight in 30% sucrose at 4°C, embedded in FSC 22 Frozen Section Media (Leica), and sectioned at 10 μm with CM1860 UV (Leica). Sections were blocked with 0.1% BSA and 1% mouse serum for 1 hr, and incubated with antibody at 4°C overnight. The slides were washed with PBS three times and Labelling was revealed using secondary antibodies at room temperature for 2 hr. After the staining, the images were immediately taken with FV3000 (Olympus).

Histopathological staining

For histopathological staining, livers were fixed by transcardial perfusion with 10% formalin and lungs were removed and fixed by degassing in 10% formalin, after which both livers and lungs were post-fixed with 10% formalin for 48 hrs at 4℃. The fixed tissues were embedded in paraffin and sectioned at 5 μm using REM-710 (Yamato). Sections were stained with hematoxylin and eosin, and mounted with Mount-Quick (Daido Sangyo). The images were observed using FSX100 (Olympus) and VS200 (Olympus).

ELISA

The concentrations of PF4, IFN-γ, and IL-2 were measured by ELISA kit from R&D Systems following the manufacturer's instructions.

Determination of lactate concentration

Tumors and spleens were removed and homogenized. To measure Lactic acid concentration, L-Lactate Assay Kit (Abcam, Cat#ab65331) was used following the manufacturer's instruction. The mean values for lactate concentration (nmol/g) and the SEM were calculated for each condition.

Cell staining for CyTOF

Each sample was first barcoded by different metal-conjugated α-CD45 antibodies in CyFACS Buffer (PBS with 0.1% BSA, 2mM EDTA and 0.01% sodium azide) with anti-CD16/32 (Biolegend). After barcoding, samples were washed twice in CyFACS Buffer and pooled. The pooled samples were stained with a metal-conjugated antibody cocktail against surface proteins in CyFACS Buffer for 45 min at RT. Samples were then washed twice in CyFACS Buffer, and stained with zirconium (IV) chloride in PBS for 5 min at

RT to discriminate live and dead cells, and fixed and permeabilized using Foxp3/Transcription Factor Staining Buffer Set following the manufacturer's instruction. Samples were subsequently stained with a metal-conjugated antibody cocktail against intracellular proteins for 45 min at 4°C. The stained samples were then washed twice in CyFACS Buffer and once in PBS and fixed overnight in 2% formaldehyde (Invitrogen) in PBS with Cell-ID Intercalator-103Rh (Fluidigm, Cat#201103A) at 4°C.

CyTOF analysis

Prior to data acquisition, fixed samples were washed once in CyFACS buffer and twice in Cell Acquisition solution (CAS) (Fluidigm, Cat#201240). Washed samples were suspended with CAS containing 15% EQ Four Element Calibration Beads (Fluidigm, Cat# 201078) and filtered. Helios mass cytometer (Fluidigm) was used for data acquisition. For acquired data analysis, live singlet cell gating and sample debarcoding were performed using FlowJo and subsequential analysis was performed using Cytobank ver. 9.1 (Beckman Coulter). vi-SNE algorithm and FlowSOM algorithm in Cytobank were respectively used for t-SNE 2D mapping and clustering.

Monoclonal Antibody Generation

PF4-deficient mice were immunized with recombinant mouse PF4 protein emulsified in TiterMax Gold adjuvant (TiterMax, Cat#G-1X5). Lymph nodes from immunized mice were harvested, homogenized to single-cell suspensions, and fused to U3P1 cells with PEG (Hampton Research, Cat#HR2-527). Fused hybridoma cells were seeded in 96-well plates in RPMI1640 with BM Condimed H1 (Roche, Cat#11088947001). After 24 hr, HAT Supplement (Thermo Scientific, Cat#21060017) was added to the culture supernatant. After ~10 days of culture, a primary screen of supernatants was performed using PF4-coupling latex beads.

Determination of the affinity of anti-PF4 mAb

Antibody affinity was detected using latex beads coated antigen. To prepare antigen-coupling latex beads, the latex beads (Invitrogen, Cat#A37304) and antigen protein (recombinant mouse PF4, mouse CXCL9, mouse CXCL10, mouse CXCL11, or human PF4 protein) were mixed and incubated with gentle mixing at room temperature. To detect antibodies with affinity for antigen, the antigen-coupling latex beads were incubated with anti-PF4 mAb for 15 min. Secondary antibody was used to detect antibodies conjugated to antigen-coupling latex beads.

CFSE proliferation assay

Purified $CD8^+$ T cells were labeled with 5 μM CFSE (Invitrogen). 5×10^4 T cells were cultured with or without PF4 in the presence of Dynabeads Mouse T-Activator CD3/CD28 (Gibco, Cat#11452D). Cell division of stimulated $CD8^+$ T cells was quantified after 72 hr using FlowJo.

***In vitro* OVA/MHC-I presentation**

WT BMDCs were treated with 0.1 nM OVA (257-264) peptide (MBL, Cat#S-5001-P) for 3 h. The cells were washed with PBS, fixed with 0.01% glutaraldehyde/PBS for 30 s, washed three times with PBS and RPMI 1640 and then cocultured in 96-well round bottom plates with $CD8^+$ T cells isolated from spleen of OT-I mice for 72 hr.

***In vivo* OVA/MHC-I presentation**

$CD8^+$ T cells were isolated from the spleens of OT-I mice using Aria III (BD Biosciences) and labeled with CFSE. WT mice were adoptively transferred intravenously with 5.0×10^5 of these isolated $CD8^+$ T cells and then injected intravenously with 100 μg OVA (KANTO CHEMICAL, Cat#01103-31) and intraperitoneally with 10 μg poly I:C (Amersham).

Human correlative studies

Publicly available human cancer datasets from "The Cancer Genome Atlas" (TCGA) (www.cancergenome.nih.gov) and UCSC Xena (https://xenabrowser.net/) were used to correlate PF4 and ITGAM mRNA expression levels in tumors with patient survival.

Statistical analysis

All quantitative data are shown as mean ± standard error of mean (SEM) and were analyzed using GraphPad Software (Prism v10.0.3). Two-tailed Student's t-test was used to compare two datasets. One-way or two-way analysis of variance (ANOVA) followed by Tukey's or Dunnett's multiple comparisons test was used to detect the differences in the results between groups. P values < 0.05 were considered statistically significant.

References and Notes

1. K. E. de Visser, J. A. Joyce, The evolving tumor microenvironment: From cancerinitiation to metastatic outgrowth. *Cancer Cell* 41, 374-403 (2023).
2. A. Sharma, C. Bleriot, J. Currenti, F. Ginhoux, Oncofetal reprogramming in tumour development and progression. *Nat Rev Cancer* 22, 593-602 (2022).
3. M. J. Pittet, O. Michielin, D. Migliorini, Clinical relevance of tumour-associated macrophages. *Nat Rev Clin Oncol* 19, 402-421 (2022).
4. P. Sharma, S. Hu-Lieskovan, J. A. Wargo, A. Ribas, Primary, Adaptive, and Acquired Resistance to Cancer Immunotherapy. *Cell* 168, 707-723 (2017).
5. L. Cassetta, J. W. Pollard, A timeline of tumour-associated macrophage biology. *Nat Rev Cancer* 23, 238-257 (2023).
6. M. Okamoto et al., A genetic method specifically delineates Th1-type Treg cells and their roles in tumor immunity. *Cell Rep* 42, 112813 (2023).
7. M. A. Moreno Ayala et al., CXCR3 expression in regulatory T cells drives interactions with type I dendritic cells in tumors to restrict CD8(+) T cell antitumor immunity. *Immunity* 56, 1613-1630 e1615 (2023).
8. K. Kachler, C. Holzinger, D. I. Trufa, H. Sirbu, S. Finotto, The role of Foxp3 and Tbet co-expressing Treg cells in lung carcinoma. *Oncoimmunology* 7, e1456612 (2018).
9. L. Bejarano, M. J. C. Jordao, J. A. Joyce, Therapeutic Targeting of the Tumor Microenvironment. *Cancer Discov* 11, 933-959 (2021).
10. A. J. Combes, B. Samad, M. F. Krummel, Defining and using immune archetypes to classify and treat cancer. *Nat Rev Cancer* 23, 491-505 (2023).
11. H. Salmon, R. Remark, S. Gnjatic, M. Merad, Host tissue determinants of tumour immunity. *Nat Rev Cancer* 19, 215-227 (2019).
12. T. R. Mempel, J. K. Lill, L. M. Altenburger, How chemokines organize the tumour microenvironment. Nat Rev Cancer, (2023).
13. P. Berraondo et al., Cytokines in clinical cancer immunotherapy. *Br J Cancer* 120, 6-15 (2019).
14. C. Tay, A. Tanaka, S. Sakaguchi, Tumor-infiltrating regulatory T cells as targets of cancer immunotherapy. *Cancer Cell* 41, 450-465 (2023).
15. G. Plitas, A. Y. Rudensky, Regulatory T Cells: Differentiation and Function. *Cancer Immunol Res* 4, 721-725 (2016).
16. Y. Takeuchi, H. Nishikawa, Roles of regulatory T cells in cancer immunity. *Int Immunol* 28, 401-409 (2016).

17. S. Sakaguchi, T. Yamaguchi, T. Nomura, M. Ono, Regulatory T cells and immune tolerance. *Cell* 133, 775-787 (2008).
18. D. R. Littman, A. Y. Rudensky, Th17 and regulatory T cells in mediating and restraining inflammation. *Cell* 140, 845-858 (2010).
19. J. D. Fontenot, M. A. Gavin, A. Y. Rudensky, Foxp3 programs the development and function of CD4+CD25+ regulatory T cells. *Nat Immunol* 4, 330-336 (2003).
20. S. Hori, T. Nomura, S. Sakaguchi, Control of regulatory T cell development by the transcription factor Foxp3. *Science* 299, 1057-1061 (2003).
21. M. Shimizu, S. Sakaguchi, Induction of tumor immunity by removing CD25+CD4+ T cells: a common basis between tumor immunity and autoimmunity. *J Immunol* 163, 5211-5218 (1999).
22. S. J. Santegoets et al., Tbet-positive regulatory T cells accumulate in oropharyngeal cancers with ongoing tumor-specific type 1 T cell responses. *J Immunother Cancer* 7, 14 (2019).
23. M. A. Koch et al., The transcription factor T-bet controls regulatory T cell homeostasis and function during type 1 inflammation. *Nat Immunol* 10, 595-602 (2009).
24. Wynn, T. A., Chawla, A. & Pollard, J. W. Macrophage biology in development, homeostasis and disease. *Nature* 496 445–455 (2013).
25. Gordon, S. & Martinez, F. O. Alternative activation of macrophages: Mechanism and functions. *Immunity* 32 593–604 (2010).
26. Gordon, S. & Taylor, P. R. Monocyte and macrophage heterogeneity. *Nature Reviews Immunology* 5 953–964 (2005).
27. Gordon, S. Alternative activation of macrophages. *Nature Reviews Immunology* 3 23–35 (2003).
28. Martinez, F. O. & Gordon, S. The M1 and M2 paradigm of macrophage activation: time for reassessment. *F1000Prime Rep* 6, 6-13 (2014).
29. B. Z. Qian, J. W. Pollard, Macrophage diversity enhances tumor progression and metastasis. *Cell* 141, 39-51 (2010).
30. Pollard JW. Tumour-educated macrophages promote tumour progression and metastasis. *Nat Rev Cancer* 4 71-78 (2004)
31. Pollard, J. W. Trophic macrophages in development and disease. *Nature Reviews Immunology* 9 259–270 (2009).
32. Engblom, C., Pfirschke, C. & Pittet, M. J. The role of myeloid cells in cancer therapies. *Nature Reviews Cancer* 16 447–462 (2016).
33. Ries, C. H. et al. Targeting tumor-associated macrophages with anti-CSF-1R

antibody reveals a strategy for cancer therapy. *Cancer Cell* 25, 846–859 (2014).

34. Mantovani, A., Allavena, P., Marchesi, F. & Garlanda, C. Macrophages as tools and targets in cancer therapy. *Nat Rev Drug Discov* 21, 799-820 (2022)

35. B. Z. Qian, J. W. Pollard, Macrophage diversity enhances tumor progression and metastasis. *Cell* 141, 39-51 (2010).

36. A. Mantovani, T. Schioppa, C. Porta, P. Allavena, A. Sica, Role of tumor-associated macrophages in tumor progression and invasion. *Cancer Metastasis Rev* 25, 315-322 (2006).

37. T. J. Curiel et al., Specific recruitment of regulatory T cells in ovarian carcinoma fosters immune privilege and predicts reduced survival. *Nat Med* 10, 942-949 (2004).

38. A. Martinez-Usatorre et al., Overcoming microenvironmental resistance to PD-1 blockade in genetically engineered lung cancer models. *Sci Transl Med* 13, (2021).

39. S. P. Arlauckas et al., Arg1 expression defines immunosuppressive subsets of tumor-associated macrophages. *Theranostics* 8, 5842-5854 (2018).

40. O. R. Colegio et al., Functional polarization of tumour-associated macrophages by tumour-derived lactic acid. *Nature* 513, 559-563 (2014).

41. A. M. Mujal et al., Holistic Characterization of Tumor Monocyte-to-Macrophage Differentiation Integrates Distinct Immune Phenotypes in Kidney *Cancer. Cancer Immunol Res* 10, 403-419 (2022).

42. S. Yona et al., Fate mapping reveals origins and dynamics of monocytes and tissue macrophages under homeostasis. *Immunity* 38, 79-91 (2013).

43. C. L. Abram, G. L. Roberge, Y. Hu, C. A. Lowell, Comparative analysis of the efficiency and specificity of myeloid-Cre deleting strains using ROSA-EYFP reporter mice. *J Immunol Methods* 408, 89-100 (2014).

44. A. Sattiraju et al., Hypoxic niches attract and sequester tumor-associated macrophages and cytotoxic T cells and reprogram them for immunosuppression. *Immunity* 56, 1825-1843 e1826 (2023).

45. S. D. Blackburn et al., Coregulation of CD8+ T cell exhaustion by multiple inhibitory receptors during chronic viral infection. *Nat Immunol* 10, 29-37 (2009).

46. L. M. Castello et al., Osteopontin at the Crossroads of Inflammation and Tumor Progression. *Mediators Inflamm* 2017, 4049098 (2017).

47. L. Lasagni et al., PF-4/CXCL4 and CXCL4L1 exhibit distinct subcellular localization and a differentially regulated mechanism of secretion. *Blood* 109,

4127-4134 (2007).

48. V. P. Makarenkova, V. Bansal, B. M. Matta, L. A. Perez, J. B. Ochoa, CD11b+/Gr-1+ myeloid suppressor cells cause T cell dysfunction after traumatic stress. *J Immunol* 176, 2085-2094 (2006).

49. R. K. Bruick, S. L. McKnight, A conserved family of prolyl-4-hydroxylases that modify HIF. *Science* 294, 1337-1340 (2001).

50. A. C. Epstein et al., C. elegans EGL-9 and mammalian homologs define a family of dioxygenases that regulate HIF by prolyl hydroxylation. *Cell* 107, 43-54 (2001).

51. K. Wing et al., CTLA-4 control over Foxp3+ regulatory T cell function. *Science* 322, 271-275 (2008).

52. R. S. McHugh et al., CD4(+)CD25(+) immunoregulatory T cells: gene expression analysis reveals a functional role for the glucocorticoid-induced TNF receptor. *Immunity* 16, 311-323 (2002).

53. L. Lasagni et al., An alternatively spliced variant of CXCR3 mediates the inhibition of endothelial cell growth induced by IP-10, Mig, and I-TAC, and acts as functional receptor for platelet factor 4. *J Exp Med* 197, 1537-1549 (2003).

54. K. Van Raemdonck, P. E. Van den Steen, S. Liekens, J. Van Damme, S. Struyf, CXCR3 ligands in disease and therapy. *Cytokine Growth Factor Rev* 26, 311-327 (2015).

55. R. Bill et al., CXCL9:SPP1 macrophage polarity identifies a network of cellular programs that control human cancers. *Science* 381, 515-524 (2023).

56. T. L. Murphy, K. M. Murphy, Dendritic cells in cancer immunology. *Cell Mol Immunol* 19, 3-13 (2022).

57. M. Zagorulya et al., Tissue-specific abundance of interferon-gamma drives regulatory T cells to restrain DC1-mediated priming of cytotoxic T cells against lung cancer. *Immunity* 56, 386-405 e310 (2023).

58. M. G. Vander Heiden, L. C. Cantley, C. B. Thompson, Understanding the Warburg effect: the metabolic requirements of cell proliferation. *Science* 324, 1029-1033 (2009).

59. A. El-Kenawi et al., Acidity promotes tumour progression by altering macrophage phenotype in prostate cancer. *Br J Cancer* 121, 556-566 (2019).

60. S. Tan et al., Platelet factor 4 enhances CD4(+) T effector memory cell responses via Akt-PGC1alpha-TFAM signaling-mediated mitochondrial biogenesis. *J Thromb Haemost* 18, 2685-2700 (2020).

61. R. J. Sharpe, H. R. Byers, C. F. Scott, S. I. Bauer, T. E. Maione, Growth inhibition

of murine melanoma and human colon carcinoma by recombinant human platelet factor 4. *J Natl Cancer Inst* 82, 848-853 (1990).

62. S. Deng et al., Non-platelet-derived CXCL4 differentially regulates cytotoxic and regulatory T cells through CXCR3 to suppress the immune response to colon cancer. *Cancer Lett* 443, 1-12 (2019).

63. J. Vandercappellen, J. Van Damme, S. Struyf, The role of the CXC chemokines platelet factor-4 (CXCL4/PF-4) and its variant (CXCL4L1/PF-4var) in inflammation, angiogenesis and cancer. *Cytokine Growth Factor Rev* 22, 1-18 (2011).

64. C. H. Ries et al., Targeting tumor-associated macrophages with anti-CSF-1R antibody reveals a strategy for cancer therapy. *Cancer Cell* 25, 846-859 (2014).

65. C. I. Chang, J. C. Liao, L. Kuo, Macrophage arginase promotes tumor cell growth and suppresses nitric oxide-mediated tumor cytotoxicity. *Cancer Res* 61, 1100-1106 (2001).

66. P. C. Rodriguez et al., Regulation of T cell receptor CD3zeta chain expression by L-arginine. *J Biol Chem* 277, 21123-21129 (2002).

67. R. Reschke, T. F. Gajewski, CXCL9 and CXCL10 bring the heat to tumors. *Sci Immunol* 7, eabq6509 (2022).

68. R. Tokunaga et al., CXCL9, CXCL10, CXCL11/CXCR3 axis for immune activation - A target for novel cancer therapy. *Cancer Treat Rev* 63, 40-47 (2018).

69. S. Sharma et al., SLC/CCL21-mediated anti-tumor responses require IFNgamma, MIG/CXCL9 and IP-10/CXCL10. *Mol Cancer* 2, 22 (2003).

70. C. Kanegane et al., Contribution of the CXC chemokines IP-10 and Mig to the antitumor effects of IL-12. *J Leukoc Biol* 64, 384-392 (1998).

71. P. Chaintreuil et al., The generation, activation, and polarization of monocyte-derived macrophages in human malignancies. *Front Immunol* 14, 1178337 (2023).

72. P. Romagnani et al., CXCR3-mediated opposite effects of CXCL10 and CXCL4 on TH1 or TH2 cytokine production. *J Allergy Clin Immunol* 116, 1372-1379 (2005).

73. Y. Zohar et al., CXCL11-dependent induction of FOXP3-negative regulatory T cells suppresses autoimmune encephalomyelitis. *J Clin Invest* 124, 2009-2022 (2014).

74. D. E. Ramirez, M. J. Turk, Th1-like Treg cells are dressed to suppress anti-tumor immunity. *Immunity* 56, 1437-1439 (2023).

75. K. Van Raemdonck et al., Angiostatic, tumor inflammatory and anti-tumor

effects of CXCL4(47-70) and CXCL4L1(47-70) in an EGF-dependent breast cancer model. *Oncotarget* 5, 10916-10933 (2014).

76. Z. Wang, H. Huang, Platelet factor-4 (CXCL4/PF-4): an angiostatic chemokine for cancer therapy. *Cancer Lett* 331, 147-153 (2013).

77. R. J. Sharpe, G. F. Murphy, D. Whitaker, S. J. Galli, T. E. Maione, Induction of local inflammation by recombinant human platelet factor 4 in the mouse. *Cell Immunol* 137, 72-80 (1991).

78. T. E. Maione, G. S. Gray, A. J. Hunt, R. J. Sharpe, Inhibition of tumor growth in mice by an analogue of platelet factor 4 that lacks affinity for heparin and retains potent angiostatic activity. *Cancer Res* 51, 2077-2083 (1991).

79. T. E. Maione et al., Inhibition of angiogenesis by recombinant human platelet factor-4 and related peptides. *Science* 247, 77-79 (1990).

80. J. Jian et al., Platelet factor 4 is produced by subsets of myeloid cells in premetastatic lung and inhibits tumor metastasis. *Oncotarget* 8, 27725-27739 (2017).

81. Y. Zhang et al., CXCL4 mediates tumor regrowth after chemotherapy by suppression of antitumor immunity. *Cancer Biol Ther* 16, 1775-1783 (2015).

82. J. Solassol et al., Serum protein signature may improve detection of ductal carcinoma in situ of the breast. *Oncogene* 29, 550-560 (2010).

83. J. Baselga et al., TGF-beta signalling-related markers in cancer patients with bone metastasis. *Biomarkers* 13, 217-236 (2008).

84. J. E. Peterson et al., VEGF, PF4 and PDGF are elevated in platelets of colorectal cancer patients. Angiogenesis 15, 265-273 (2012).

85. Y. Li et al., Elevated expression of CXC chemokines in pediatric osteosarcoma patients. *Cancer* 117, 207-217 (2011).

86. T. Wiesner, S. Bugl, F. Mayer, J. T. Hartmann, H. G. Kopp, Differential changes in platelet VEGF, Tsp, CXCL12, and CXCL4 in patients with metastatic cancer. *Clin Exp Metastasis* 27, 141-149 (2010).

87. M. Sasai *et al.*, Essential role for GABARAP autophagy proteins in interferon-inducible GTPase-mediated host defense. *Nat Immunol* 18, 899-910 (2017).

88. M. Sasai *et al.*, Uncovering a novel role of PLCbeta4 in selectively mediating TCR signaling in CD8+ but not CD4+ T cells. *J Exp Med* 218, (2021).

89. M. Okamoto, A. Kuratani, D. Okuzaki, N. Kamiyama, T. Kobayashi, M. Sasai, M. Yamamoto, IFN-γ-induced Th1-Treg polarization in inflamed brains limits exacerbation of experimental autoimmune encephalomyelitis. *Proc. Natl. Acad. Sci. U.S.A.* 121, e2401692121 (2024).

List of Publications

1. **Kuratani A**, Okamoto M, Kishida K, Okuzaki D, Sasai M, Sakaguchi S, Arase H, Yamamoto M.

   Platelet factor 4-induced TH1-Treg polarization suppresses antitumor immunity.
   Science. (2024) 386:eadn8608. doi: 10.1126/science.adn8608. PMID: 39571033

ACKNOLEDGMENTS

I would like to express my sincere gratitude to Professor Masahiro Yamamoto and Associate Professor Miwa Sasai of the Department of Immunoparasitology, Research Institute for Microbial Diseases, Osaka University, for their careful guidance and encouragement throughout the course of this study.

I would like to express my heartfelt gratitude to Assistant Professor Masaaki Okamoto, of Department of Infectious Disease Control, Oita University for his invaluable advice and insightful discussions on this study.

I am deeply grateful to Professor Hisashi Arase and Assistant Professor Kazuki Kishida of the Department of Immunochemistry, Research Institute for Microbial Diseases, Osaka University, and Professor Shimon Sakaguchi of the Department of Experimental Immunology, WPI Immunology Frontier Research Center, Osaka University for their guidance and advice in this research.

I am deeply grateful to Associate Professor Daisuke Okuzaki of Genome Information Research Center, Osaka University, for his technical support in this research.

I am also profoundly grateful to Professor Masaru Ishii, Department of Immunology and Cell Biology, Graduate School of Medicine, Osaka University, Professor Takashi Nagasawa, Laboratory of Stem Cell Biology and Developmental Immunology, Graduate School of Medicine, Osaka University, and Professor Kazuhiro Suzuki laboratory of Immune Response Dynamics, WPI Immunology Frontier Research Center, Osaka University for their review of this manuscript.

I would like to express my deepest gratitude to the members of the Department of Immunoparasitology, Research Institute for Microbial Diseases, Osaka University, who have given me tremendous support in various aspects of my research and life.

Finally, I would like to express my deepest gratitude to my parents, who have continued to support me emotionally and mentally throughout my student life.